Blood Oxygen Level Dependent Imaging of Cerebral Mesostructure

Michael Germuska

Wolfson College
University of Oxford

A thesis submitted for the degree of Doctor of Philosophy

Supervisor: Dr. Daniel Bulte

Michaelmas Term, 2013

Blood Oxygen Level Dependent Imaging of Cerebral Mesostructure

Michael Germuska

Wolfson College, University of Oxford

A thesis submitted for the degree of Doctor of Philosophy

Michaelmas Term, 2013

Abstract

In this thesis I investigate blood oxygen level-dependent (BOLD) MRI methods of imaging the cerebral blood volume (CBV), mean vessel radius and oxygen extraction fraction (OEF). Through the investigation of these individual techniques a new framework is proposed for the simultaneous measurement of all three parameters, providing a comprehensive assay of the cerebral mesostructure.

A new method for the segmentation of blood filled voxels from the sagittal sinus is presented. The implemented method is completely automated and thus removes user bias in voxel selection. The segmentation method is used in a volunteer study to calculate CBV from a hyperoxic challenge according to an existing technique. CBV measurements from this study are found to be significantly overestimated. However, a new derivation of the hyperoxic CBV equation is presented that reveals significant errors in the original method, corresponding to the observed overestimates in CBV.

Modelling studies are presented that investigate the discrepancy in reported BOLD MRI measurement of mean vessel size. A significant degree of the variation in the results is found to arise from the noise sensitivity of the analysis methods. This finding is confirmed with experimental data from healthy volunteers that show good agreement with the modelling studies.

Comprehensive modelling of the BOLD response to hyperoxia and hypercapnia is used to develop a new framework for OEF calculation. The new method is based on the calibration of the BOLD signal response against a change in intravascular susceptibility. The OEF calculation is extended by introducing a spin-echo readout into the acquisition scheme. This extension of the acquisition scheme provides a further independent probe of the BOLD signal, enabling the simultaneous calculation of the mean vessel size and CBV. The new framework is shown to provide OEF and vessel size estimates over a wider range of physiological parameters, providing greater scope for the clinical implementation of these techniques.

Acknowledgements

I would like to thank all the people who have helped me during my time at FMRIB and made this thesis possible. In particular my thanks go my supervisor Dr. Daniel Bulte. Dan's extensive knowledge and openness to explore any idea, no matter how crazy, has been a true inspiration. However, he has also known when to give honest feedback and practical advice to focus my work, without which I'm sure I would not have a thesis to write.

Many of the physics group students and post-docs also deserve thanks, in particular Michael Kelly. Mike has been a great support throughout this project and freely gave up numerous early-mornings and late-evenings helping me acquire volunteer data. Another group member who needs a special mention is James Meakin, who has always been a great person to discuss/explain MRI theory and of invaluable help with pulse programming. He and Wilfred Lam have also 'volunteered' for scanning sessions more times than I can count. Of course a big thank you must go to all the other post-docs and students who volunteered to be my victims. So thank you Nic Blockley, Alex Gardener, Rob Frost, Jamie Near, Hannah Hare, Tom Okell and Nico Filippini.

FMRIB has been a great place to study for the last three years and many other people have given their time and valuable advice on everything from pulse programming to data analysis. So thank you to Stuart Claire, Karla Miller, Peter Jezzard, Mark Jenkinson, Matt Robson and Jesper Andersson. However, rather than thanks I feel I should give my apologies to Saad Jbabdi, whose work I so frequently interrupted when speaking to Dan. You guys really need to get your own offices! Outside of FMRIB a big thank you goes to Theis Jochimsen, who so generously shared with me his Monte-Carlo modelling code and started me down the path of vessel size imaging.

Finally, and most importantly, I need to thank my wife Wendy and my parents for all their support during my years of study, who must have often wondered if it would ever end. To those that have had the same thought, this is my final degree, I promise.

Contents

Publications arising from this thesis:

Journal articles:

The influence of noise on BOLD-mediated vessel size imaging analysis methods

Germuska, M., Meakin, J.A., Bulte, D.P.

Journal of Cerebral Blood Flow and Metabolism (2013)

Epub ahead of print. doi: 10.1038/jcbfm.2013.141

MRI Measurement of Oxygen Extraction Fraction, Mean Vessel Size and Cerebral Blood Volume Using Serial Hyperoxia and Hypercapnia

Germuska, M. and Bulte, D.P.

Neuroimage (2014)

Epub ahead of print. doi: 10.1016/j.neuroimage.2014.02.002

Vessel Size Imaging in the Brainstem

Germuska, M. and Bulte, D.P.

In preparation.

Conference abstracts:

Combined Vessel Size and Blood Flow Imaging with Hyperoxia

Germuska, M., Jochimsen, T., Kelly, M., Okell, T., Bulte, D. P.

ISMRM, 2012, Melbourne

Vessel Size Imaging in the Brainstem

Germuska, M. and Bulte, D. P.

ISMRM, 2013, Salt Lake City

Preface

Measurement of tissue oxygen extraction fraction (OEF) and rate of cerebral oxygen metabolism ($CMRO_2$) using oxygen-15 PET has been of fundamental importance in elucidating the processes underlying stroke. PET measurement of OEF has been instrumental in authenticating the theory of 'luxury perfusion' (high or normal blood flow with low OEF) (Baron et al., 1981a) and revealing the presence of 'misery perfusion' (high OEF with low blood flow) (Baron et al., 1981b). In addition to applications in stroke, measurement of OEF has provided useful insight into many other diseases including Parkinson's disease (Wolfson et al., 1985), epilepsy (Bernardi et al., 1983), Alzheimer's disease (Ishii et al., 1996) and cancer (Beaney et al., 1984). However, despite the efficacy of the technique its application is restricted due to the high cost and the high associated dose of ionising radiation, limiting the patient population and the number of repeated measurements in any individual. To overcome these restrictions alternative technologies are needed to measure OEF.

A promising alternative to oxygen-15 PET is the use of magnetic resonance imaging (MRI). MRI uses non-ionising radiation, expanding the applicability of the measurement to a much wider subject group. However, quantitative measurement of OEF via MRI is still in its infancy. One of the developing MRI methods exploits the Blood Oxygen Level-Dependent (BOLD) signal, as used in functional imaging experiments. The BOLD signal change is measured with hyperoxic and hypercapnic gas stimuli, enabling the underlying physiological parameters to be teased apart (Bulte et al., 2012; Gauthier and Hoge, 2012). The magnitude of the BOLD signal response is determined by several

underlying factors including oxy-haemoglobin saturation, blood flow, blood volume, and the tissue structure. While the effects of blood flow and volume are included in the BOLD signal modelling it is currently necessary to make standard assumptions about the tissue structure. However, it is well known that tissue vascularisation can be altered in certain disease states. In fact there is evidence that physiologic mechanisms exist to adjust capillary density to balance oxygen availability and oxygen consumption (Dore-Duffy and LaManna, 2007). Therefore, it is to be expected that disease states that exhibit an altered OEF are more likely to demonstrate a change in mean vessel size and capillary density. This indeed appears to be the case, with changes in vessel size being characteristic of cancer (Kerbel, 2000) and associated with stroke (Xu et al., 2011), Parkinson's disease (Bradaric et al., 2012), epilepsy (Rigau et al., 2007), and Alzheimer's disease (Biron et al., 2011). Thus, the assumption of standard vascular parameters in the BOLD signal analysis is likely not to reflect the underlying tissue properties and cannot be assumed when investigating OEF in these diseases.

Alternative BOLD signal analysis methods, that utilise spin-echo data in addition to gradient-echo data, have been developed to quantify mean vessel size (Jochimsen and Moller, 2008). However, these techniques rely on the assumption of a typical OEF, which as previously discussed, cannot be assumed in a large number of disease states. In this thesis a combined approach is formulated that enables the simultaneous calculation of OEF and mean vessel size from BOLD signal measurements. Modelling studies show that the new method removes a large degree of uncertainty from each of the combined methods, while in-vivo studies are used to confirm the utility of the method in human volunteers. In addition to the development of a new methodology, existing methods of

blood volume quantification are investigated and BOLD vessel size quantification is examined in terms of its noise sensitivity and applicability outside the cerebrum.

Thesis Outline

This thesis is concerned with the development of blood oxygen level-dependent (BOLD) MRI methods of imaging cerebral physiology. The first three chapters introduce the background theory of the BOLD signal and the current state of the art of BOLD physiological measurements. The following chapters are concerned with the main work of this thesis, with chapters 5, 6 and 7 corresponding to the publications arising from this thesis. The chapters are structured in the following manner:

Chapter 1 introduces background information regarding the BOLD signal and BOLD signal models.

Chapter 2 introduces current calibration methods for the measurement of relative and absolute physiological parameters with hyperoxic and hypercapnic stimuli.

Chapter 3 is a general introduction to vessel size imaging and vessel size imaging using the BOLD signal.

Chapter 4 looks in detail at an existing method of blood volume measurement using a hyperoxic stimulus. A new method of vessel segmentation is introduced to reduce user bias and the validity of the measurement technique is investigated from a theoretical perspective.

Chapter 5 uses a signal modelling approach to investigate the noise sensitivity of BOLD vessel size measurement. The modelling results explain a large degree of the

variation in reported BOLD vessel size measurements. The modelling results are confirmed with a volunteer study that agrees well with the simulations.

Chapter 6 introduces a new framework for the simultaneous measurement of the oxygen extraction fraction, cerebral blood volume and means vessel size. The new technique is shown to remove significant uncertainties in each of the combined methods. The applicability of the technique is confirmed with a pilot study in healthy volunteers.

Chapter 7 compares the performance of dual-echo and multi-echo vessel size imaging in the brainstem. Each technique is acquired with and without cardiac gating, which is shown to significantly improve the multi-echo data.

Chapter 8 summarises the main conclusions of this thesis and highlights some possible avenues of future work.

Chapter 1

The BOLD Effect

1.1 Haemoglobin and Blood Susceptibility

Magnetic resonance imaging has the ability to create a wide range of image contrasts related to physiological properties of the tissue under investigation. In functional MRI one of the best known and most widely used contrast methods is based on the blood oxygenation level-dependent (BOLD) fMRI signal. The BOLD contrast relies on changes in deoxyhaemoglobin content, which acts as a paramagnetic contrast agent (Pauling and Coryell, 1936). A molecule of oxyhaemoglobin has no unpaired electrons, producing zero magnetic moment (diamagnetic). While a deoxygenated molecule has a high proportion of un-paired electrons, producing a strong magnetic moment and is thus highly paramagnetic. In fact, the susceptibility of blood is linearly proportional to the fractional haemoglobin saturation (Y) (Weisskoff and Kiihne, 1992).

$$\chi_{blood} = 4\pi \cdot Hct \cdot \Delta\chi_{do}(1-Y) \qquad [1.1]$$

where $\Delta\chi_{do}$ (0.264 ppm) is the difference in susceptibility between entirely oxygenated and entirely deoxygenated red blood cells and the haematocrit (Hct) is related to the haemoglobin concentration by:

$$[Hb] = \frac{Hct}{3.0(ml/g) \cdot 0.016125(g/\mu mol)} \qquad [1.2]$$

As blood passes through the microvasculature oxygen is delivered to metabolically active tissue. This causes the partial pressure of oxygen in the blood (pO_2) to drop from approximately 95 mmHg in the arteries to 30 mmHg in the veins (Bandettini and Wong, 1995). The relationship between oxyhaemoglobin saturation and pO_2 can be approximated by:

$$Y/(1-Y) = (pO_2/P_{50})^{2.8} \qquad [1.3]$$

where P_{50}, the pO_2 at which Y = 0.5, equals 26mm Hg. This means that arterial blood is almost completely saturated, with Y = 0.97, while the saturation of the venous blood is approximately 0.6. Because of this there is limited dynamic range on the arterial side, and the BOLD signal is generally well approximated by considering the susceptibility change in the venous vasculature (venous side of the capillaries, venuoles, collecting veins and pial veins). In the following section the relationship between the venous blood susceptibility and the BOLD signal is explored: providing the framework necessary to link the BOLD signal to the venous oxyhaemoglobin saturation (SvO_2). Having explored this relationship a simplified BOLD model is introduced, allowing the physiological basis of the signal to be understood in greater detail.

1.2 Susceptibility Induced Frequency Shift

When a material is placed in a magnetic field (B_0) the magnetic moments within the material tend to align along the field. The degree of magnetic susceptibility (χ) of the material will dictate the magnetization created in the material, as defined by equation 1.4.

$$M \propto \chi \cdot B_0 \qquad [1.4]$$

The induced magnetization creates an additional magnetic field (B) that adds to B_0, and thus influences the local nuclei precession frequency according to equation 1.5.

$$\omega = \gamma \cdot (B_0 + B) \qquad [1.5]$$

where ω is the precession frequency in rads/sec and γ is the gyromagnetic ratio (267.5×10^6 rad/T). However, the distribution of the additional field, and thus the modulation of the precession frequency, depends on the geometry of the magnetized material. If a venous vessel is considered to be a simple infinite cylinder with uniform susceptibility, then the frequency shifts for the intravascular and extravascular compartments can be determined by equations 1.6 and 1.7 respectively (Bandettini and Wong, 1995).

$$\omega(r,\theta,\phi) = \Delta\omega\left[3\cos^2(\theta) - 1\right]/3 \qquad [1.6]$$

$$\omega(r,\theta,\phi) = \Delta\omega \sin^2(\theta)(a/r)^2 \cos(2\phi) \qquad [1.7]$$

where $\Delta\omega = 2\pi\gamma B_0 \Delta\chi_{d0} Hct(1-Y)$, θ is the angle between the vessel and the B0 field and φ is the azimuthal angle of the proton position in a plane perpendicular to the vessel. Figure 1.1 shows the geometrical relationships that govern these equations. Because a cylindrical perturber causes a distribution of precession frequencies, this causes the spins to lose coherence (dephase) as they precess, inducing a loss of signal. In the next sections the intra and extravascular signal losses are examined in more detail.

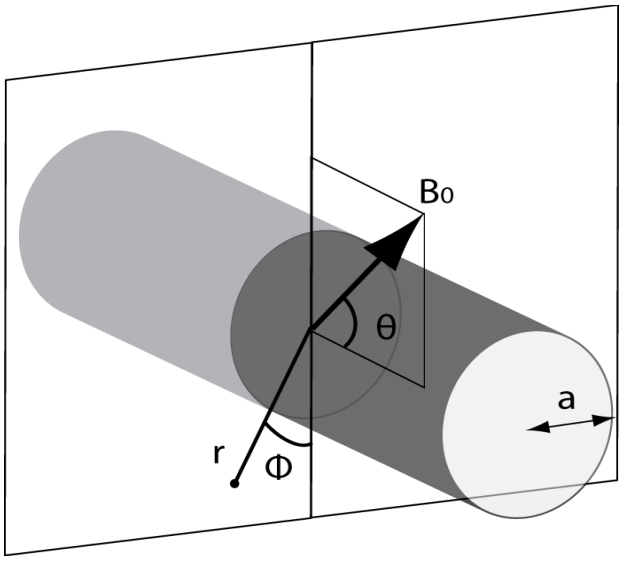

Figure 1.1 Schematic of a proton at a distance 'r' from a cylindrical vessel with radius 'a' in a static magnetic field B_0.

1.3 Intravascular Signal Losses

As shown in equations 1.1 and 1.6 a susceptibility difference between a vessel and its surrounding tissue produces a shift in precession frequency within a vessel. Each voxel acquired in an MRI image will typically contain a large number of vessels at different orientations. Therefore, because the frequency shift within each vessel is dependent on its angle with B_0, there will be a distribution of frequency shifts within a voxel. These multiple frequency shifts cause a phase dispersion and thus a reduction in the blood T_2', where T_2' is the characteristic time constant that describes the decay of transverse magnetization due to time-invariant dephasing. However, it should be noted that a very large vessel (that could span one or more voxels) will have a unique phase shift depending on oxygenation level and orientation.

In addition to the frequency shift effects, the concentration of deoxyhaemoglobin within a vessel has a direct effect on the blood T_2, where T_2 is the time constant associated with the decay of transverse magnetization due to non time-invariant processes. Water protons rapidly exchange between red blood cells and plasma (average water residence time in RBCs = ~5 ms). Thus, during a typical MRI acquisition they frequently change their magnetic environment. While in the blood plasma the water molecules also diffuse through magnetic field gradients generated by the compartmentalised deoxyhaemoglobin within the vessel. These processes of exchange and diffusion cause a loss of phase coherence, known as dynamic averaging, which is a time irreversible process. The blood T_2 due to these effects can be estimated as shown in equation 1.8 (Qin et al., 2011).

$$1/T_2 = A_0 + K_0\left(1 - SvO_2\right)^2 \qquad [1.8]$$

where A_0 is a field independent constant term and K_0 scales quadratically with the magnetic field (and is also dependent on the spin-echo time). This phenomenological relationship between T_2 and haemoglobin saturation has been used in a number of techniques to estimate SvO_2 (Lu, 2007; Nield et al., 2002). However, in the majority of BOLD signal models (Kiselev and Posse, 1999; Sukstanskii and Yablonskiy, 2004; Yablonskiy and Haacke, 1994; Ziener et al., 2007) the compartmentalisation of intravascular haemoglobin has often been ignored.

1.4 Extravascular Signal Losses

The blood-brain barrier ensures that haemoglobin must remain intravascular; therefore the only BOLD contrast mechanisms to affect the extravascular space are due to the intra/extra susceptibility difference and exchange of water between the two compartments.

However, the typical lifetime of water in capillaries (500 ms) (Kim and Ogawa, 2012) is much greater than echo times used in fMRI experiments. Therefore the extravascular BOLD signal can be well approximated by only considering the susceptibility difference as described by equation 1.7. Equation 1.7 has a dependence on the radius of the vessel (a), the distance from the vessel (r) and the angle between the vector, r, and the component of B_0 in the perpendicular plane (ϕ). Thus around any vessel there is a distribution of precession frequencies in the extravascular space. In order to calculate the distribution of frequencies (and thus signal loss) a common approach is to assume there is no extravascular diffusion, the so called static dephasing regime. This assumption is valid if we consider the vascular network to be made of large vessels (radius greater than approximately 10 μm). For large vessels the induced B field falls off slowly and relaxation is dominated by local differences in precession frequencies. Under the assumption of the static dephasing regime Yablonskiy and Haacke (Yablonskiy and Haacke, 1994) showed that equation 1.7 can be integrated over the sum of frequency shifts over time to produce equation 1.9 (Dickson et al., 2011).

$$S_0(t) = \exp\left[-CBV\left({}_1F_2\left(\left\{-\frac{1}{2}\right\};\left\{\frac{3}{4},\frac{5}{4}\right\};-\frac{\Delta\omega^2 t^2}{4}\right)-1\right)\right] \qquad [1.9]$$

where ${}_pF_q$ is the extended hypergeometric function, CBV is the post-capillary cerebral blood volume and $\Delta\omega = 2\pi\gamma B_0 \Delta\chi_{d0} Hct(1\text{-}Y)$. It can be seen that under the stated assumptions, the BOLD signal is only dependent on the venous saturation and CBV. However, this equation is only valid for large vessels where the static dephasing regime can be assumed. If the effects of diffusion are incorporated into the model Ziener et al.

(Dickson et al., 2011; Ziener et al., 2007) showed that the extravascular signal can be approximated by the following equations;

$$s(t) = \int_{-\infty}^{\infty} d\omega p(\omega) \exp(i\omega t) \qquad [1.10a]$$

$$p(\omega) = \frac{1}{\pi} \left| \mathrm{Re} \frac{\hat{S}_0\left(i\omega + \tau_c^{-1}\right)}{1 - \tau_c^{-1}\hat{S}_0\left(i\omega + \tau_c^{-1}\right)} \right| \qquad [1.10b]$$

$$\tau_c = \frac{a^2}{4D} \cdot \frac{\ln|CBV|}{(1 - CBV)} \qquad [1.10c]$$

where $\hat{s}_0$ is the Laplace transform of the signal in the static dephasing regime (averaged over vessel angles from 0 to π) and $p(\omega)$ is the frequency distribution in the presence of diffusion (under the strong-collision approximation). Examination of equations 1.10b-c tells us that the frequency distribution of spins is now dependent on the vessel radius (a) and the diffusion coefficient (D). Thus, incorporating extravascular diffusion into the model has introduced a signal dependence on vessel size. While the BOLD signal now has the expected dependence on vessel size, an analytical solution has yet to be developed that accurately predicts the BOLD response over the complete range of in-vivo vessel scales (Dickson et al., 2011).

To overcome the difficulties in creating an analytical BOLD model, Monte-Carlo modelling of diffusion in a vascular network is often employed (Boxerman et al., 1995; Dickson et al., 2011; Ogawa et al., 1993). By combining the results of such signal modelling with a physiological model, Davis et al. (Davis et al., 1998) created a simplified BOLD model that is widely used by the MR community.

1.5 Simplified BOLD Model

The simplified BOLD model is based on Monte-Carlo modelling studies by (Boxerman et al., 1995) and (Ogawa et al., 1993) and makes several assumptions and approximations in order to parameterise their results. However, because of the simple nature of the model, it becomes possible to substitute in physiologically meaningful parameters, creating a useful tool for interpreting the BOLD signal. The signal is expressed in terms of the relaxation rate R_2*; where R_2* represents the combination of dynamic and time-invariant dephasing processes ($R_2^* = 1/T_2 + 1/T_2'$). Two important approximations used in the simplified model are; firstly that R_2* is linearly dependent on the blood volume fraction, and secondly that R_2* is linearly dependent on the blood susceptibility, χ_{blood}, raised to the power β. Thus, the R_2* contribution due to deoxyhaemoglobin, $R_2^*|_{dHb}$, can be approximated by equation 1.11.

$$R_2^*|_{dHb} = K \cdot CBV(\chi_{blood})^{\beta} \qquad [1.11]$$

where K and β are scaling factors dependent on the vessel geometry and field strength. The signal dependence on β is taken from (Ogawa et al., 1993), who suggests that β=1 for large vessels and β=2 for capillaries.

The modelling underlying equation 1.11 does not consider contributions from the intravascular compartmentalisation of haemoglobin, which is a significant contribution to the BOLD signal at lower field strengths. However, further consideration of β suggests that equation 1.11 may implicitly contain this information. As described by equations 1.1 and 1.8, the intravascular signal attenuation caused by haemoglobin

compartmentalisation also has a quadratic dependence on χ_{blood}. Thus β values closer to 2 can be considered to indicate a greater intravascular signal contribution (as well as smaller vessel scale). At higher magnetic fields, the intrinsic signal of the intravascular compartment is reduced (due to a significantly reduced T_2), and the BOLD signal is dominated by the extravascular effect, thus β should decrease. A typical β value at 1.5T is 1.5, decreasing to 1.3 at 3T (Blockley et al., 2013).

The change in relaxation rate ΔR_2^* at non-baseline values of CBV and blood susceptibility can be expressed as follows:

$$\Delta R_2^* = K\left[CBV \cdot \left(\chi_{blood}\right)^{\beta} - CBV_0 \cdot \left(\chi_{blood,0}\right)^{\beta}\right] \qquad [1.12]$$

where the subscript '0' represents the baseline state. Equation 1.12 tells us that the BOLD signal will be reduced by either an increase in blood volume or blood susceptibility. Re-arranging equation 1.12 we get:

$$\Delta R_2^* = K \cdot CBV_0 \cdot \left(\chi_{blood,0}\right)^{\beta}\left[\left(\frac{CBV}{CBV_0}\right)\left(\frac{\chi_{blood}}{\chi_{blood,0}}\right)^{\beta} - 1\right] \qquad [1.13]$$

The passive change in blood volume due to a change in flow has been demonstrated to follow a power relationship (Grubb Jr et al., 1974), and the change in susceptibility can be linked to a change in blood flow and/or metabolism as follows (Hoge et al., 1999a):

$$\frac{\chi_{blood}}{\chi_{blood,0}} = \left(\frac{CMRO_2}{CMRO_{2,0}}\right)\left(\frac{CBF_0}{CBF}\right) \qquad [1.14]$$

Combining equation 1.13 with these two flow relationships produces equation 1.15.

$$\Delta R_2^* = K \cdot CBV_0 \cdot \left(\chi_{blood,0}\right)^{\beta} \left[\left(\frac{CMRO_2}{CMRO_{2,0}} \right)^{\beta} \left(\frac{CBF}{CBF_0} \right)^{\alpha-\beta} - 1 \right] \qquad [1.15]$$

where the exponent α is the flow/volume coupling constant with an approximate value of 0.38 (Grubb Jr et al., 1974).

Literature values suggest that α is significantly less than β, therefore a BOLD increase requires the fractional change in blood flow to be greater than the fractional change in $CMRO_2$. This leads us to the understanding that a task related increase in the BOLD signal is due to a blood flow change that overcompensates for the local metabolic demand. By probing the changes in BOLD signal due to various stimuli it becomes possible to tease apart equation 1.15 and derive some fundamental properties of the tissue under investigation. In chapter 2 calibrated acquisitions are investigated that allow the calculation of task related changes in $CMRO_2$. In addition, a combination of calibration methods is explored that enables the quantification of baseline venous haemoglobin saturation (SvO_2).

Chapter 2

Calibrated fMRI

2.1 Introduction

Analysis of the simplified BOLD model in chapter 1 shows that the BOLD signal is dependent on changes in blood flow, blood volume and the rate of oxygen consumption. The amplitude of the recorded signal will depend both on the baseline values and the reactivity of each parameter. This complicated dependence on baseline physiology and reactivity means it is difficult to isolate the primary driver for any given signal change, making any comparison between groups or individuals problematic. This problem becomes particularly important when comparing the BOLD response between groups with different vascular properties or baseline physiology (such as the elderly or certain disease states), which is known to strongly influence the dynamic range of the BOLD signal (Gauthier et al., 2011). Therefore, it is necessary to control for any vascular differences between groups or individuals when comparing their BOLD responses.

One method of controlling for the vascular influence on the BOLD signal is to perform a calibration step prior to the investigation (Chiarelli et al., 2007b; Davis et al., 1998). By performing this calibration it becomes possible to calculate the fractional change in $CMRO_2$ for a particular task; therefore isolating a quantitative measure from the BOLD signal that can be compared across patient populations and disease states.

From chapter 1 we know that the change in transverse relaxation, as described by the Davis model, can be expressed as follows:

$$\Delta R_2^* = K \cdot CBV_0 \cdot \left(\chi_{blood,0}\right)^{\beta} \left[\left(\frac{CBV}{CBV_0} \right) \left(\frac{\chi_{blood}}{\chi_{blood,0}} \right)^{\beta} - 1 \right] \qquad [2.1]$$

Equation 2.1 is typically converted into a signal change rather than relaxation rate by making the approximation:

$$\frac{\Delta BOLD}{BOLD_0} \approx -TE \cdot \Delta R_2^* \qquad [2.2]$$

Substituting equation 2.2 in 2.1 leads to:

$$\frac{\Delta BOLD}{BOLD_0} \approx TE \cdot K \cdot CBV_0 \cdot \left(\chi_{blood,0}\right)^{\beta} \left[1 - \left(\frac{CBV}{CBV_0} \right) \left(\frac{\chi_{blood}}{\chi_{blood,0}} \right)^{\beta} \right] \qquad [2.3]$$

The term $TE \cdot K \cdot CBV_0 \cdot (\chi_{blood,0})^{\beta}$ represents the maximum possible BOLD signal change that could be achieved by eliminating all the deoxyhaemoglobin from the intravascular space. For convenience this term is often denoted M. Thus, equation 2.3 becomes:

$$\frac{\Delta BOLD}{BOLD_0} = M \left[1 - \left(\frac{CBV}{CBV_0} \right) \left(\frac{\chi_{blood}}{\chi_{blood,0}} \right)^{\beta} \right] \qquad [2.4]$$

Equation 2.4 can be considered the basic calibration equation, from which the hypercapnic (Davis et al., 1998) and hyperoxic (Chiarelli et al., 2007b) calibration methods both derive. In each method a process for the determination of M is proposed, calibrating the BOLD signal against the baseline physiology. The calibration factor M is

typically used in two ways; first to measure the relative change in $CMRO_2$, and second to determine the flow/metabolism coupling constant.

As shown in chapter 1, an alternative way to express the Davis model is in terms of blood flow and metabolic changes. Thus, equation 2.4 can be reposed as follows:

$$\frac{\Delta BOLD}{BOLD_0} = M\left[1-\left(\frac{CMRO_2}{CMRO_{2,0}}\right)^{\beta}\left(\frac{CBF}{CBF_0}\right)^{\alpha-\beta}\right] \qquad [2.5]$$

The physiological parameters α and β are taken from literature values, typically 0.38 and 1.3 (at 3T) respectively. Therefore, if the value of M is known, measurement of task related changes in CBF and BOLD signal will allow the calculation of relative $CMRO_2$.

A number of studies (Ances et al., 2008; Hoge et al., 1999b) have found that the relative change in $CMRO_2$ is linearly related to the CBF increase. This linear relationship allows the calculation of the flow/metabolism coupling constant (n). Where n is defined as:

$$n = \left(\frac{\Delta CBF}{CBF_0}\right) \Big/ \left(\frac{\Delta CMRO_2}{CMRO_{2,0}}\right) \qquad [2.6]$$

Thus, in addition to calculating relative $CMRO_2$, which is indicative of the metabolic demand of a task, we are also able to probe the vascular responsiveness. The value of n appears to be dependent on cortical region and has a significant impact on the magnitude of the BOLD response (Ances et al., 2008; Chiarelli et al., 2007a; Devonshire et al., 2012). It is also likely that n will change with age and disease. Therefore, measurement of n may offer an insight into the health of the tissue and could be used to track disease progression.

2.2 Hypercapnic Calibration

Examination of equation 2.5 tells us that if we can measure the CBF and BOLD signal response to a stimulus that does not alter $CMRO_2$, then we will be able to calculate M. One such assumed iso-metabolic stimulus is achieved with elevated levels of inspired carbon dioxide (hypercapnia). A hypercapnic stimulus leads to an increase in cerebral blood flow while minimally influencing the rate of metabolism (Hoge, 2012). Breathing elevated levels of carbon dioxide increases the arterial partial pressure ($PaCO_2$) leading to a localised decrease in blood and extravascular pH. The decrease in pH is the initial step in a cascade of events resulting in relaxation of arterial smooth muscle (Brian Jr, 1998). As the smooth muscle relaxes this leads to a localised increase in CBF, the magnitude of which is dependent on its baseline value and the cerebral perfusion pressure. The increased CBF leads to an increase in oxygen delivery and a reduction in venous blood susceptibility, which is inversely proportional to the change in blood flow.

2.2.1 Hypercapnic Data Acquisition

Practical measurement of the changes in both CBF and the BOLD signal is achieved with a modified arterial spin labelling (ASL) sequence during periods of normocapnia interleaved with periods of hypercapnia. The calculated signal from an ASL acquisition is proportional to the rate of cerebral perfusion, or CBF. The ASL signal is calculated from two images (repeated for sufficient SNR), called the tag and control. In the tag image the magnetisation of blood flowing into the brain is inverted, while the control image is acquired without inverting the blood signal. By inserting a post labelling delay (PLD) time into the pulse sequence, time is allowed for the labelled blood to exchange with the

tissue water (typically 1.5 to 2.5 seconds). Thus the tissue signal in the tag acquisition is reduced proportionally to the rate of perfusion. By calculating the difference between the tag and control acquisitions a perfusion-weighted image is produced, where the signal intensity is proportional to the rate of perfusion. A BOLD signal can be extracted from the ASL data either by averaging the tag/control pairs (Buxton, 2002), or by explicitly modelling the ASL and BOLD signal changes (Woolrich et al., 2006).

The ASL perfusion signal is typically only about 1% of the acquired data. Therefore, to maximise the CNR, a short echo time is desirable. However, the BOLD signal is dependent on T_2* processes (rather than T_1 as in ASL), thus sufficient time must be allowed for the signal to dephase and create the BOLD contrast. At 3T the average BOLD echo time used in published studies is 35 ms (Triantafyllou et al., 2011), which is significantly longer than the typical ASL echo time of 10 ms (Liu and Brown, 2007). These different requirements present a problem if the same acquisition is to be used to calculate CBF and BOLD weighted data. A number of solutions exist to this problem. The simplest solution is to select an intermediate echo time that is a compromise between the two sets of demands (Bulte et al., 2012). Alternatively, an interleaved acquisition maybe used where short (perfusion weighted) and long echo (BOLD weighted) acquisitions are acquired alternately. Finally a dual-echo acquisition may be employed that acquires both echoes after a single RF pulse. The interleaved and dual-echo methods have a clear advantage in that they require no compromise in echo time. However, the interleaved approach needs double the number of acquisitions in order to acquire separate perfusion and BOLD-weighted data and hence takes twice as long to acquire. The dual-

echo approach avoids this but may require accelerated acquisition techniques, which can carry a small SNR penalty.

2.3 Hyperoxic Calibration

In addition to manipulating the BOLD signal via a change in CBF, Chiarelli et al. (Chiarelli et al., 2007b) demonstrated how the BOLD response could be calibrated using an oxygen gas challenge. The influence of inspired oxygen fraction (FiO_2) on T_2* weighted MR signals is well established (Rostrup et al., 1995). However, the significant contribution by Chiarelli et al. was to propose a method for measuring the fractional change in susceptibility from end-tidal measurements of O_2.

Again, the calibration method starts from equation 2.4. However, instead of modulating the blood susceptibility with a change in CBF, the oxygenation of the blood is directly altered with an increase in FiO_2. Importantly, mild hyperoxia is taken to be iso-metabolic with only a minimal decrease in CBF and no change in CBV. Thus, equation 2.4 can be simplified to:

$$\frac{\Delta BOLD}{BOLD_0} = M\left[1-\left(\frac{\chi_{blood}}{\chi_{blood,0}}\right)^{\beta}\right] \qquad [2.7]$$

Therefore, the only needed measurements to calculate M are the BOLD signal change and the fractional change in blood susceptibility. The following derivation shows how the fractional change in blood susceptibility can be calculated from the end-tidal oxygen content.

Measurement of the partial pressure of end-tidal O_2 ($P_{ET}O_2$) is possible with a gas analyser and yields a quantity that is equivalent to the alveolar oxygen tension (P_AO_2). In the method presented by Chiarelli et al. this is assumed to be equivalent to PaO_2, the arterial oxygen tension. Having measured the partial pressure of oxygen, an estimate of the oxygen saturation of arterial haemoglobin (SaO_2) can be made according to the Severinghaus (Severinghaus, 1979) equation below.

$$SaO_2 = \frac{1}{\left(\frac{22400}{\left(PaO_2\right)^3 + 150\left(PaO_2\right)} + 1\right)} \qquad [2.8]$$

where the units of PaO_2 are expressed in mmHg and SaO_2 is between 0 and 1 (at or above atmospheric pressure $SaO_2 \approx 1$, when $FiO_2 \geq 0.21$).

The arterial oxygen content (CaO_2) and the venous content (CvO_2) can be calculated from equations 2.9a-b, which separate the contributions from bound and dissolved oxygen content.

$$CaO_2 = \left(\varphi \cdot \left[Hb\right] \cdot SaO_2\right) + \left(PaO_2 \cdot \varepsilon\right) \qquad [2.9a]$$

$$CvO_2 = \left(\varphi \cdot \left[Hb\right] \cdot SvO_2\right) + \left(PvO_2 \cdot \varepsilon\right) \qquad [2.9b]$$

where φ represents the O_2 carrying capacity of haemoglobin, [Hb] the concentration of haemoglobin, and ε is the solubility coefficient of oxygen in blood. All of which can be well approximated in healthy subjects from standard values.

If it is assumed (as is reasonable for a hyperoxic stimulus) that there is no change in $CMRO_2$, then CvO_2 can also be expressed as CaO_2, less the oxygen content extracted metabolism at baseline.

$$CvO_2 = CaO_2 - \left(CaO_{2,0} \cdot OEF\right) \qquad [2.10]$$

where the oxygen extraction fraction is defined as:

$$OEF = \left(CaO_2 - CvO_2\right)/CaO_2 \qquad [2.11]$$

Re-arranging equation 2.9b and substituting equation 2.10 in for CvO_2 leads to an expression for SvO_2 where the only unknowns are PvO_2 and OEF.

$$SvO_2 = \frac{CaO_2 - \left(CaO_{2,0} \cdot OEF\right) - \left(PvO_2 \cdot \varepsilon\right)}{\varphi\left[Hb\right]} \qquad [2.12]$$

This is an important step in the derivation of the calibration process, as $1\text{-}SvO_2$ is proportional to the blood susceptibility, as shown in equation 1.1. The dissolved oxygen on the venous side ($PvO_2 \cdot \varepsilon$) is expected to be very small (<1%), and so can be ignored. Therefore the fractional change in blood susceptibility can be expressed as $1\text{-}SvO_2/1\text{-}SvO_{2,0}$, or:

$$\frac{\chi_{blood}}{\chi_{blood,0}} = \frac{\varphi \cdot \left[Hb\right] - CaO_2 + \left(CaO_{2,0} \cdot OEF\right)}{\varphi \cdot \left[Hb\right] - CaO_{2,0}\left(1 - OEF\right)} \qquad [2.13]$$

The arterial oxygen content at rest ($CaO_{2,0}$) and stimulation (CaO_2) can be calculated from the partial pressure of end-tidal oxygen as described previously. Thus, the only unknown value necessary to calculate $\chi_{blood}/\chi_{blood,0}$ is the oxygen extraction fraction (OEF). In healthy subjects, PET measurement of OEF has found it to be surprisingly

consistent throughout the brain and across subjects (Perlmutter et al., 1985). Because of this Chiarelli et al. suggested using a PET derived value of 0.3 to calibrate the BOLD signal and estimate M.

In addition, to the simple model derived here, Chiarelli et al. also present an expanded version that accounts for small reductions in CBF; while Gauthier and Hoge (Gauthier and Hoge, 2013) introduced a new model to account for arbitrary changes in CBF, as shown below.

$$\frac{\Delta BOLD}{BOLD_0} = M\left[1-\left(\frac{CBF}{CBF_0}\right)^{\alpha}\left(\frac{\chi_{blood}}{\chi_{blood,0}}\right)^{\beta}\right] \qquad [2.14]$$

The hyperoxic method of calibrating the BOLD signal has several advantages over hypercapnia in terms of its effect on physiology. As a result it is much more easily tolerated by subjects, resulting in far fewer subject drop-outs. However, there is still ongoing debate as to whether oxygen can truly be considered an iso-metabolic stimulus (Xu et al., 2012a). There are a number of reports from various techniques and animal models that claim both an increase in $CMRO_2$ (Rockswold et al., 2010), a decrease (Richards et al., 2007) and no change (Diringer et al., 2007). Thus, while there is yet to be a definitive answer regarding the use of oxygen as an iso-metabolic challenge, its effect on metabolism is likely to be small and the method has become established within the calibrated fMRI community.

Perhaps a more significant drawback to the hyperoxic calibration method is the need to assume a value of OEF. While this may only introduce a small error in healthy subjects, it restricts the use of this method to non-clinical investigations, severely restricting its

usefulness. Fortunately, as identified by Bulte et al (Bulte et al., 2012) and Gauthier and Hoge (Gauthier and Hoge, 2012), this dependence on OEF can in fact be exploited to great benefit if a hyperoxic calibration is combined with a hypercapnic calibration.

2.4 Serial Hyperoxic and Hypercapnic Measurement of OEF and $CMRO_2$

The two previous sections have described alternative ways of calculating M, and from there a task-related change in $CMRO_2$. As described previously, this calibration process allows task-related BOLD changes to be compared across differing subject groups in a meaningful manner. However, it has been shown that by combining these two calibration techniques it is possible to calculate the resting OEF and rate of oxygen metabolism ($CMRO_{2,0}$) (Bulte et al., 2012; Gauthier and Hoge, 2012). As discussed in the introductory section, PET measurement of OEF and $CMRO_2$ has been shown to be a powerful biomarker for assessing diseases such as stroke, Parkinson's and Alzheimer's. The ability to obtain the same information with a truly non-invasive technique, such as calibrated fMRI, is an attractive proposition. In this section the methodology proposed by Bulte et al. is examined and a relationship between the change in fractional blood susceptibility and OEF is derived.

The Bulte calibration method relies on the fact that the hypercapnia calibration method is independent of OEF, while the hyperoxic calibration is not. If both methods are used to measure the value of M, then they should only be in agreement if the correct OEF is used in the hyperoxic calibration. So while, in a traditional hyperoxic calibration the value of OEF must be assumed, in a joint calibration it can be calculated when there is a unique

solution for M. A straightforward method to calculate OEF is to feed a hypercapnic measurement of M into the hyperoxia calibration method.

By re-arranging the hyperoxia calibration equation (2.7) we get an expression for the fractional change in blood susceptibility ($\chi_{blood}/\chi_{blood,0}$) due to a hyperoxic challenge.

$$\frac{\chi_{blood}}{\chi_{blood,0}} = \left[1 - \frac{\left(\frac{\Delta BOLD}{BOLD_0}\right)}{M}\right]^{1/\beta} \qquad [2.15]$$

where M can be determined from a traditional hypercapinc challenge, and the BOLD signal change is measured from a hyperoxic challenge.

Having defined the fractional susceptibility change, this can be combined with measurements of end-tidal oxygen content to calculate OEF. Re-arranging equation 2.13 provides an algebraic solution for OEF from $\chi_{blood}/\chi_{blood,0}$.

$$OEF = \frac{\varphi \cdot [Hb] - CaO_2 + \frac{\chi_{blood}}{\chi_{blood,0}}\left(CaO_{2,0} - \varphi \cdot [Hb]\right)}{CaO_{2,0}\left(\frac{\chi_{blood}}{\chi_{blood,0}} - 1\right)} \qquad [2.16]$$

where the arterial oxygen content at rest ($CaO_{2,0}$) and stimulation (CaO_2) can be calculated from the partial pressure of end-tidal oxygen as before. The equations presented in (Bulte et al., 2012) include a correction term for small reductions in CBF, which have been left out of this analysis for simplicity. However, the hyperoxia calibration method can be extended to include arbitrary changes in CBF, via the use of equation 2.14 instead of 2.7 in the initial calculation of $\chi_{blood}/\chi_{blood,0}$.

The calculated oxygen extraction faction can be combined with a measure of resting CBF to estimate the resting $CMRO_2$. The absolute rate of cerebral metabolism is defined as:

$$CMRO_2 = VO_2 + CIO_2 \qquad [2.17]$$

where VO_2 is the oxygen consumption by the brain and CIO_2 is the amount of oxygen accumulated in brain tissue, which under normal conditions is negligible (Reich, 2011). Therefore, $CMRO_2$ is approximately equal to the oxygen consumption (VO_2), and can be expressed as:

$$CMRO_2 = CBF\left(CaO_2 - CvO_2\right) \qquad [2.18]$$

By substituting in for the oxygen extraction fraction (equation 2.11) $CMRO_2$ can be expressed in terms of resting CBF, OEF and CaO_2 (all of which can be measured).

$$CMRO_2 = CBF \cdot OEF \cdot CaO_2 \qquad [2.19]$$

The arterial oxygen content (CaO_2) can be calculated from the Severinghaus equation and equation 2.9a, while resting CBF can be calculated from rest periods in the ASL data. Although single-TI ASL data can in theory be used to estimate resting CBF (Wong et al., 1998), the use of multiple inversion times (multi-TI) provides a more robust calculation (MacIntosh et al., 2010; Wong et al., 1997). Because of this Bulte et al included a multi-TI ASL measurement in their protocol, providing quantitative estimates of $CMRO_2$.

As with all calibration methods based on the Davis model, a value of β must be assumed to calculate M and therefore OEF. However, there is an inherent contradiction in assuming a fixed value of β and fitting for M. The Monte-Carlo modelling on which the Davis model is based (Boxerman et al., 1995; Ogawa et al., 1993) shows that both β and

K (and therefore M) must vary with vessel size. So that, as the vessel size increases, M increases and β decreases. Thus, if a fixed β value is assumed, the associated M value will be in error if β does not match the vessel scale under investigation. This error in M will obviously feed forward to an error in the calculated OEF in the joint calibration method. Indeed, sensitivity analysis in (Gauthier and Hoge, 2012) demonstrates that a hypercapnic/hyperoxic estimate of OEF can vary by approximately 25% as β is varied from 2 to 1. While the mean vessel size across the brain is fairly consistent in healthy subjects (Kiselev et al., 2005), it has been shown to change dramatically in diseases such as tumour (Lemasson et al., 2013; Tropres et al., 2004b) and stroke (Bosomtwi et al., 2008; Xu et al., 2011). Therefore, while it may be possible to select a representative vessel scale, and associated β value, in healthy tissue, variation in vessel scale must be accounted for in disease states. Due to such considerations Wise et al. (Wise et al., 2013) have recently proposed a multiple gas challenge technique to simultaneously quantify α, β and M.

Chapter 3

Vessel Size Imaging

Chapter 2 demonstrated how an estimate of the resting OEF could be made with a combined hypercapnic/hyperoxic calibration of the BOLD signal. However, this methodology was found to be limited because of the need to assume a vessel size, via the fitting parameter β. In this chapter MR methods for determining voxelwise estimates of vessel size are investigated. In addition to providing vessel scale information for model fitting, the vessel size is a useful biomarker for assessing disease state and progression. The mean vascular density (mean vessel size/blood volume) is the gold standard for histological assessment of angiogenesis (Tahergorabi and Khazaei, 2012). In addition, measurements of mean vessel size in-vivo have been correlated with various disease states (Dennie et al., 1998; Hsu et al., 2009; Xu et al., 2011) and have shown a high correlation with histological measures (Lemasson et al., 2013).

3.1 Spin Echo Signal

Thus far all consideration of BOLD contrast has been focused on the gradient-echo (GE) signal. However, MR modelling studies (Bandettini and Wong, 1995; Boxerman et al., 1995; Dickson et al., 2011; Fujita, 2001) demonstrate a complex vessel size dependence of the BOLD spin-echo (SE) signal. To understand this vessel size dependence it is helpful to consider equation 1.7, which describes the extravascular frequency shift due to a susceptibility difference (intra to extravascular). Aside from the dependence on the

susceptibility difference, the frequency shift is also dependent on $(a/r)^2$, where a is the vessel radius and r is the distance from the vessel. This means that for small vessels there is a sharp change in extravascular precession frequency over a small distance, but a much more gradual change in frequency around large vessels. Figure 3.1 shows how these two different scenarios (small versus large vessels) produce different dephasing effects in the extravascular space.

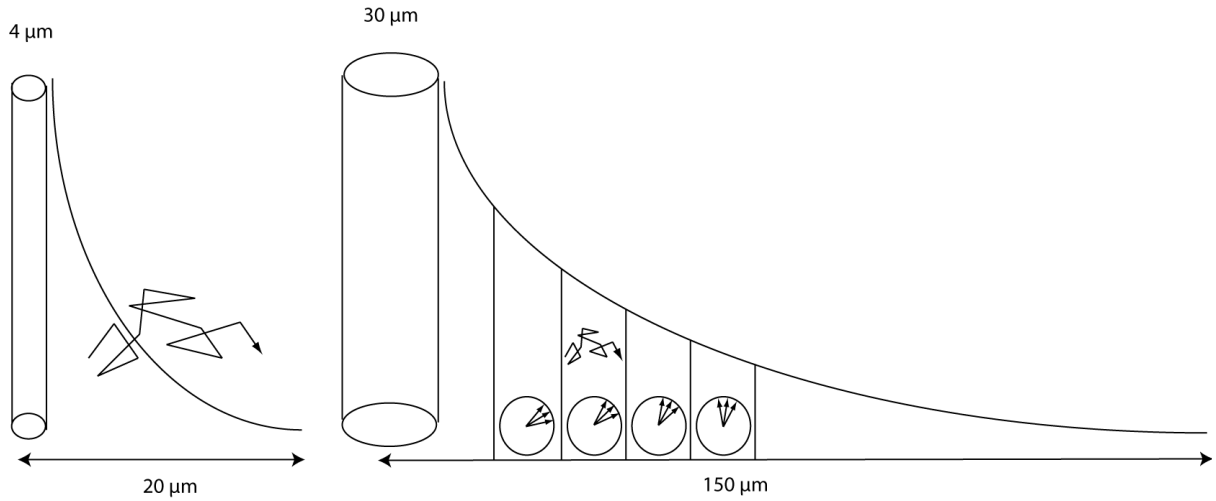

Figure 3.1 Extravascular dephasing effects from a 4 μm radius capillary and a 30 μm radius venule (adapted from Kim Seong-Gi Principles of Functional MRI).

A typical water molecule will diffuse approximately 20 μm during a TE of 80 ms, as can be seen in figure 3.1. The change in precession frequency around small vessels is relatively large over this distance. Therefore spins diffusing in the extravascular space sample many different precession frequencies. This sampling of frequencies results in a dynamic averaging effect and a loss of phase coherence that cannot be refocused with a SE experiment, thus producing an irrecoverable loss of signal. However, in the case of large vessels the change in precession frequency is relatively small over the diffusion

distance. This means that a positional dependent phase will be accrued during TE, approximating the static dephasing regime. Thus, a significant part of the signal around large vessels can be refocused with a 180º RF pulse. The total signal loss around any vessel can be considered as a combination of dynamic averaging and static dephasing effects; with larger vessels more closely approaching the ideal static dephasing regime where all the dephasing effects can be refocused. This vessel size dependence is maintained for a change in intravascular susceptibility, as shown in figure 3.2, where vessel size is plotted against the change in relaxation rate at 3T (χ_0=0.45ppm, $\Delta\chi$=-0.1 ppm, CBV=0.03, diffusion=0.67 μm^2/ms, TE=80 ms).

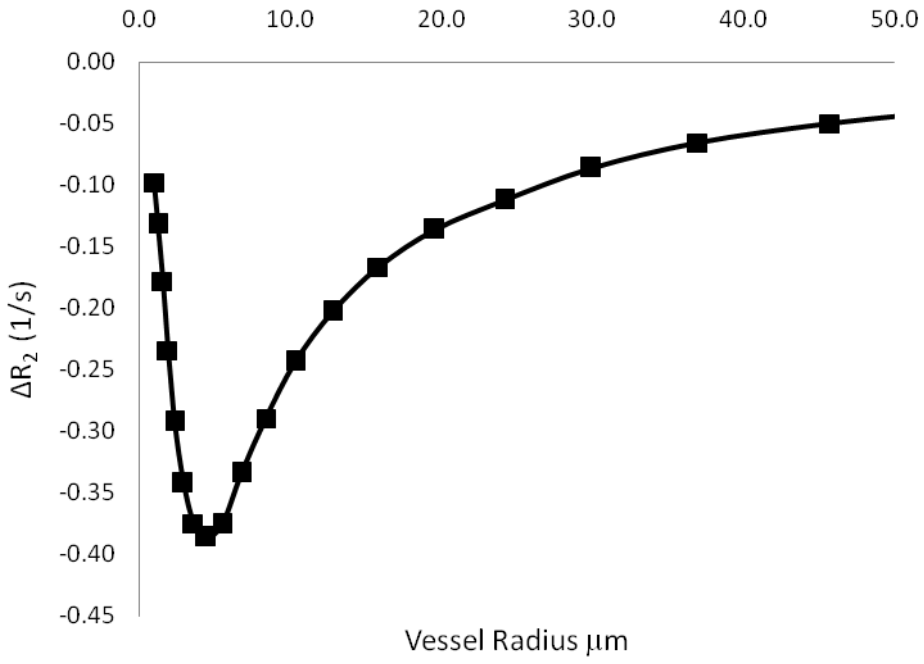

Figure 3.2 Monte-Carlo model of the change in spin-echo relaxation rate arising from extravascular water at 3T due to an intravascular susceptibility change. (χ_0=0.45 ppm, $\Delta\chi$=-0.1 ppm, CBV=0.03, diffusion=0.76 μm^2/ms, TE=80 ms.)

The data in Figure 3.2 was generated using a Monte-Carlo model to calculate the MR signal arising from diffusing spins in a vascular network. The Monte-Carlo modelling was performed as per (Jochimsen and Moller, 2008). The ODIN C++ NMR framework (Jochimsen and von Mengershausen, 2004) was used to perform the simulations for this data, and in all other NMR signal modelling presented in this thesis. The ODIN framework allows for the simulation of an MR sequence acting on a virtual sample. Where the virtual sample holds spatially resolved NMR-specific properties (spin density, relaxation rates T1 and T2, and frequency offset). By playing out the specified sequence the simulation is performed on the virtual sample. During the simulation an exact solution of the Bloch equations (for piecewise constant fields) is used to calculate the magnetization vector at each point of the sample recursively. During acquisition periods, a virtual NMR signal is generated by integrating over the transverse component of the magnetization vector for all points within the virtual sample. As with previous studies, (Boxerman et al., 1995; Fisel et al., 1991), the virtual sample representing the vasculature was modelled as a fully permeable, randomly-oriented, cylinder of infinite length. Multiple samples were simulated for different vessel radii (1-60 μm), while random vessel orientations were accounted for by varying the angle between the main field and the cylinder in the range from 0 to $\pi/2$ (in 64 linear steps). A $\sin\theta$ weighting was applied to the signal values to account for the density of possible vessel angles with respect to the static field. Because the field is invariant along the cylinder, simulations were only performed in a 2D plane perpendicular to the cylinder's axis. The area of the simulated plane (A) was adjusted to match the required intravascular volume fraction, where $A=\pi\cdot(\text{radius})^2/\text{CBV}$. The shift in precession frequencies in the intra and extravascular

space of the virtual sample were calculated according to equations 1.6 and 1.7 respectively. Intravascular signal attenuation due to the compartmentalization of haemoglobin was accounted for with a saturation dependent T_2, as per (Jochimsen et al., 2010) and (Shen et al., 2011). For each simulated radius and vessel orientation 100,000 random walks were simulated from randomly seeded starting points. The step size of each simulation was 1 ms, with the displacement at each step generated by a Gaussian random distribution to represent isotropic diffusion. Diffusion was assumed to be 0.76 $\mu m^2/ms$, as is typical in gray matter measurements (Jensen and Chandra, 2000), while the baseline haemoglobin saturation was assumed to be 0.6. For a given set of parameters (resting susceptibility, susceptibility change, blood volume) each vascular simulation took approximately 4-5 hours, running on a virtualised installation of NeuroDebian (hardware: 2.4 GHz Intel Core 2 Duo).

As can be seen from figure 3.2, the magnitude of the change in relaxation rate, ΔR_2, initially increases with vessel size, as more extravascular spins are affected by the susceptibility difference. However, at a radius of approximately 5 μm, ΔR_2 plateaus and begins to decrease again. This decrease in ΔR_2 is due to a gradual shift towards the static dephasing regime, where the accrued phase can be refocused. The vessel size dependence described in figure 3.2 means that the extravascular SE-BOLD contrast at 3T is heavily dominated by small vessels.

While this discussion has only considered the extravascular contributions (as this is the dominant vessel size effect), there will obviously be an intravascular contribution as well. The dephasing caused by the angular dependence of the intravascular frequency shift can be refocused, as this is a T_2' effect. However, the dephasing of intravascular spins due to

the compartmentalisation of intravascular haemoglobin arises due to dynamic averaging and is similar to the effect of very small vessels. Thus the signal loss caused via this mechanism cannot be easily refocused. Figure 3.3 shows how the inclusion of intravascular signal into the Monte-Carlo model affects ΔR_2 at 3T.

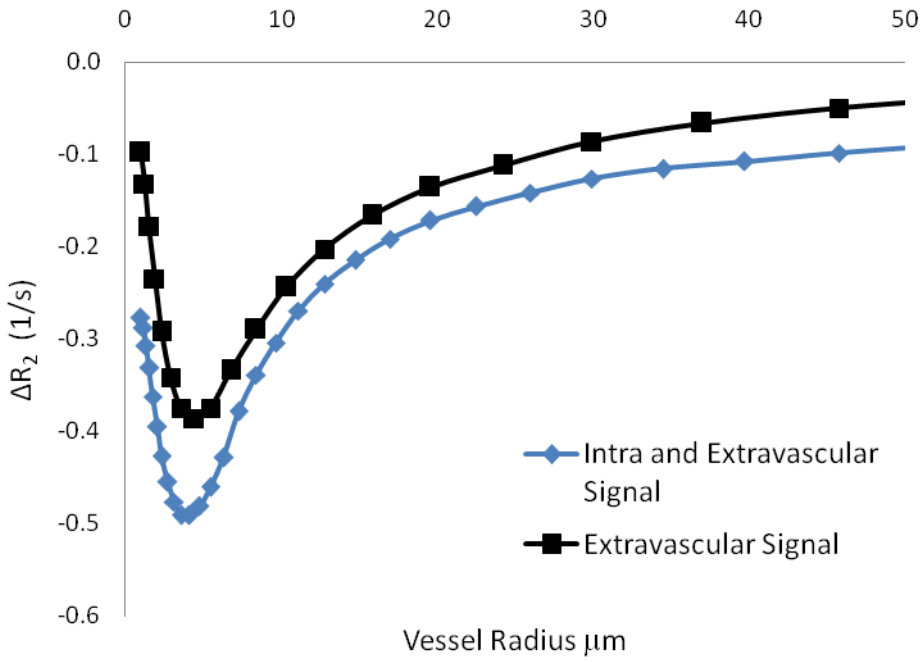

Figure 3.3 Monte-Carlo model of the change in spin-echo relaxation rate arising from extravascular and intravascular water at 3T due to an intravascular susceptibility change. (χ_0=0.45 ppm, $\Delta\chi$=-0.1 ppm, CBV=0.03, diffusion=0.76 μm^2/ms, TE=80 ms.)

Inclusion of the intravascular signal has increased ΔR_2 while leaving the vessel size dependence largely unaffected. The increase in ΔR_2 is predominately caused by including the effect of compartmentalized haemoglobin, which is independent of vessel size. The exact correspondence between vessel size and ΔR_2 is dependent on the blood susceptibility, the spin-echo time, extravascular diffusion rate, and field strength. If the modelling is extended to 7T (figure 3.4) then the peak ΔR_2 is shifted down to

approximately 3 µm. Above 3 µm the difference between the extravascular and total model is almost zero. Given the typical human capillary has a radius of 4 µm (Freitas, 1999) the intravascular signal is insignificant for human studies at 7T. This phenomenon is due to the dramatic decrease in intravascular T_2 with field strength, where the blood T_2 and field strength are thought to be quadratically related (Wright et al., 1991). The resting intravascular T_2 of venous blood at 3T is approximately 32 ms (Zhao et al., 2007), decreasing to 8 ms at 7T (Jochimsen et al., 2010).

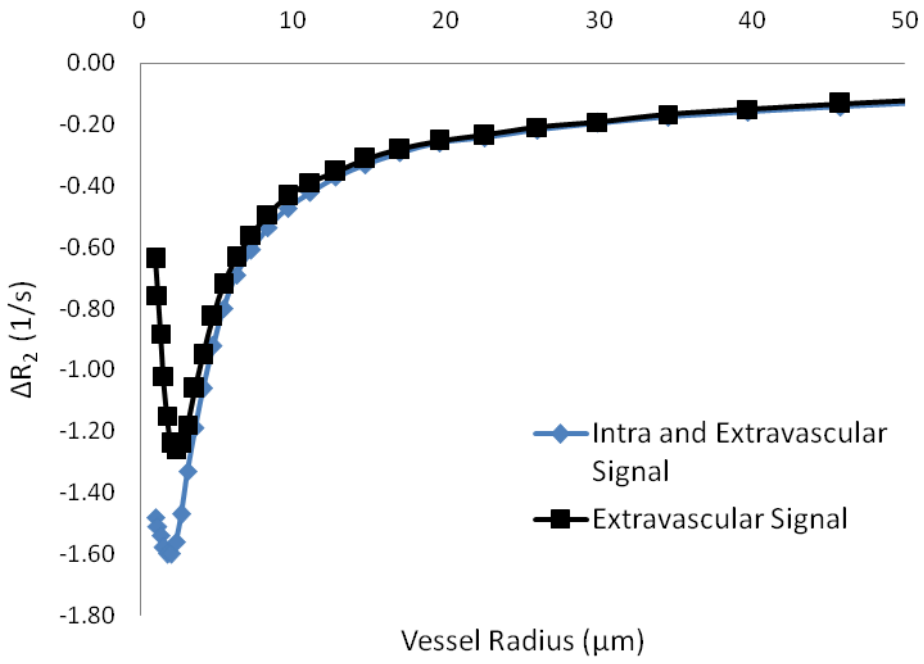

Figure 3.4 Monte-Carlo model of the change in spin echo relaxation rate arising from extravascular and intravascular water at 7T. (χ_0=0.45 ppm, $\Delta\chi$=-0.1 ppm, CBV=0.03, diffusion=0.76 µm^2/ms, TE=55 ms.)

Decreasing the field strength to 1.5 T (figure 3.5) dramatically increases the intravascular contribution, which is maintained even for large vessel scales. When partial voluming with draining veins is considered, the intravascular signal becomes the dominant source

of SE-BOLD contrast at 1.5T (Oja et al., 1999). This increase in intravascular signal can again be explained by the blood T_2, which is approximately 181 ms at rest (Barth and Moser, 1997).

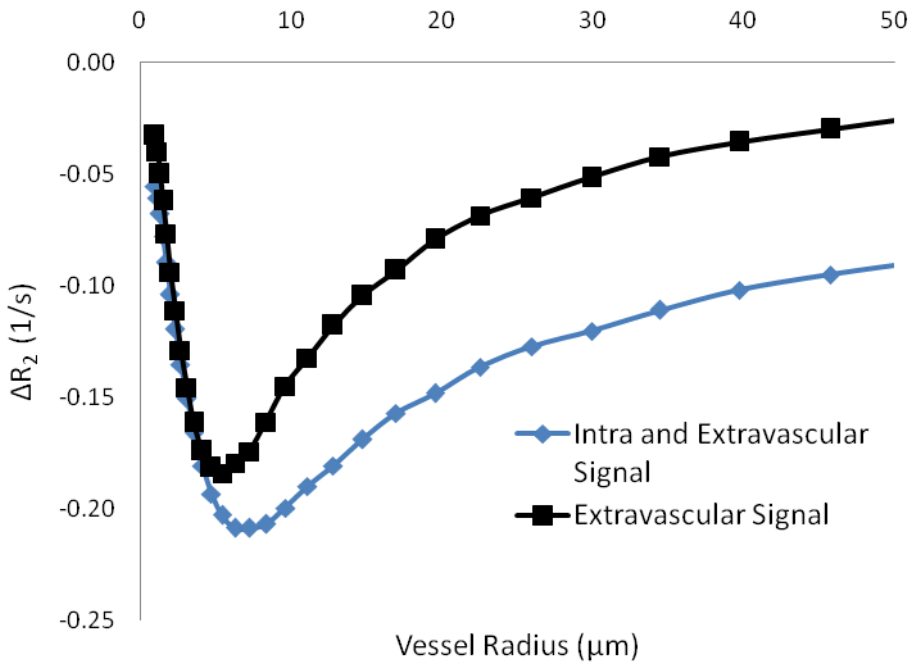

Figure 3.5 Monte-Carlo model of the change in spin-echo relaxation rate arising from extravascular and intravascular water at 1.5T. (χ_0=0.45 ppm, $\Delta\chi$=-0.1 ppm, CBV=0.03, diffusion=0.76 μm^2/ms, TE=110 ms.)

As with the GE models in chapter 1, a number of analytical SE models have been developed that take into account various aspects of the susceptibility induced SE response. One of the more popular models is the slow diffusion approximation proposed by Kiselev and Posse (Kiselev and Posse, 1999). The slow diffusion model considers both the extravascular and intravascular signal contributions; however the compartmentalization of haemoglobin is ignored, heavily weighting the model to extravascular contributions. The slow diffusion approximation means that during TE, extravascular water molecules

experience no change in field gradient. This is a reasonable approximation with large vessels, or with large intra/extravascular susceptibility differences; as in both scenarios the rate of change in the induced magnetic field gradient is small compared to the water diffusion distance. The assumptions used in the slow diffusion model lead to equation 3.1.

$$\Delta R_2 \approx 0.694 \cdot \delta\omega^{2/3} \cdot D^{1/3} \cdot CBV \cdot r_V^{-2/3} \qquad [3.1]$$

where $\delta\omega=2\pi\gamma\Delta\chi B_0$ and is the spread of precession frequencies at the surface of a cylinder perpendicular to B_0, D is the rate of diffusion in the extravascular space and r_V is the mean vessel radius.

Equation 3.1 has a dependence on $r_V^{-2/3}$, thus displaying the expected reduction in SE signal with increasing vessel size. Figure 3.6 shows the agreement between the slow diffusion spin-echo model and an extravascular Monte-Carlo model of ΔR_2 due to an injection of contrast agent ($\Delta\chi$=1.26 ppm). The change in relaxation rate appears to be fairly well described by the slow diffusion model; showing reasonable agreement with the MC model above approximately 2.5 μm. Below 2.5 μm the signal is in the so-called fast diffusion regime, and appropriate modelling is needed to avoid gross overestimation of ΔR_2. Thus, under the assumption of r_V>2.5 μm and minimal intravascular contribution, the slow diffusion approximation appears to be valid for injections of contrast agent. The neglect of the intravascular contribution to the SE signal was demonstrated to have minimal influence by Kiselev (Kiselev et al., 2005). This is due to the relatively large change in extravascular signal and the extreme shortening of intravascular T_2 caused by the contrast agent. Thus the situation is similar to that presented in figure 3.4, where the total model is well approximated by considering only extravascular contributions.

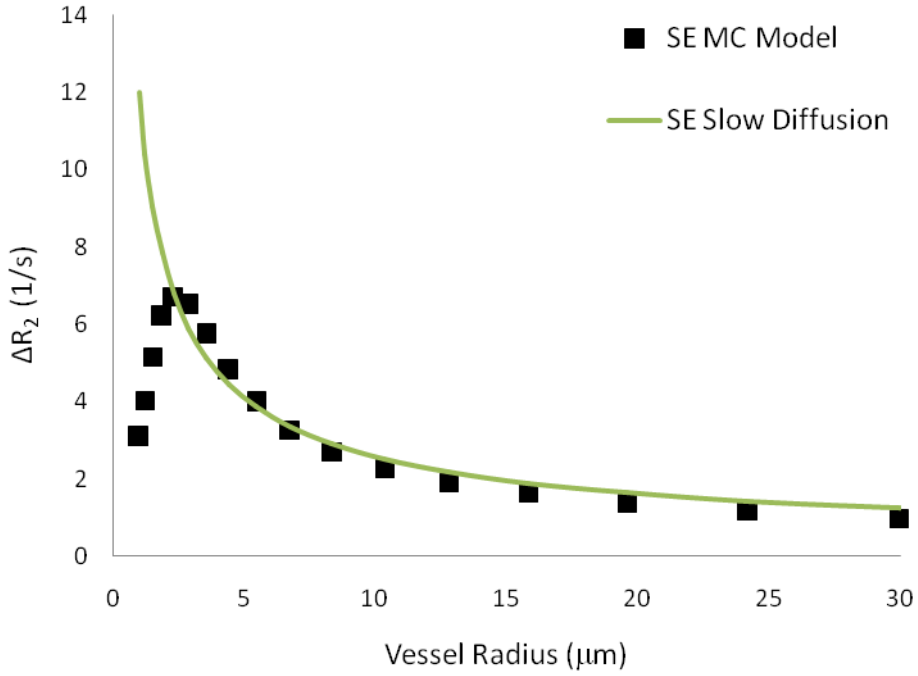

Figure 3.6 Slow Diffusion and extravascular Monte-Carlo model of the change in spin echo relaxation rate due to an injection of contrast agent at 3T. (χ_0=0.45 ppm, $\Delta\chi$=1.26 ppm, CBV=0.03, diffusion=0.76 μm^2/ms, TE=80 ms.)

3.2 Contrast Agent Modelling

While the magnitude of the spin-echo signal is related to vessel size, it cannot easily be used as a direct probe of the vasculature as the signal is also dependent on several physiological properties (e.g. CBV, $\Delta\chi$, and the diffusion rate). However, by combining a SE measurement with a GE measurement the dependence on CBV can be divided out. This is possible because both ΔR_2* and ΔR_2 have a near linear dependence on CBV (Boxerman et al., 1995; Ogawa et al., 1993). Taking advantage of this, Tropres et al. (Tropres et al., 2001) derived a simple algebraic expression for the mean vessel size within a voxel. The equation is based on a combination of the slow diffusion model for

SE acquisitions (equation 3.1) and the static dephasing model for GE acquisitions (equation 3.2).

$$\Delta R_2^* = \frac{2}{3} \cdot \delta\omega \cdot CBV \qquad [3.2]$$

Similar to the slow diffusion model, the static dephasing regime is only accurate when r_V is large or there is a significant change in intravascular susceptibility. As shown in figure 3.7, the static dephasing regime is reasonably accurate above a radius of approximately 3 μm (for an injection of contrast agent at 3T). However, there is still some discrepancy with the MC model until approximately 25-30 μm.

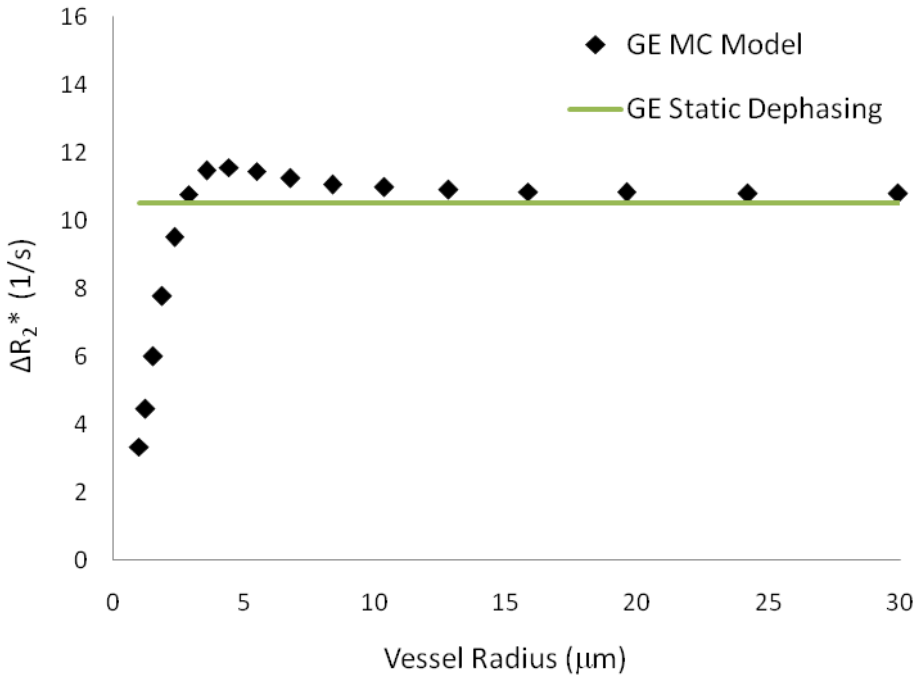

Figure 3.7 Static dephasing model of ΔR_2^* for a contrast agent injection at 3T compared to an extravascular Monte-Carlo model (χ_0=0.45 ppm, $\Delta\chi$=1.26 ppm, CBV=0.03, diffusion=0.76 μm^2/ms, TE=30 ms).

Combining equations 3.1 and 3.2 leads to a simple expression for r_V (equation 3.3), where all the variables except $\Delta\chi$ can be measured with standard MRI measurements. However, the change in intravascular susceptibility can be readily estimated from the concentration of the injected contrast agent (Tropres et al., 2001).

$$r_V = 0.425\left(\frac{D}{\gamma\Delta\chi B_0}\right)^{1/2}\left(\frac{\Delta R_2^*}{\Delta R_2}\right)^{3/2} \qquad [3.3]$$

It should be noted that modelling by Dennie et al. (Dennie et al., 1998) suggests that r_V has a linear relationship with $\Delta R_2^*/\Delta R_2$, rather than a power relationship as described above. To estimate the vessel size, Dennie et al. performed Monte-Carlo modelling of ΔR_2^* and ΔR_2 with a representative diffusion rate and a range of $\Delta\chi$ values. The ratio $\Delta R_2^*/\Delta R_2$ (denoted q) was found to be near-linearly related to r_V and minimally influenced by $\Delta\chi$. Figure 3.8 shows a comparison of the Tropres (slow diffusion) model and Monte-Carlo models with and without intravascular contributions.

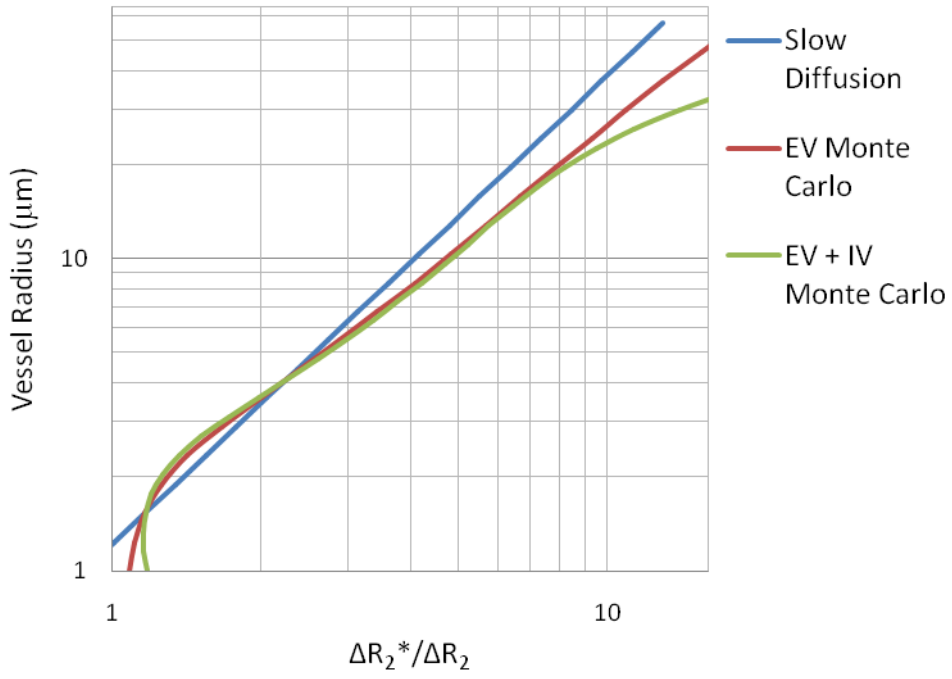

Figure 3.8 Comparison between Monte-Carlo models of $\Delta R_2^*/\Delta R_2$ versus vessel radius and the slow diffusion approximation at 3T (χ_0=0.45 ppm, $\Delta\chi$=1.26 ppm, CBV=0.03, diffusion=0.76 μm^2/ms, GE TE=30 ms, SE TE=80 ms).

As predicted, the inclusion of intravascular signal only has a small influence on the relationship over the majority of vessel scales. However, the slow diffusion model consistently overestimates the vessel radius compared to the Monte-Carlo modelling. This is in agreement with modelling by Kiselev et al. (Kiselev et al., 2005) and with in-vivo validation studies by Farrar et al. (Farrar et al., 2010); which found the Tropres model consistently over-estimated the vessel size compared to both the Dennie model and in-vivo two-photon microscopy. Despite the potential quantitative limitations of the Tropres method, it still shows promise as a clinical tool being easy to implement and showing strong correlation with disease states (Tropres et al., 2004b).

3.3 BOLD-mediated VSI

One potential drawback of contrast based vessel size imaging is that it is sensitive to the entire vascular network, and so is not directly integrable into a BOLD framework; as the BOLD signal is primarily sensitive to the post-capillary vasculature. To overcome this problem a number of studies have experimented with the BOLD contrast to directly determine the venous-weighted vessel size (Jochimsen et al., 2010; Shen et al., 2013). These studies, much like the calibrated BOLD measurements, typically use a gas challenge to alter the deoxy-haemoglobin saturation, and thus the blood susceptibility. This clearly has the advantage of targeting the desired vasculature; however the signal contrast generated by such an experiment is significantly less than induced by an injection of contrast agent. For the small susceptibility changes produced in a BOLD experiment the slow diffusion approximation and static dephasing regime are not valid for the entire range of in-vivo vessel scales. At 3T, as can be seen from figure 3.3, the BOLD SE signal transitions from the fast diffusion to slow diffusion regime on the scale of capillaries (around 5-6 μm). In addition, at 3T, the GE BOLD signal does not reach a plateau until a radius of approximately 10 μm (figure 3.9). Therefore, modelling that includes both fast and slow diffusion components is essential to quantify the expected range of in-vivo vessel scales using a BOLD-mediated VSI study.

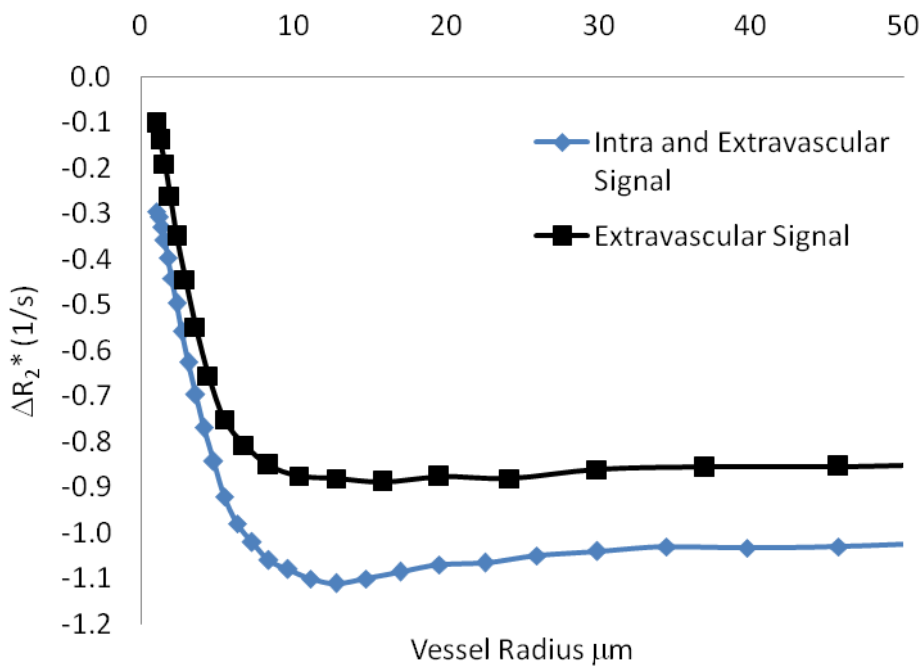

Figure 3.9 Monte-Carlo model of the change in gradient-echo relaxation rate arising from extravascular and intravascular water at 3T. (χ_0=0.45 ppm, $\Delta\chi$=-0.1 ppm, CBV=0.03, diffusion=0.76 μm^2/ms, TE=30 ms.)

A number of models that include fast diffusion effects have been developed, for example (Sukstanskii and Yablonskiy, 2004) and (Ziener et al., 2007). However, as mentioned in chapter 1, none of these models accurately describe the BOLD signal at all vessel scales (Dickson et al., 2011). To overcome these difficulties Jochimsen et al. (Jochimsen and Moller, 2008) employed a similar methodology to Dennie et al., using Monte-Carlo modelling to create a look-up table of the relationship between $\Delta R_2^*/\Delta R_2$ and vessel radius for typical BOLD parameters. As predicted by the modelling of Dennie et al, the magnitude of the susceptibility change and resting blood volume were shown to have minimal impact on this relationship (Jochimsen et al., 2010). Figure 3.10 demonstrates

the effect on the extravascular signal of different combinations of Δχ and CBV for typical physiological values and evoked susceptibility changes.

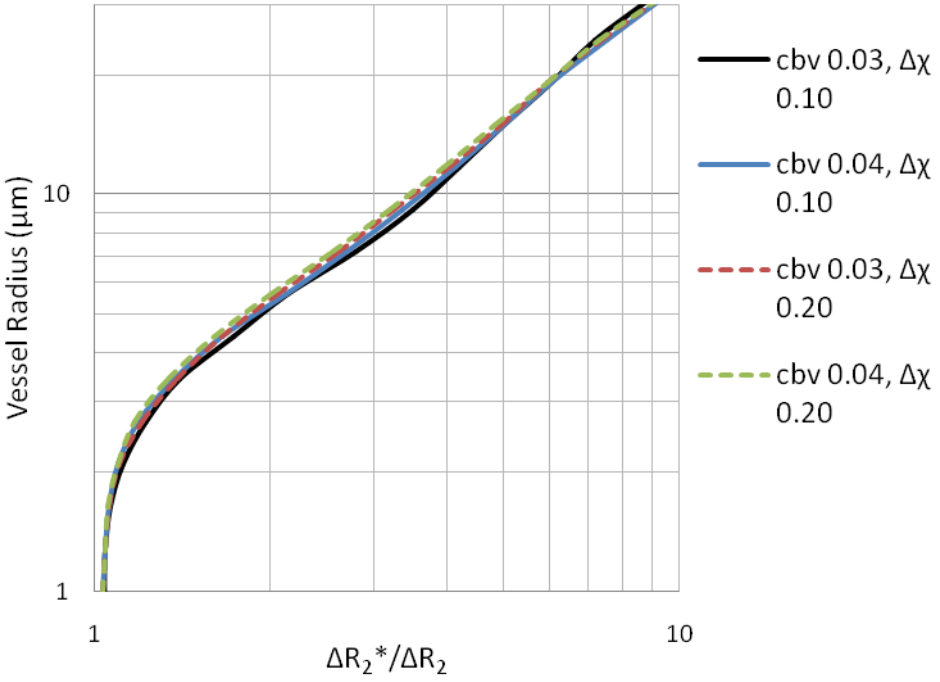

Figure 3.10 Monte-Carlo model of extravascular $\Delta R_2^*/\Delta R_2$ versus vessel radius at 3T with different CBV and susceptibility changes (χ_0=0.45 ppm, diffusion=0.76 μm^2/ms, GE TE=30 ms, SE TE=80 ms).

As predicted, the vessel radius appears to be well defined for all the simulated values and has minimal dependence on either CBV or Δχ. However, inclusion of the intravascular signal (figure 3.11) broadens this relationship, significantly increasing the interaction with Δχ. This dependence on Δχ was not seen in the original work of Jochimsen et al. at either 3T (Jochimsen and Moller, 2008) or 7T (Jochimsen et al., 2010). At 7T the intravascular signal only makes a minimal contribution (as shown in figure 3.4), while at 3T Jochimsen et al. suppressed the intravascular signal with a bipolar gradient.

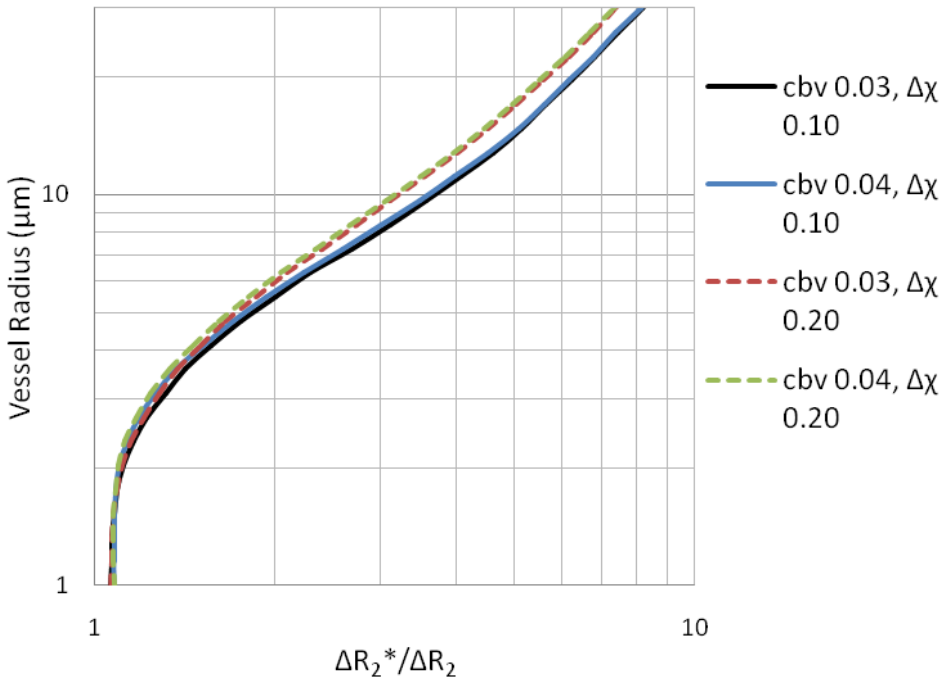

Figure 3.11 Monte-Carlo model of intra and extravascular $\Delta R_2^*/\Delta R_2$ versus vessel radius at 3T with different CBV and susceptibility changes (χ_0=0.45 ppm, diffusion=0.76 μm^2/ms, GE TE=30 ms, SE TE=80 ms).

These figures suggest that the vessel radius can be well defined at 3T with either an extravascular measurement of $\Delta R_2^*/\Delta R_2$, or by including a measurement of $\Delta\chi$. However, this analysis ignores any influence of the baseline susceptibility and assumes an additive change in susceptibility for all stimuli. In chapter 6 the modelling of BOLD-mediated VSI is extended to include the influence of baseline susceptibility and the mechanism of susceptibility change for different stimuli is considered (oxygen and carbon dioxide). From a consideration of these effects a novel method for the simultaneous determination of vessel size and OEF is derived.

In addition to the model restrictions, data analysis methods are of fundamental importance to the validity of vessel size estimates. Studies by Shen et al (Shen et al.,

2013; Shen et al., 2011) have derived substantially different vessel size estimates than presented in Jochimsen's work; the mean vessel size presented in Jochimsen (Jochimsen et al., 2010; Jochimsen and Moller, 2008) being 15.4 μm and the mean vessel size in Shen (Shen et al., 2013; Shen et al., 2011) being 6.5 μm. This large discrepancy is clearly a significant failure of the method and needs to be resolved for there to be any confidence in BOLD-VSI as a quantitative technique. The work presented in chapter 5 investigates the influence of measurement noise on analysis methods as the driver for these differences. The modelling in chapter 5 suggests that a large amount of this variation can indeed be explained by the analysis methods and this is confirmed with in-vivo acquisitions.

Chapter 4

Venous CBV Calculation with Sagittal Sinus Segmentation

4.1 Introduction

The cerebral blood volume is a valuable biomarker and is increasingly being used as a non-invasive measure of angiogenesis (Dunn et al., 2008; Yang et al., 2013). Moreover, combining blood volume with a measurement of vessel size enables the calculation of the mean vessel density (MVD), which is the gold standard in histological assessment of tumour grade. The previous chapters have explored the physiological dependence of the gradient-echo and spin-echo signal in response to a change in blood susceptibility. In all the presented models and simulations there has been a linear, or near linear, signal dependence on blood volume. In this chapter I investigate and expand on a method proposed by Bulte et al. (Bulte et al., 2007a) that exploits this CBV dependence to calculate a venous-weighted CBV.

4.2 CBV Calculation (Theory)

An established MRI method for quantification of total cerebral blood volume is through the infusion of gadolinium contrast agent (Tudorica et al., 2002). The method assumes a linear change in relaxation rate (R_2*) with concentration of contrast agent to derive an expression for fractional CBV (as described in equation 4.1).

$$CBV = h \cdot \frac{\ln\left(S_T(t)/S_{T,0}\right)}{\ln\left(S_a(t)/S_{a,0}\right)} \qquad [4.1]$$

where S_T is the signal in the tissue and S_a is the arterial signal. Because the contrast agent is confined to the plasma, the equation also includes a haematocrit correction factor h (which corrects for the difference between large and small vessels plasma content). The correction factor can be estimated from a measurement of the blood haematocrit as per equation 4.2.

$$h = \left(1 - Hct\right)/\left(1 - Hct_m\right) = \left(1 - Hct\right)/\left(1 - \upsilon \cdot Hct\right) \qquad [4.2]$$

where Hct and Hct_m are the large and microvessel haematocrits, respectively, and υ is assigned a constant value (typically 0.85) from PET studies (Phelps et al., 1979). Thus, by acquiring a time series of data point in the tissue, S_T, and in an artery, S_a, the microvascular CBV may be calculated as per equation 4.1.

In 2007 Bulte et al. applied this equation to BOLD-weighted MRI data to calculate the venous blood volume (CBV_v) using a hyperoxic challenge. As discussed in chapter 1, the change in oxygen saturation due to a hyperoxic challenge is predominately confined to the venous vasculature. Therefore, the reference signal must be taken from a draining vein rather than a feeding artery. In the Bulte method it is suggested that the sagittal sinus is used as a reference as it is sufficiently large to contain a typical fMRI voxel without any partial voluming. Selecting such a reference assumes that the change in oxygen saturation in draining veins is the same as in the BOLD-visible microvasculature. Additionally, as in the original theory of Tudorica et al., it assumes that the intra and extravascular contrast mechanisms are identical. While the assumption of an equal

change in oxygen saturation is reasonable, the contrast mechanisms are known to have different physiological dependencies (as discussed in chapter 1).

Here a new CBV equation is constructed from the Davis model (equation 1.12). While the Davis model is derived from a consideration of the extravascular signal, it has been shown to implicitly include intravascular contributions with a modification of the exponent β, as previously discussed in the introductory chapters. Constructing the equation in this manner has the advantage of making explicit the necessary assumptions in the calculation of CBV. If, as discussed in chapter 2, CBV is assumed to remain constant during a hyperoxic challenge, then equation 1.12 can be re-written as:

$$\Delta R_2^* = K \cdot CBV\left[\left(\chi_{blood}\right)^\beta - \left(\chi_{blood,0}\right)^\beta\right] \qquad [4.3]$$

Now by substituting for the blood susceptibility, as per equation 1.1, we get:

$$\Delta R_2^* = K \cdot CBV \cdot \left(4\pi \cdot Hct \cdot \Delta\chi_{do}\right)^\beta \left[\left(1 - SvO_2\right)^\beta - \left(1 - SvO_{2,0}\right)^\beta\right] \qquad [4.4]$$

Thus, the ratio of relaxation rate changes, microvasculature versus sagittal sinus, may be expressed as:

$$\frac{\Delta R_{2,m}^*}{\Delta R_2^*} = \frac{K_m}{K} \cdot CBV \cdot \frac{Hct_m^{\beta,m}}{Hct^\beta} \frac{\left[\left(1 - SvO_2\right)^{\beta,m} - \left(1 - SvO_{2,0}\right)^{\beta,m}\right]}{\left[\left(1 - SvO_2\right)^\beta - \left(1 - SvO_{2,0}\right)^\beta\right]} \qquad [4.5]$$

where *m* denotes signal from the microvasculature and the blood volume in the reference voxel is taken to be 1. If β_m is assumed to equal β and K_m is taken to be equal to K, the cerebral blood volume can be calculated as shown below.

$$CBV = \left(\frac{Hct}{Hct_m} \right)^{\beta,m} \cdot \frac{\Delta R^*_{2,m}}{\Delta R^*_2} \qquad [4.6]$$

Given that the change in transverse relaxation rate may be expressed as in equation 4.7, it follows that the venous CBV can be estimated with equation 4.8.

$$\Delta R^*_2 = -\frac{\ln\left(S(t)/S_0\right)}{TE} \qquad [4.7]$$

$$CBV = \left(\frac{1}{\upsilon} \right)^{\beta} \cdot \frac{\ln\left(S_m(t)/S_{m,0}\right)}{\ln\left(S(t)/S_0\right)} \qquad [4.8]$$

Comparing equation 4.8 with equation 4.1 we see the only difference is in the haematocrit scaling factor and the exponent β. The difference in the scaling factor arises because the susceptibility change due to deoxy-haemoglobin content is linearly related to the blood haematocrit; while the gadolinium concentration is linearly dependent on the blood plasma. This subtlety was not noted in the original Bulte method and is a source of significant potential error in CBV estimates. The exponent β is also missing from the original derivation as Tudorica et al. assumed that ΔR_2* was linearly related to the contrast agent concentration. The issues presented by equation 4.8 can be solved by using the correct haematocrit scaling factor and an estimated β. However, this derivation also highlights more fundamental shortcomings of the method. In order to reduce equation 4.5 to 4.6 it is necessary to assume a single β value, i.e. $\beta = \beta_m$, and the equivalence of K and K_m. Investigation of the contrast agent method (Newman et al., 2006) suggests that the ratio K_m/K deviates significantly from unity, while, investigation of the BOLD signal in chapter one highlighted the fact that R_2 decay for intravascular blood has a quadratic relationship with susceptibility (equation 1.8). Because intravascular ΔR_2* is dominated

by this effect (Silvennoinen et al., 2003) it has an effective β of 2, while in healthy tissue at 3T β_m is often assumed to be 1.3. These discrepancies in the haematocrit scaling factor, β, and the ratio K_m/K could all lead to significant uncertainty in the Bulte hyperoxic CBV method.

4.3 Vessel Segmentation (Method)

Aside from the theoretical difficulties associated with the Bulte CBV methodology, there is a significant technical challenge in isolating suitable reference voxels within the sagittal sinus. A reference voxel must be contained completely within the vein and avoid the inclusion of any tissue signal, which would result in overestimation of CBV values. One option to select an appropriate reference is to manually select the voxel from the time series data; however this could clearly lead to operator bias. As an alternative, a new method is presented here, which uses an additional time-of-flight acquisition to automatically segment a number of appropriate voxels within the sagittal sinus. The average signal from these segmented voxels can then be used to create a reference without any operator bias.

To provide a high contrast reference image (between venous vessels and tissue) a high resolution 2D time-of-flight (TOF) dataset is acquired. The TOF data is acquired with 4 times the in-plane resolution and twice the through plane resolution of the time series data. Acquiring the data sets with identical field-of-views produces 32 TOF voxels within each time series voxel. A 2D acquisition is used rather than 3D to provide high contrast for the relatively slow moving venous blood (Lee, 2005). An example slice taken from a

2D TOF acquisition is shown below in figure 4.1, where the bright signal from the draining veins is clearly visible.

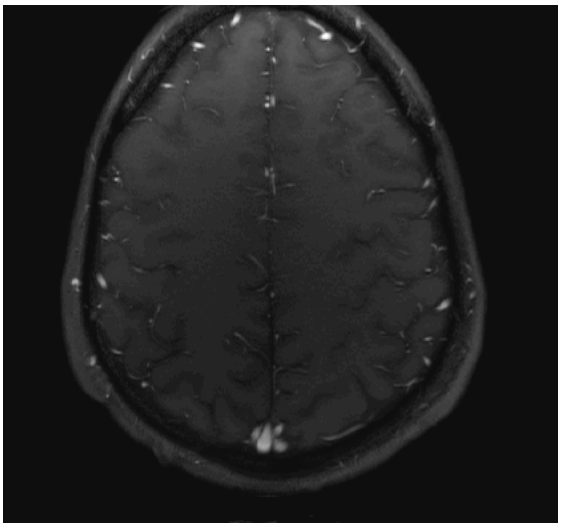

Figure 4.1. Axial slice from 2D time-of-flight acquisition. Signal from venous vessels appears bright.

To extract the desired reference voxels the TOF data is processed with MATLAB (Mathworks, Natick, MA, USA). The first step in the vessel segmentation process is to isolate a volume-of-interest (VOI) that contains the posterior section of the sagittal sinus. The VOI is defined from the edge of the skull (found using Canny edge detection) to a plane 2 cm into the skull (figure 4.2).

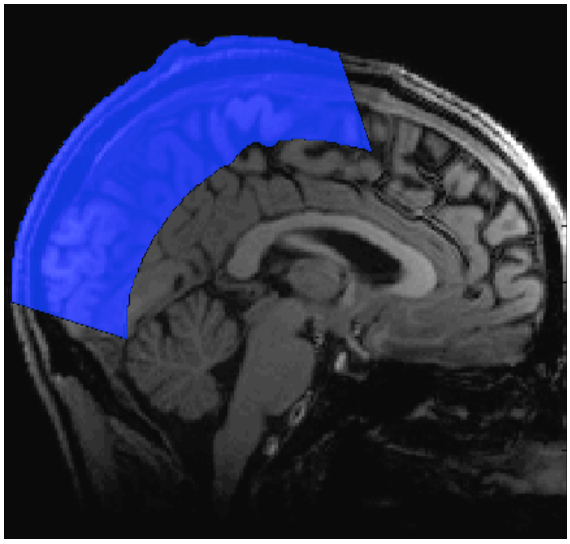

Figure 4.2. Sagittal image with volume-of-interest (blue) extracted using Canny edge detection.

Isolating the sagittal sinus in this way allows a simple thresholding technique to be used to segment out the sinus. Pilot data was used to define a retention threshold of 0.5% of the most intense voxels with the VOI. This level was chosen to be conservative, with segmented voxels in the pilot data including not only the sagittal sinus, but also some of the larger feeding veins (as shown in figure 4.3). The retained voxels are then binarised to produce a vessel mask, as shown below.

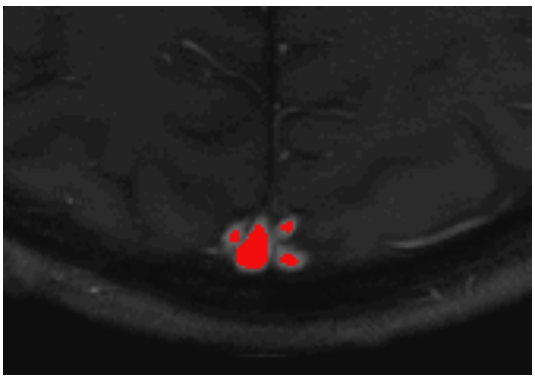

Figure 4.3 Time-of-flight data with vessel mask overlayed (red).

By downsampling the vessel mask to the resolution of the time series data (using linear interpolation) a new mask is created; where the voxel intensities are inversely proportional to the amount of partial voluming (figure 4.4). A voxel in the downsampled data that is completely contained within the sagittal sinus will have a value of 1. Voxels that protrude from the sagittal sinus will be scaled down by the proportion of high-resolution voxels outside the vessel.

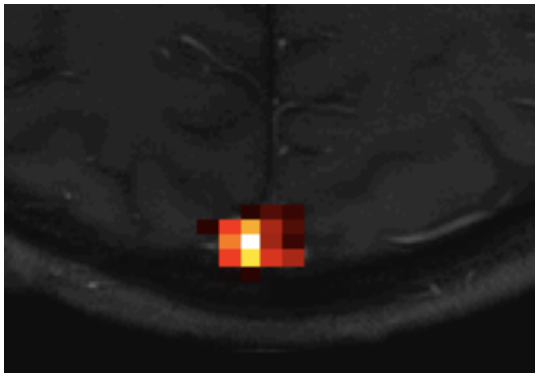

Figure 4.4 Time-of-flight data with low-resolution vessel mask. In-plane partial volume is apparent in voxels at the perimeter of the mask.

By hard thresholding the low-resolution vessel mask, only those voxels without partial voluming can be retained, creating a VOI of venous reference voxels for the time series data (figure 4.5). Figure 4.5b shows a maximum intensity projection of the selected reference voxels. The break in the line indicates that this region contained no voxels that were free from partial voluming.

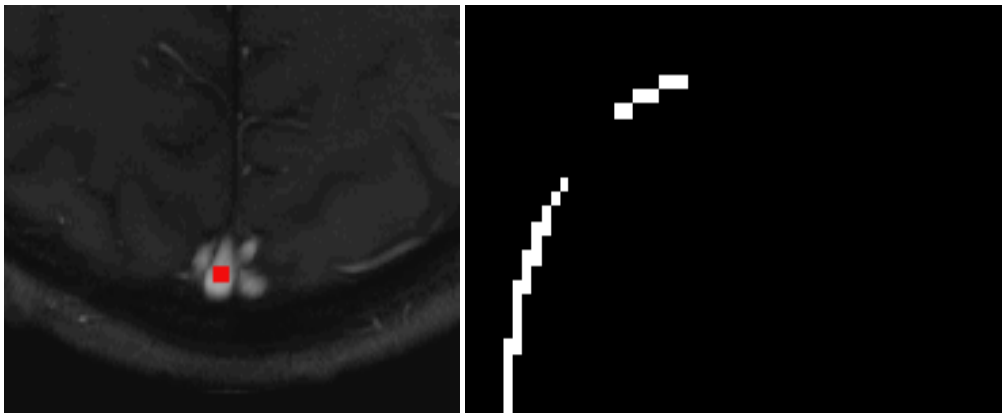

Figure 4.5 (A: Left, B: Right.) A. Low-resolution vessel mask, thresholded to remove in-plane partial volume voxels. B. Maximum intensity projection of vessel mask (sagittal view).

4.4 In-Vivo Validation (Results)

To verify the vessel segmentation process, the method was validated with in-vivo data collected from 4 healthy volunteers. The subjects were scanned using a Siemens 3T Verio system equipped with a transmit body coil and a 32-channel receive head coil, using foam inserts to minimise head motion. Time series data (160 volumes) were collected with a gradient-echo echo-planar imaging (EPI) readout; TR = 3.75 s, TE = 22 ms, 6/8 kspace, flip angle 90°. Twenty-three axial slices in ascending order (3.2×3.2×5 mm^3 voxels, with a 10% inter-slice gap of 0.5 mm) were prescribed. A field map with the same resolution as the EPI sequence was obtained in order to correct for EPI distortion. A 2D time-of-flight volume was acquired with 46 slices (0.8x0.8x2.5 mm^3 voxels with a 10% inter-slice gap), TR = 45 ms, TE = 4.4 ms, flip angle 60°. The 10 minute (160 volumes) paradigm consisted of delivering gasses via a sealed facemask (8920 Series, Hans Rudolph Inc., Kansas City, MO, USA). Two 3-minute blocks of 50% oxygen (mixed with medical air) were alternated with 2x2 minute blocks of medical air. The

gases were delivered via a gas mixing system with a flood chamber (a 2 m long, 10 cm diameter, open-ended tube) acting as a gas reservoir. By delivering the gasses at a high delivery rate (30 L/min) sufficient flow was achieved to flush the reservoir of exhaled gasses and minimise any re-breathing.

The time series data were pre-processed with FEAT (http://www.fmrib.ox.ac.uk/fsl/). The pre-processing steps included motion and distortion correction and high pass temporal filtering (480 s). A registered high-resolution T1-weighted structural data set was processed with the FMRIB FAST tool to produce a gray matter mask. Two different datasets were produced from the EPI data, one with 5 mm FWHM spatial smoothing and one with no spatial smoothing. The data set without smoothing was used for the reference data and the smoothed data was used for the microvascular signal. Smoothing was omitted from the reference data to avoid contamination of the venous signal by the surrounding voxels. Segmentation of the sagittal sinus was performed as described in section 4.2. However, only a subset of the segmented voxels (6 voxels with the largest signal change) was included in the mean reference signal. A subset of the segmented voxels was used due to limitations in the EPI distortion correction, which meant that it was not possible to align all of the EPI voxels with the TOF data. Six voxels were chosen, as this was the largest number that could reliably be registered across all datasets. The baseline and stimulation signals were calculated from the mean signal during plateau periods (i.e. once the signal had reached a steady-state). Equation 4.8 was then used to produce CBV maps of the whole brain and the data were then smoothed using a 3 x 3 Gaussian kernel. The haematocrit correction factor was not included in the calculation of

CBV for ease of comparison with (Blockley et al., 2013), where no haematocrit factor was applied.

In Blockley et al., 2013 an alternative method of using a hyperoxic challenge to measure venous CBV is proposed. Rather than scaling the tissue signal by the change in a blood filled voxel, the change in end-tidal oxygen is used as a scaling factor. In the derivation of the method a linear relationship between tissue signal and deoxyhaemoglobin is employed. Thus it appears to assume that the tissue signal is derived only from extravascular water surrounding large veins (where β can be assumed to equal 1). However, some account of the capillary and intravascular contributions is made by the inclusion of empirically derived linear scaling factors. The method presented by Blockley et al. has an advantage over the Bulte method in that it removes the dependence on OEF from the CBV calculation. However, the validity of the model has only been examined over a narrow range of typical (healthy) vascular parameters.

For each volunteer in the current study the sagittal sinus was successfully segmented from the TOF data with an average signal change of 124% in the selected voxels. The mean grey matter CBV estimated from the 4 volunteers was 7.2% (±2.3). Figure 4.6 shows typical CBV maps obtained from one of the volunteers.

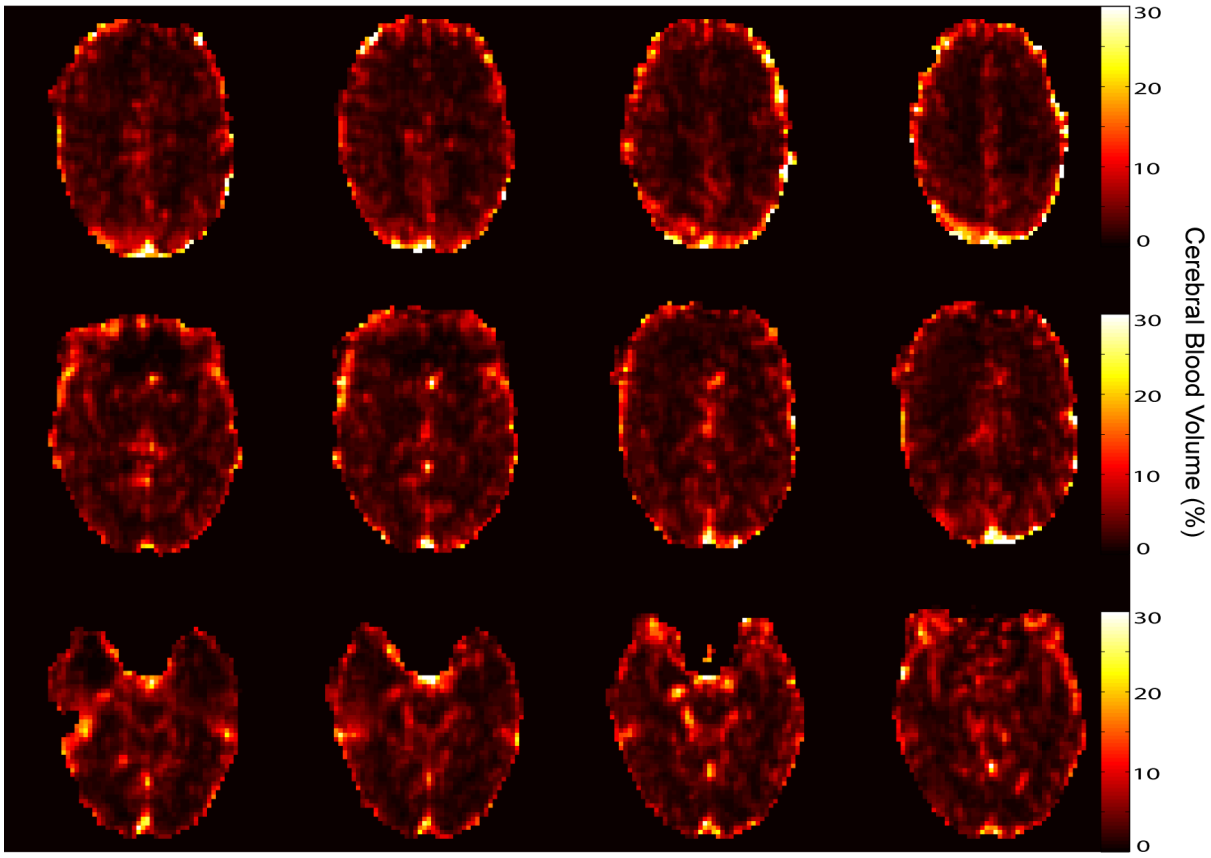

Figure 4.6 Smoothed CBV maps from one volunteer.

The mean gray matter CBV is significantly larger than calculated in previous studies (He and Yablonskiy, 2007; Jochimsen et al., 2010), which estimate a venous blood volume closer to 2-3%. Examination of the data shows that distortion correction, as implemented in FSL, is not robust in and around the sagittal sinus. Because of this a number of segmented voxels did not fall completely within the sinus. To mitigate this effect only those voxels with the highest signal change were used as a reference (as described previously). To investigate any bias caused by this mis-registration a user assisted method was also developed, where fiducial points were manually placed in the descending sinus to track its course. This method was utilised by Blockley et al. (Blockley et al., 2013) to compare the Bulte CBV technique with a new method. The data

in the Blockley paper agrees well with that presented here, with a mean grey matter CBV of 8.24% (±1.14) for the Bulte method. This strong agreement between the results suggests that the automatic segmentation process is not the prime driver for the overestimation of CBV in this method. Instead, the overestimation in CBV appears to be the result of the assumptions used to reduce equation 4.5 to 4.8. If an alternative approach is taken to calculate CBV, and equation 4.5 is used directly, then this overestimation error can be effectively corrected for. Inserting typical physiological values into equation 4.5 ($SvO_2 = 0.6$, $\Delta SvO_2 = 0.05$, Hct = 0.4, $\beta_m = 1.3$, $\beta = 2$ and $K_m/K = 0.69$ (Newman et al., 2006)) produces a correction factor of 0.35 that can be applied to the previous estimates. Using this correction factor, the CBV estimates made here and by Blockley et al. produce grey matter estimates of 2.5% and 2.86% respectively. Thus, producing venous CBV estimates in the expected physiological range. However, it should be noted that such a correction requires not only knowledge of the baseline SvO_2 but also the change in venous oxygen saturation due to the hyperoxic challenge (which is not generally measured in the Bulte methodology).

4.5 Conclusions

Because the TOF and time series data are acquired from matched volumes, the low-resolution mask is implicitly registered to the time series data. However, EPI acquisitions, which would generally be used to acquire R_2*-weighted data, are affected by geometric distortions caused by variations in B_0. By acquiring a map of B_0 these distortions can be corrected for with tools such as FEAT, which is standard practice for fMRI studies. Unfortunately, the performance of these tools was not found to be sufficiently robust to

correct for all distortions in and around the sagittal sinus. A number of solutions to this problem and alternative segmentation processes were investigated. However, given the agreement of the results with Blockley et al. it is apparent that the Bulte CBV method suffers from inherent bias that is independent from the reference voxel selection method. The theoretical limitations discussed in section 4.1 highlights the most likely cause of this bias, in the assumption of a single β value and proportionality constant K. Substitution of typical physiological values into equation 4.5 demonstrated that this bias could effectively be removed with knowledge of the baseline physiology and change in oxygen saturation caused by the stimulus. Alternatively, as proposed by Blockley et al., end-tidal oxygen measurements can be used to convert the tissue signal to CBV. This new methodology avoids the use of the haematocrit scaling factor and the ratio K_m/K. However, it assumes a uniform β_m of 1. As discussed in chapter 2, the assumption of a uniform β value is an implicit assumption of a uniform vessel scale (in this case a large mean vessel radius), which is questionable in healthy tissue and certainly inappropriate for a large number of disease states. In chapter 6 a new venous CBV measurement method is proposed that also uses end-tidal measurements of O_2. However, in this case the mean vessel size per voxel is included in the modelling and calculation of CBV, expanding the applicability of the method and avoiding the bias present in the Bulte methodology.

Chapter 5

The Influence of Noise on BOLD-Mediated Vessel Size Imaging Analysis Methods

Abstract

Vessel size imaging (VSI) is an MRI technique that aims to provide quantitative measurements of tissue microvasculature. An emerging variation of this technique uses the BOLD effect as the source of the imaging contrast. Gas challenges have the advantage over contrast injection techniques in that they are non-invasive and easily repeatable due to the fast washout of the contrast. However, initial results from BOLD-VSI studies are somewhat contradictory, with substantially different estimates of the mean vessel radius.

Due to BOLD-VSI being an emerging technique, there is not yet a standard processing methodology, and different techniques have been employed to calculate the mean vessel radius and reject uncertain estimates. Additionally, the acquisition methodology and signal modelling vary from group to group. Due to these differences it is difficult to determine the source of this variation. Here I have used computer modelling to assess the impact of noise on the accuracy and precision of different BOLD-VSI calculations. The results show both potential over and underestimates of the mean vessel radius, which is confirmed with a validation study at 3T.

5.1 Introduction

MRI measurement of vessel size aims to provide a quantitative measurement of tissue microvasculature. Typically, the mean vessel size, or vessel calibre index (VCI), is calculated from the ratio of the change in R_2^* and R_2 due to the injection of a contrast agent (Dennie et al., 1998; Jensen and Chandra, 2000; Tropres et al., 2001). In the majority of studies either gadolinium DTPA (Gd-DTPA) or super-paramagnetic iron oxide (SPIO) particles are used as the contrast agent. Alternatively, the blood BOLD effect can be used as the source of this contrast (Jochimsen et al., 2010; Prinster et al., 1997; Shen et al., 2013; Shen et al., 2011). The blood oxygenation is modulated with either hypoxic, hyperoxic or hypercapnic gas challenges, probing the venous vasculature.

The use of contrast agents to determine the mean vessel size has been validated with histology in a number of animal studies (Bosomtwi et al., 2008; Dennie et al., 1998; Lemasson et al., 2013; Tropres et al., 2004a). For example, Lemasson et al. found a high correlation between VCI and stereologic measurements on histology data from rat brain tumour. While Bosomtwi et al. showed a significant correlation between MRI derived vessel size and histological measurement after stroke. Additionally, clinical studies have demonstrated the potential of VSI to provide a non-invasive assessment of tumour grade (Schmainda et al., 2004) and aid in defining the ischaemic penumbra in acute stroke (Xu et al., 2011). While the initial clinical findings are promising, the requirement to inject a contrast agent somewhat limits the potential patient population. Furthermore, because of the requirement of paramagnetic contrast agents to remain intravascular the technique is

limited to the brain, where the blood-brain barrier restricts the distribution of the contrast agent to the intravascular space (Shen et al., 2011).

To date a small number of BOLD-VSI studies have been reported in the literature. The first quantitative study (Jochimsen and Moller, 2008) used blocks of visual stimulation to modulate the BOLD signal, whereas subsequent studies (Jochimsen et al., 2010; Shen et al., 2013; Shen et al., 2011) have used gas challenges. Some difference between BOLD-VSI and Gd-DTPA studies might be expected; with Gd-DTPA providing contrast to the whole vascular system while BOLD provides a venous weighted contrast. However, there is a degree of symmetry between the arterial and venous vasculature. In-vivo measurements show that the average cerebral arteriole and venule radii are approximately the same, 26.5μm and 25.5μm respectively (Pennings et al., 2004). Therefore, we might expect the measured VSI distributions to be similar. Indeed, initial BOLD-VSI experiments (Jochimsen et al., 2010; Jochimsen and Moller, 2008) do show a high degree of similarity with Gd-DTPA measurements (Hsu et al., 2009; Kiselev et al., 2005; Xu et al., 2011). However, subsequent BOLD-VSI measurements (Shen et al., 2013; Shen et al., 2011) estimate a mean vessel radius that is less than 50% of these. The difference in vessel size estimates appears to derive primarily from a difference in the measured ΔR_2^*/ ΔR_2 ratio (denoted q). While changes in q might be expected with field strength, the signal modelling used for VCI calculations is expected to account for this. Such large differences in vessel size estimates need to be addressed before BOLD-VSI can be considered a robust and reliable technique, suitable for clinical implementation.

Because the BOLD signal provides a relatively low contrast-to-noise (CNR) measurement, BOLD-VSI is inherently more sensitive to noise than contrast based

methods. I hypothesized that it is this noise sensitivity that underlies some of the discrepancy in vessel size estimates obtained with this technique. Here I use computer modelling to assess the impact of noise on the accuracy q and VCI calculations with different BOLD-VSI analysis methods and noise content. The results of the modelling are then compared with in-vivo measurements using an oxygen challenge and different levels of spatial smoothing, producing a number of datasets with varying CNR.

5.2 Materials and Methods

5.2.1 Signal Modelling

The magnitude of MRI signals acquired with gradient echo (GE) and spin echo (SE) acquisitions are dependent on the transverse relaxation rates R_2^* and R_2 respectively. Assuming monoexponential signal decay, constant proton density and negligible T_1 effects (related to in-flow or molecular oxygen), changes in transverse relaxation rates can be determined from GE and SE acquisitions as per equations 5.1a and 5.1b.

$$\Delta R_2^* = -\frac{\ln\left(S(t)_{GE}/S_{0,GE}\right)}{TE_{GE}} \qquad [5.1a]$$

$$\Delta R_2 = -\frac{\ln\left(S(t)_{SE}/S_{0,SE}\right)}{TE_{SE}} \qquad [5.1b]$$

where S(t) is the time course of the signal magnitude, S_0 is its average value during baseline and TE is the corresponding gradient echo or spin echo time.

Because ΔR_2^* and ΔR_2 have differential vessel size sensitivity, the vessel radius, r_v, can be modelled as a function of q and the BOLD induced susceptibility change, $\Delta\chi$, so that

$r_v = f(q,\Delta\chi)$ (Jochimsen et al., 2010). Therefore, by acquiring GE and SE signals during rest and stimulation, estimates of the vessel radius can be made. In-vivo, each voxel will typically contain a distribution of vessel radii. If this distribution has a small variance compared to the mean, then the measured q (and therefore r_v) will be equal to the mean (Jochimsen and Moller, 2008). Given this, r_v represents the voxel-wise average over the post-capillary population with each vessel size weighted by its blood volume fraction.

GE and SE signals (at 3T and 7T) were estimated using a Monte-Carlo simulation of water in a vascular network. The ODIN framework (Jochimsen and von Mengershausen, 2004) was used to produce numerical integrations of the Bloch equations along a large number of random walk paths, as described in (Jochimsen and Moller, 2008). Intravascular signal was also included in the modelling, with the field distribution inside a vessel calculated according to (Bandettini and Wong, 1995). Vessel modelling was undertaken for intravascular susceptibility changes, $\Delta\chi$, ranging from of -0.05 to -0.3ppm (SI units). This range of susceptibility changes was chosen to include the measured susceptibility change with oxygen in volunteers and the reported susceptibility changes in previous studies. For a given set of parameters (resting susceptibility, susceptibility change) each vascular simulation took approximately 4-5 hours, running on a virtualised installation of NeuroDebian (hardware: 2.4 GHz Intel Core 2 Duo).

In all simulations the susceptibility difference between fully oxygenated and deoxygenated haemoglobin was taken to be 0.264 ppm (Spees et al., 2001). A diffusion coefficient of $0.76 \cdot 10^{-3}$ mm^2/s, a post-capillary blood volume fraction of 3% and a haematocrit of 0.40 were assumed. GE and SE echo times of 30/90ms at 3T and 18/55ms at 7T were chosen to be representative of recent BOLD-VSI studies. A venous oxy-

haemoglobin saturation, Y, of 60% at rest was assumed and intravascular T_2 values were calculated by fitting to (Zhao et al., 2007) at 3T and (Jochimsen et al., 2010) at 7T. In each case (3T and 7T) a quadratic fit between the reported oxygen extraction fraction and relaxation rate was made (as per equation 1.8). The quadratic fits were then used to calculate blood relaxation times for each susceptibility change, as summarised in Table 5.1.

$\Delta\chi$ (ppm)	0	-0.05	-0.1	-0.2	-0.3
Y	60%	64%	68%	75%	83%
T_2 at 3T (ms)	32.2	36.5	41.4	53.3	68.0
T_2 at 7T (ms)	8.1	9.7	12.0	18.4	27.3

Table 5.1 Modelled blood T_2 values for each of the simulated susceptibility values at 3T and 7T.

Figures 5.1a and 5.1b show plots of VCI against q for the simulated susceptibility changes at 3T and 7T respectively. It is clear from the figures that the relationship between q and r_v has a much greater dependence on $\Delta\chi$ at 3T compared to 7T (particularly for large q). This is the result of increased sensitivity to intravascular contributions at 3T, which are significantly reduced at 7T due to the short T_2 of blood.

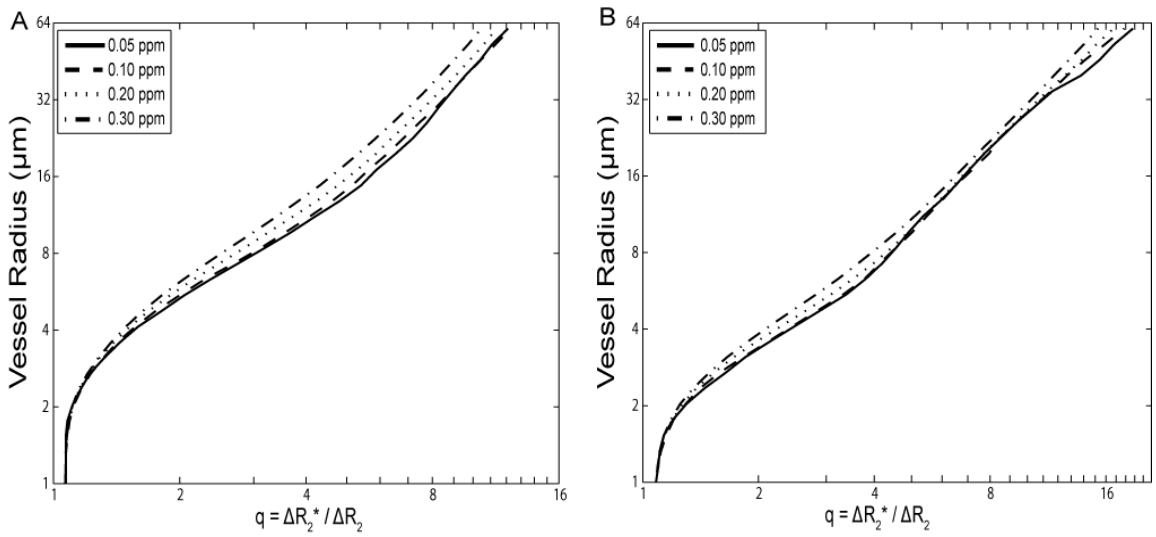

Figure 5.1 Modelled relationship between mean vessel radius (μm) and the vessel size index, q. Modelled at 3T (A) and 7T (B) for susceptibility changes -0.05 to -0.3ppm.

It should be noted that the modelling does not account for changes in blood flow or blood volume during stimulation, which are expected in hypercapnic gas challenges (Ito et al., 2003). Simulations performed by (Shen et al., 2013) suggest only a small error is introduced by ignoring ΔCBV up to 12%. Using a large hypercapnic stimulus, 7% CO_2, Ito et al. (Ito et al., 2003) measured a 30.5% increase in cerebral blood flow with an associated 9.6% change in total blood volume, well below the modelled ΔCBV. Animal experiments (Lee et al., 2001) indicate that the venous ΔCBV, which is relevant for BOLD-weighted studies, only accounts for 36% of this increase. However, the majority of this increase occurs in the small cerebral vessels, 5-15μm radius, and was found to be as large as 23% in this range of vessels with a 9% CO_2 stimulus in rat (Lee et al., 2001).

5.2.2 Noise Modelling

MRI experiments were simulated with MATLAB (Mathworks, Natick, MA) to assess the impact of noise on different analysis methods. The noise modelling used a hybrid simulation, with measured noise added to simulated MR signals. A hybrid simulation method was used to accurately capture the noise characteristics, including any correlation between the GE and SE noise that might arise due to physiological fluctuations. Noise datasets in this type of simulation are in effect resting-state EPI time series. In the simulations presented here 4 datasets were acquired in human volunteers at each field strength (3T: Siemens Verio with 32-channel head coil and 7T: Siemens Magnetom with 32-channel Nova Medical head coil). A scan time of 15 minutes was used for each acquisition (TR 3.5 seconds) using identical acquisition parameters to the simulated vessel data, TE 30/90ms at 3T and 18/55ms at 7T. In each case a GRAPPA acceleration factor of 2 and a matrix size of 64x64 was used with a 200mm FOV. A slice thickness of 3mm (1mm slice gap) and 28 slices (26 slices at 7T) were used for full brain coverage.

The measured noise datasets were pre-processed with FSL (FEAT) (http://www.fmrib.ox.ac.uk/fsl) (Smith et al., 2004). Each dataset was registered to a corresponding structural acquisition, corrected for motion, high pass filtered to remove baseline drift (cut-off = 400s) and spatially smoothed. For each acquisition, four different datasets were produced with 0, 4, 6 and 8mm FWHM spatial smoothing. After pre-processing with FEAT the datasets were masked to produce grey matter volumes, creating over 25,000 GE and SE time courses for each field strength and level of smoothing. Prior to spatial smoothing, grey matter voxels had a mean time course SNR (tSNR) of 66±29 for GE acquisitions and 35±13 for SE acquisitions at 3T. At 7T, the GE

acquisitions had a similar tSNR, with a mean value of 67±29. However, the SE tSNR value increased slightly to 45±19. Given the non-uniform distribution of tSNR values across the brain, a random sampling of voxels (from all volunteers) was used during simulations, ensuring an unbiased noise distribution for each simulated vessel size.

During modelling, the randomly selected GE and SE noise pairs were added to simulated experimental data, representing the expected BOLD signal change due to a gas challenge. The experimental paradigm consisted of two stimulation blocks of 3 minutes (TR=3.5 seconds) interleaved with three 3-minute baseline periods. When presented with a block gas challenge, the change in oxy-haemoglobin saturation is somewhat delayed and dispersed. To account for this, the block design was convolved with a gamma-variate function (mean lag 30 seconds and standard deviation 30 seconds). In our experience the resulting time course fits well with grey matter BOLD data acquired in CO_2 challenges. While the mean lag would be greater for an oxygen challenge, which is typically accounted for by longer rest periods, these differences are not expected to have a large influence on the analysis.

5.2.3 Vessel Population Modelling

When reporting in-vivo estimates of vessel size it is often useful to present a summary measure across voxels, such as a mean grey matter estimate. A population modelling approach was used to analyse the impact of noise on such an analysis. Using an assumed VCI distribution, to represent the histogram of mean VCI values across an ROI, the number of simulations was modulated for each vessel radii. Smoothing splines were fitted to the modelled MRI signals, allowing noise simulations to be performed on vessel

radii from 1 to 70 μm in 0.01μm steps, with a minimum of one simulation at each radius. To extend the range of SNR values probed by the simulations each analysis was repeated using four different levels of spatial noise smoothing (0, 4, 6 and 8 mm FHWM).

The VCI distribution was chosen to represent the expected distribution of mean vessel radii present in grey matter ROI analysis. The in-vivo distribution of the VCI over a region of interest is unknown and cannot easily be inferred from ex-vivo measurements such as confocal laser microscopy. Ex-vivo measurements of vessel size typically exclude veins and arteries, and are subject to ill-defined vessel shrinkage; while BOLD-VSI is sensitive to the entire post-capillary network including veins. As such, estimates made using VSI are expected to be significantly greater than ex-vivo measurements.

Because of the difficulty in inferring the true in-vivo distribution I have taken the practical approach in deriving a distribution from the current VSI literature; (Hsu et al., 2009; Jochimsen et al., 2010; Jochimsen and Moller, 2008; Kiselev et al., 2005; Xu et al., 2011) all present distributions with similar mean values and distributions. However, the Gd-DTPA studies are sensitive to the entire vasculature, not just the post-capillary network. Additionally, contrast agent based experiments have been shown to have a dependence on the relative arterial and venous blood volume and the tracer bolus dispersion (Xu et al., 2013). The data acquired by Jochimsen and Moller (Jochimsen and Moller, 2008) used a smaller susceptibility change and lower field strength than Jochimsen et al. (Jochimsen et al., 2010), and so are expected to suffer from a lower CNR. Because of these considerations, the volunteer data presented in (Jochimsen et al., 2010) was used as the basis for the VCI distribution. MATLAB was used to fit the averaged data with a generalized extreme value distribution, the resulting probability density

function being described by a Frechet distribution (α=0.41, β=5.8, γ=10.1 and R^2=0.99), equation 5.2.

$$f(x) = \frac{\alpha}{\beta}\left(\frac{\beta}{x-\gamma}\right)^{\alpha+1} \exp\left(-\left(\frac{\beta}{x-\gamma}\right)^{\alpha}\right) \qquad [5.2]$$

where α is the shape parameter, β is the scale parameter and γ is the location parameter. The parameters α and β are distinct from the other uses of alpha and beta in this thesis.

Figure 5.2 shows the correspondence between the derived distribution and a histogram of mean VCI values obtained from volunteer data. The volunteer data was obtained at 3T as outline in section 5.2.4 below. For consistency with methods employed in Jochimsen et al. 2010, from which the model distribution is derived, the q values in the volunteer data have been calculated with a standard linear regression between ΔR_2* and ΔR_2.

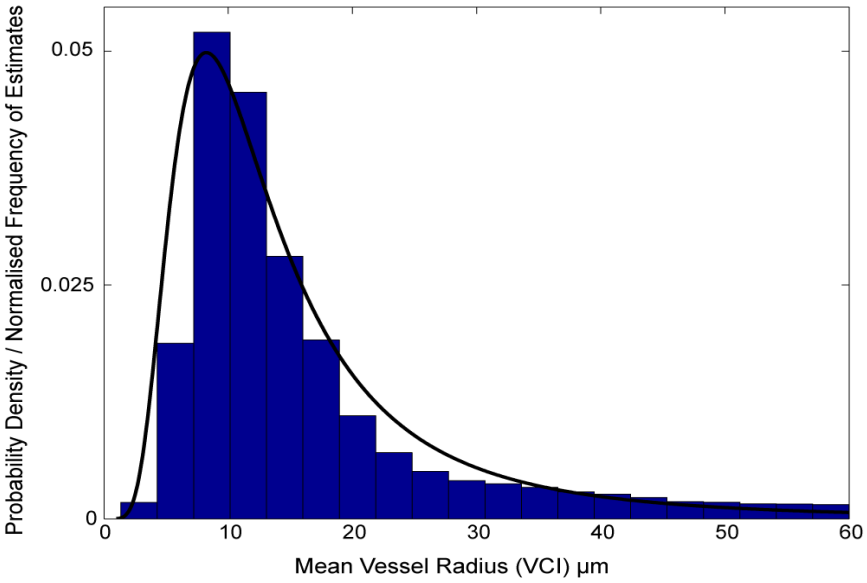

Figure 5.2 Modelled VCI distribution across grey matter voxels (solid line), plotted against a histogram of grey matter VCI estimates from volunteer data.

5.2.4 MRI Validation Study

To validate the simulation results, five VSI datasets were acquired at 3T from five healthy volunteers (4 male and 1 female, mean age 34). The experimental paradigm and data acquisition were identical to the simulations; TR=3.5 TE=30/90ms, 3x3x3mm^3 voxel, 28 slices with 1mm slice gap. The BOLD signal was modulated with two periods (3 minutes each) of elevated oxygen. During the stimulation periods 100% oxygen was delivered to the subjects via a non-rebreathing mask (Flexicare Medical, Mountain Ash, UK) at a flow rate of 15 L/min. During rest periods, air was delivered through the mask at the same flow rate. The acquired MR data was motion corrected and smoothed with 4 different Gaussian smoothing kernels (FWHM 0, 4, 6 and 8mm) to produce 4 different VSI datasets. The datasets were then analysed as described in the following sections.

To calculate the blood susceptibility change caused by the stimulus, blood T_2 was measured in the sagittal sinus at baseline and stimulation (using a further oxygen block). The T_2 measurements were performed using an implementation of T_2-Relaxation-Under-Spin-Tagging (TRUST) (Lu and Ge, 2008). In our local implementation (figure 5.3) spin tagging was performed using a pseudo-continuous inversion in the sagittal sinus superior to the imaging slice with a tag duration of 1.4 seconds and a post-labelling delay time of 150 ms. An MLEV T_2 preparation was used with 10 ms CPMG time (Lu et al., 2012), with effective TEs of 0, 40, 80 and 120 ms, with 4 tag-control pairs acquired for each preparation time. As per (Xu et al., 2012b) global spoiling was used at the end of each TR, allowing a TR of 4 seconds and a total acquisition time of 2.2 minutes.

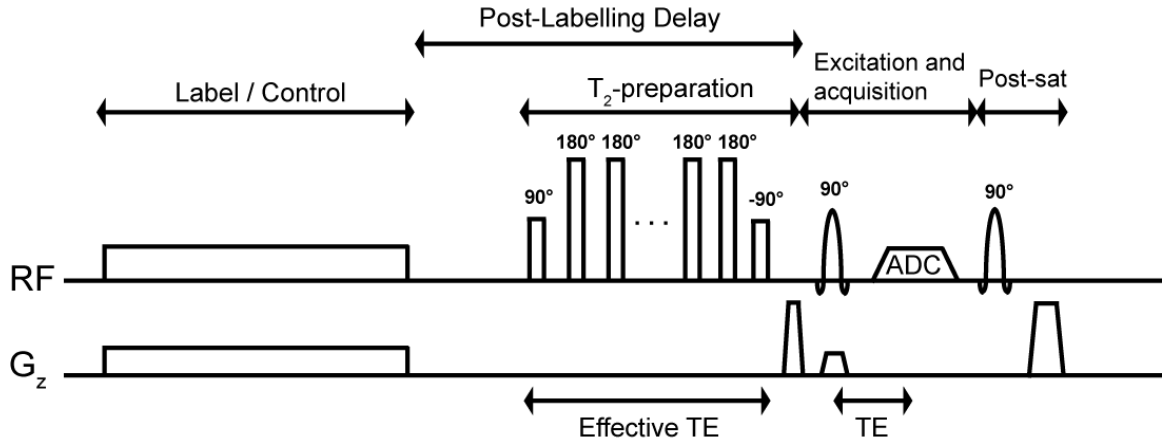

Figure 5.3 Pulse sequence timing diagram for the implemented pCASL TRUST sequence used to measure the global change in venous blood saturation.

Tag-control image pairs were motion corrected, subtracted, and the average value of a selected sagittal sinus voxel fit to obtain an estimate of T_2. The measured T_2 values were converted to venous oxygen saturation values according to (Lu et al., 2012) assuming a haematocrit of 0.4, and then into blood susceptibility values according to equation 5.3 (Weisskoff and Kiihne, 1992), where $\Delta\chi_{do} = 4\pi \cdot 0.264$.

$$\chi = Hct\Delta\chi_{do}(1 - Y_v) \qquad [5.3]$$

5.2.5 Analysis Methods

All datasets (simulations and volunteer studies) were analysed using two principal methods to calculate q, and therefore vessel size. In the first case the average decay rates (ΔR_2^* and ΔR_2) during signal plateau periods are used, in the second case a linear regression of ΔR_2^* timepoints against ΔR_2 is used as per (Jochimsen et al., 2010). Figure 5.4 shows the expected BOLD timecourse for the applied hyperoxic stimuli, along with the associated signal plateau periods.

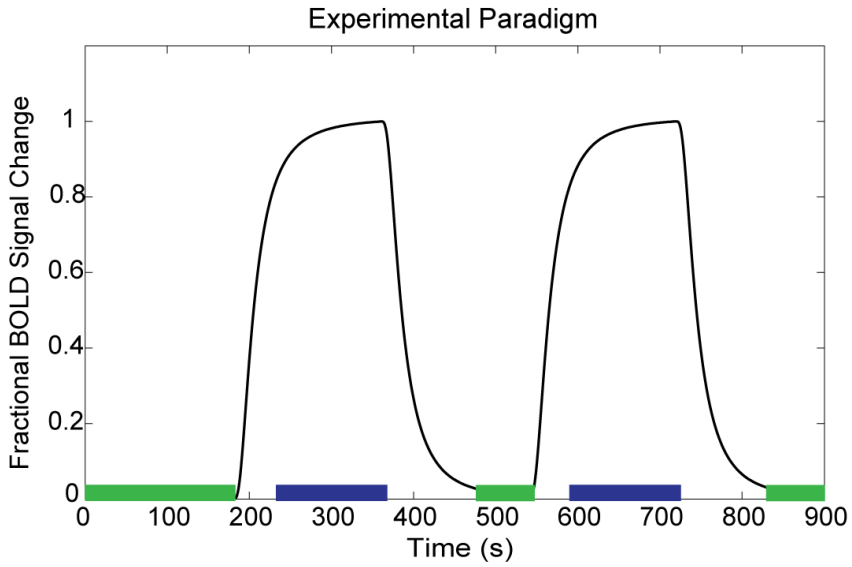

Figure 5.4 Expected BOLD timecourse for the implemented gas paradigm. Plateau periods for the normoxic and hyperoxic states are highlighted in green and blue respectively.

Examples of the acquired BOLD (GE and SE) time series from volunteer data are shown in figure 5.5. The data is extracted from a single voxel to highlight the effect of spatial smoothing on the data. The overall variation in the signal is in good agreement with the predicted BOLD timecourse. The magnitude of the signal change for the GE data is significantly greater than for the SE data (suggesting a large VCI). Increasing the spatial smoothing from 4mm to 8mm FWHM demonstrably increases the CNR of both the GE and SE data. The improvement in CNR appears to be greater for the SE dataset; revealing the expected signal variation in the 8mm FWHM dataset that is difficult to discern in the 4mm filtered data.

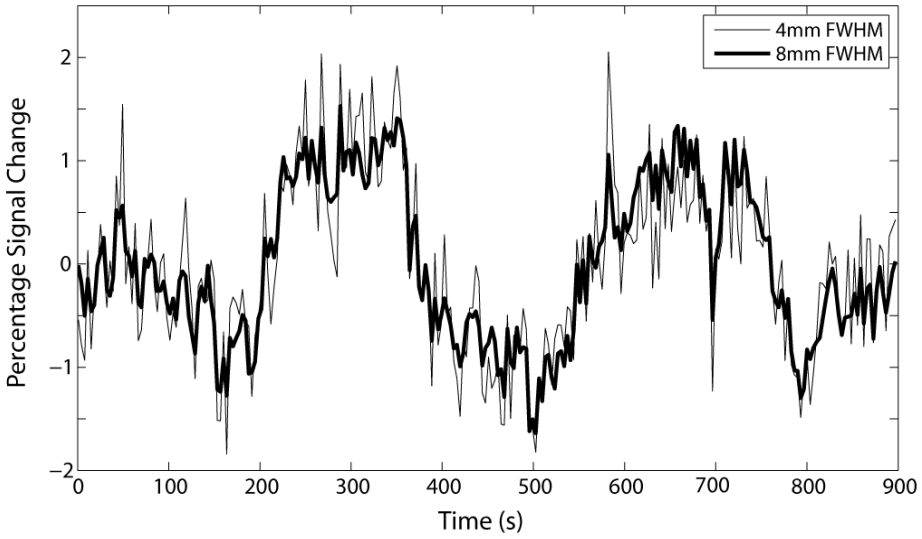

Figure 5.5a Example GE BOLD time courses from a single voxel. The same data is displayed with 4mm and 8mm FWHM Gaussian spatial smoothing.

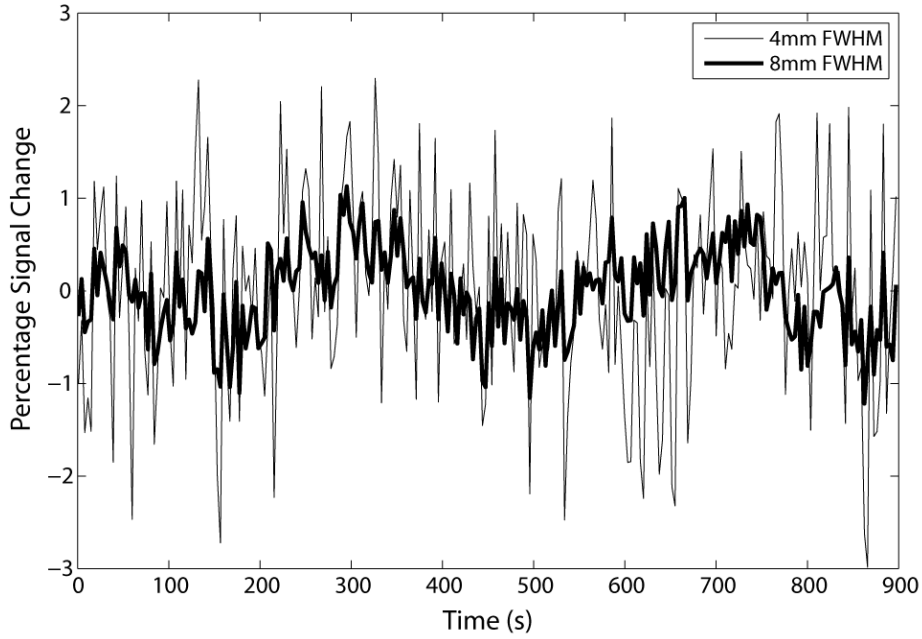

Figure 5.5b Example SE BOLD time courses from a single voxel. The same data is displayed with 4mm and 8mm FWHM Gaussian spatial smoothing.

For each of the analysis techniques a refinement of the method was also investigated. For the plateau analysis a t-test was used to identify statistically significant signal changes between baseline and stimulation periods as per (Shen et al., 2013; Shen et al., 2011). For consistency with the method proposed by Shen et al., only simulations that showed significant signal increases in both the GE and the SE data with a p-value of 0.0001 were included. The regression analysis, which was originally evaluated with ordinary least squares (OLS), was extended via the use of a total-least squares regression. Total least squares allows for observational errors on both dependent and independent variables and so allows for uncertainties in both ΔR_2^* and ΔR_2. This is untrue of simple linear regression, which assumes the independent variable to be error free, and thus leads to attenuation bias when this is not the case (Frost and Thompson, 2000).

Calculated q values were converted into distributions of vessel radii using the Monte-Carlo modelled data and the relationships described in figure 5.1. Unrealistic vessel sizes estimates, less than 1μm and greater than 70 μm, were discarded. Vessel distributions are summarised using the median, as is appropriate for non-normal distributions, however in some instances mean values are also quoted for consistency with previous publications.

5.3 Results

5.3.1 Simulations

Using the estimated VCI distribution the modelled data (without noise) predicts a median q value of 4.0 (±0.4) at 3T and 5.6 (± 0.1) at 7T, corresponding to a median VCI of 11.8 μm (mean value 13.8 μm). The data from the hybrid noise simulation predicts both an over and underestimates of the mean and median VCI. The direction of the error is

mainly dependent on the analysis type, while the size of the error is dependent on the susceptibility change and level of spatial smoothing. A summary of the effect of spatial smoothing on a ROI analysis at 3T is presented in figure 5.6 and table 5.2. The modelled data presented here is averaged over all simulated susceptibility changes to isolate the influence of spatial smoothing. For the sake of clarity the plots have only been displayed for the extreme ranges of spatial smoothing (0mm and 8mm FWHM).

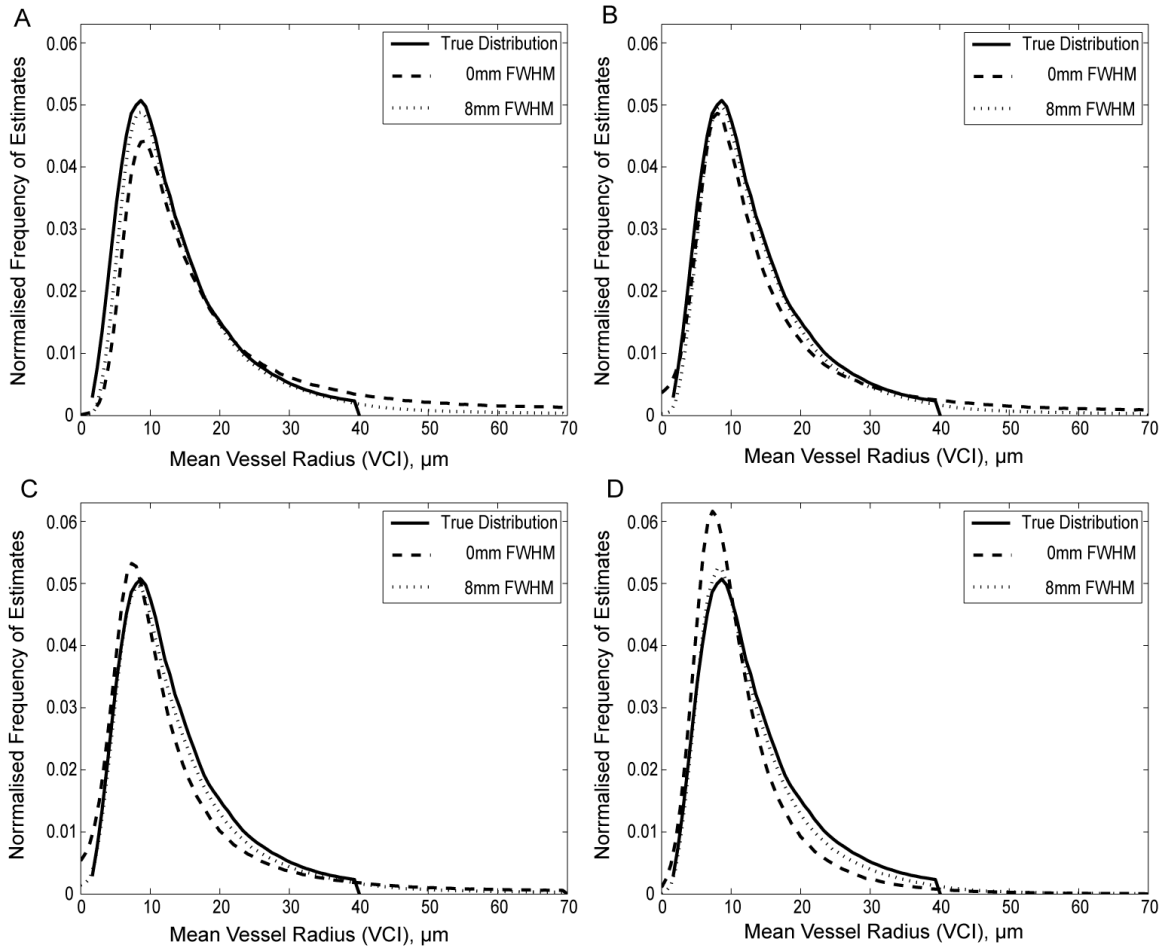

Figure 5.6 Modelled probability density estimates of mean vessel radii for each analysis method at 3T with an assumed vessel distribution (true distribution). Modelled data derived from 0mm and 8mm FWHM smoothed datasets (averaged over susceptibility changes -0.05 to -

0.3ppm). Ordinary least squares analysis (A), total least squares (B), plateau analysis (C) and plateau analysis with t-test (D).

	OLS		TLS		Plateau		Plateau with T-Test	
	Mean	Median	Mean	Median	Mean	Median	Mean	Median
No Filter	38%	21%	21%	-0.5%	0.7%	-12%	-23%	-22%
4mm	28%	15%	14%	2.3%	4.3%	-6.6%	-14%	-14%
6mm	17%	8.7%	8.7%	2.6%	4.7%	-3.3%	-5.8%	-7.5%
8mm	12%	6.4%	7.9%	2.6%	5.0%	-1.5%	-1.9%	-4.2%
Average	**24%**	**13%**	**12%**	**1.7%**	**3.7%**	**-5.8%**	**-11%**	**-12%**

Table 5.2 VCI error with degree of spatial smoothing at 3T. Group mean and median error values for mean vessel size estimates averaged over all simulated susceptibility changes at 3T. FWHM of Gaussian filter 0mm to 8mm.

The simple regression technique (OLS) produces a large overestimation of the mean VCI at 3T, reducing with increased spatial smoothing. The total least squares regression (TLS) significantly reduces this overestimation taking the group median error down from 13% to 1.7%. However, the plateau analysis results in a consistent underestimation of the median value, with a group error of -5.8%. The inclusion of a t-test increases this error to -12%.

A summary of the results at 7T is shown in table 5.3 below. The increase in the CNR at 7T has produced a significant reduction in all errors. In particular there is significant improvement in the OLS estimates, which now show only a modest over-estimation in the median (group value of 3.5%), even with no spatial smoothing. However, there is still

a surprisingly high bias introduced by the t-test method (for small $\Delta\chi$), which is apparent in the summary statistics. The cause of this anomaly is likely due to the sharper decrease in spin-echo signal with vessel size, the same reason for increased q values at 7T. Thus, the statistical test is more heavily biased to larger vessel sizes at higher field strengths

	OLS		TLS		Plateau		Plateau with T-Test	
	Mean	Median	Mean	Median	Mean	Median	Mean	Median
No Filter	15%	3.5%	8.0%	-4.4%	0.5%	-11%	-16%	-19%
4mm	13%	3.8%	7.4%	-1.9%	1.7%	-7.5%	-12%	-14%
6mm	3.7%	-0.3%	0.6%	-3.4%	0.3%	-4.9%	-6.9%	-8.4%
8mm	2.2%	-0.2%	-0.0%	-2.3%	0.2%	-3.3%	-4.6%	-5.8%
Average	**8.5%**	**1.7%**	**4.0%**	**-3.0%**	**0.7%**	**-6.7%**	**-9.8%**	**-11.8%**

Table 5.3 VCI error with degree of spatial smoothing at 7T. Group mean and median error values for vessel size estimates averaged over all simulated susceptibility changes at 7T. FWHM of Gaussian filter 0mm to 8mm.

The data presented in figure 5.6 and tables 5.2-5.3 are averaged over all the modelled susceptibility changes. As such they summarise the influence of spatial smoothing for a variety of modelled gas challenges (oxygen, carbon dioxide and carbogen). In figures 5.7 a typical values of spatial smoothing (6mm FWHM) has been used to investigate the influence of the susceptibility change, and therefore gas challenge, on the estimated mean vessel size distribution. The plots show estimated VCI distributions for $\Delta\chi$ = -0.05 and -0.3 ppm for each analysis method. It is clear from the figures that the plateau analysis

shifts the modal value to the left, increasing the number of small vessel estimates. The OLS analysis shifts the modal value to the right. Introducing a t-test preferentially removes large vessel estimates, with increasing bias for smaller susceptibility changes. The TLS analysis shows reduced bias compared to the OLS analysis, more closely matching the true distribution. Increasing $\Delta\chi$ reduces the bias present in all analysis techniques.

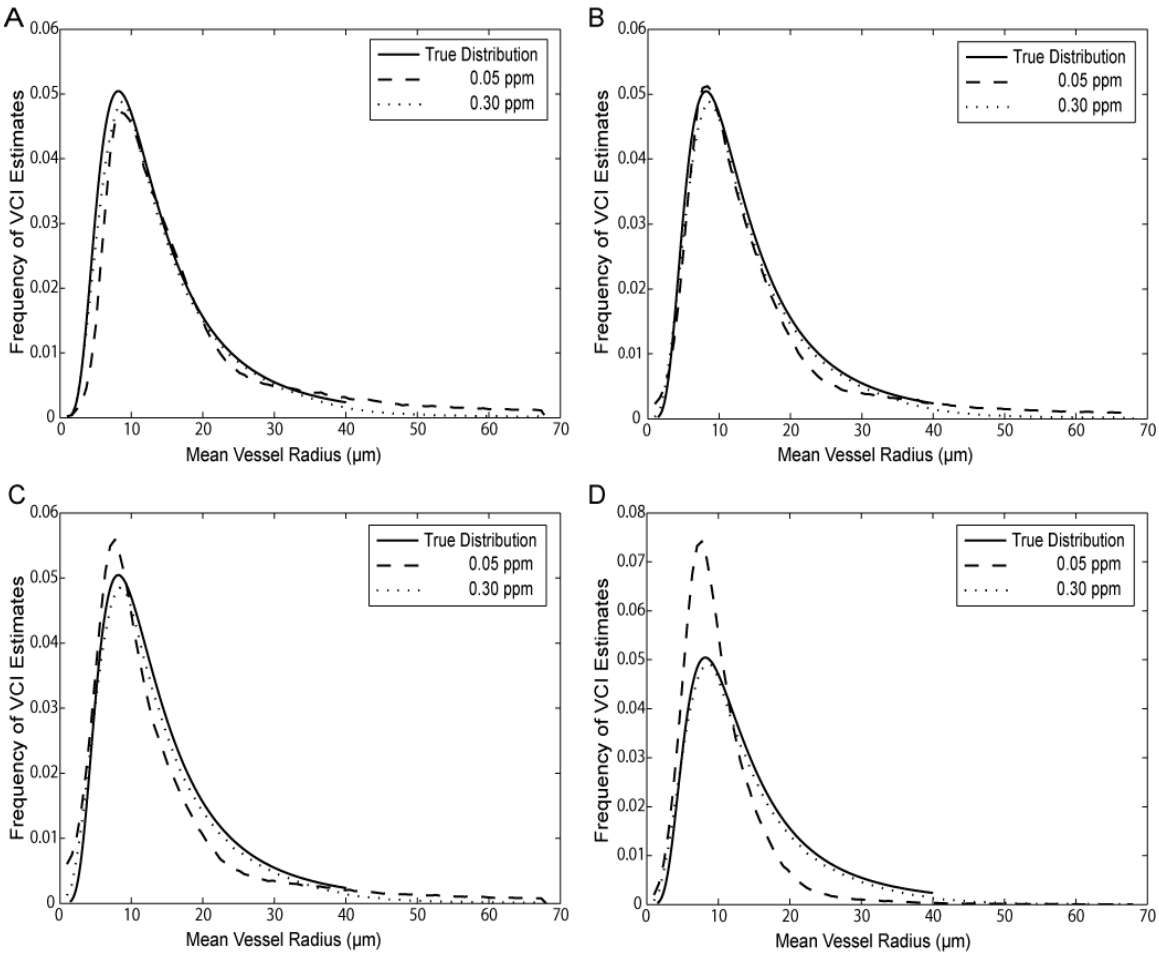

Figure 5.7 Modelled probability density estimates of vessel radii for each analysis method at 3T with an assumed vessel distribution (true distribution). Modelled data derived from 6mm FWHM smoothed datasets and susceptibility changes -0.05 and -0.3ppm. Ordinary least squares analysis (A), total least squares (B), plateau analysis (C) and plateau analysis with t-test (D).

The modelling results presented thus far have sought to summarise the influence of spatial smoothing and susceptibility change on a ROI analysis of VCI. In the following table (table 5.4) the analysis is presented for a modelled oxygen challenge ($\Delta\chi$ = -0.05ppm) at 3T. Oxygen challenges are easily implemented and tolerated by subjects and therefore are a desirable method of performing VCI analysis. However, the small associated change in susceptibility means they have a low CNR and are heavily influenced by the analysis method. The data in table 5.4 suggests that an error of up to -43% in the median VCI could be produced using the t-test analysis on such data. Increasing the level of spatial smoothing only reduce this error to around -13% for a smoothing kernel of 8mm FWHM. Analysis methods such as the total-least squares and standard plateau analysis reduce this error significantly, with a minimum error of 4.4% predicted with the TLS method and an 8mm smoothing kernel.

	OLS		TLS		Plateau		Plateau with T-Test	
	Mean	Median	Mean	Median	Mean	Median	Mean	Median
No Filter	55%	33%	14%	-9.4%	-7.9%	-26%	-46%	-43%
4mm	43%	24%	16%	-3.6%	0.8%	-16.5%	-38%	-35%
6mm	29%	15%	15%	2.0%	4.9%	-9.1%	-23%	-21%
8mm	23%	13%	14%	4.4%	6.2%	-5.3%	-13%	-13%

Table 5.4 VCI error for $\Delta\chi$ = -0.05ppm at 3T. Group mean and median error values for different levels of spatial smoothing (FWHM of Gaussian filter 4mm to 8mm) with $\Delta\chi$ = -0.05ppm at 3T.

5.3.2 In-vivo Validation

Measurements of the change in intravascular T_2 (as a result of the hyperoxic stimulus) were made with a TRUST sequence. The average T_2 value at baseline was found to be 65 ms, increasing to 75 ms during hyperoxia, which is equivalent to an intravascular susceptibility change of -0.057ppm. The closest modelled susceptibility change of -0.05ppm was used to calculate radius estimates from the volunteer data.

Figure 5.8 shows example parameter maps for each of the analysis methods (OLS, TLS, plateau and plateau plus t-test) from the acquired volunteer data. The maps appear generally similar, with an apparent reduction in vessel size with the plateau techniques.

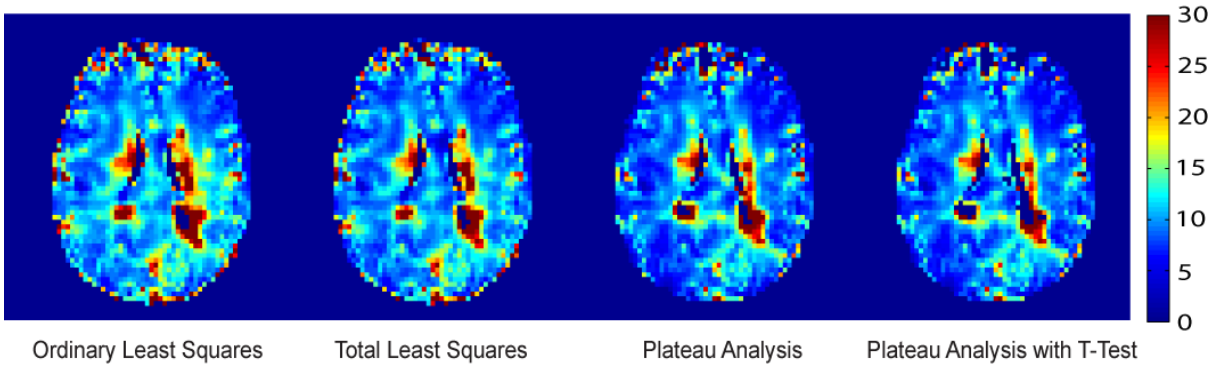

Figure 5.8 Example mean vessel calibre estimates (μm) from an individual subject. The same slice is shown analysed with each of the investigated methodologies.

The variation in vessel size with analysis method and smoothing level is summarised in Table 5.5. As with the modelled data, OLS estimates are consistently greater than TLS, while the median TLS value is relatively insensitive to the degree of spatial smoothing. Plateau estimates of VCI are less than with the regression techniques, and are further reduced by including a t-test. This is consistent with the modelled data presented in table

5.4, which predicts errors of 13%, 4.4%, -5.3% and -13% for a susceptibility change of -0.05ppm and an 8mm spatial smoothing kernel.

	OLS		TLS		Plateau		Plateau with T-Test	
	Mean	Median	Mean	Median	Mean	Median	Mean	Median
4mm	17.4±0.9	12.6±0.9	13.8±0.7	9.4±0.6	10.9±0.9	7.7±0.7	8.8±1.0	7.1±0.6
6mm	14.6±0.9	10.8±0.9	12.6±0.9	9.3±0.9	10.2±1.2	7.9±0.9	9.0±1.4	7.6±1.0
8mm	13.3±1.0	10.1±1.0	12.0±1.0	9.2±0.9	9.9±1.3	8.0±1.0	9.2±1.5	7.8±1.1

Table 5.5 Grey matter VCI values (μm) for in-vivo validation study with different levels of spatial smoothing at 3T (n=5). FWHM of Gaussian filter 4mm to 8mm.

Given the correspondence between the results and the expected errors, we can infer that the true mean and median VCI values in this subject group are approximately 11 μm and 8.5 μm respectively. These values are obtained by choosing VCI values that best correspond to the modelled error in each of the analysis methods.

5.4 Discussion

BOLD mediated VSI offers a novel method for quantifying vessel sizes and vessel size changes in-vivo. However, because of the relatively low CNR of the method, care must be taken when analysing and comparing results. Here I have explored the noise sensitivity of different analysis methods using a simulated BOLD acquisition. The results demonstrate significant CNR dependent variations in calculated q values, and therefore vessel size estimates.

The use of a linear regression to assess the ratio q provides a model free analysis method which should be unaffected by regional changes in haemodynamic latency and/or delay (Jochimsen et al., 2010). While this may prove important in certain disease states, it is also insensitive to any delayed hypercapnic response between healthy grey and white matter. However, standard regression techniques have long been known to underestimate the gradient due to noise in the independent variable (Spearman, 1904). Because the regression is used to estimate $1/(\Delta R_2^*/\Delta R_2)$, this can lead to an overestimation of q and hence vessel size. Here I included a total least squares regression to mitigate this effect. The modelling results show that the total least squares regression removes much of the overestimation in vessel size, correcting a median overestimation of 13% to only 1.7% at 3T.

Because large vessels produce a small ΔR_2, any reduction in this due to noise can lead to a significant overestimation of q. One method to remove these uncertain estimates, proposed by Shen et al. (Shen et al., 2011) is to use a t-test to accept estimates only if there is a significant increase in GE and SE signals between rest and stimulation. However, above approximately 10 μm the change in GE signal should always be significantly greater than the change in SE. Therefore, for the most part, this is really a test for significant changes in the SE signal. Because ΔSE decreases with vessel size, great care must be taken not to exclude legitimate voxels that are dominated by large vessels. Additionally, any estimates where noise adds to ΔSE such that it passes the t-test will be accepted, while estimates where noise reduces ΔSE below significance will be rejected. The simulations show that this biased rejection causes an increased underestimation of the mean and median vessel size. A mean reduction in vessel size of

approximately 30-40% is predicted in low CNR situations (small $\Delta\chi$ and minimal spatial smoothing), this corresponds well with the 40% change observed by Shen et al.

It could be argued that the distribution used in the modelling presented here is unrepresentative of the true vessel distribution, including an unrealistic number of large vessels. In the model distribution 20% of vessels have a radius greater than 20 μm, while in recent in-vivo studies (Perez-Barcena et al., 2009) suggest that only 10% of vessels fall into this range. However, this difference could be explained by BOLD sensitivity to large veins that were excluded from their study. Additionally, the validation study presented in this chapter revealed a consistently lower estimate of vessel size with the t-test approach that reduced with the level of spatial smoothing (as predicted by the modelling). While the motivation for the t-test approach is to remove unrealistic estimates of large vessels, it appears that the level of significance chosen is such that it includes a significant proportion of large vessel estimates in low CNR situations. This phenomenon becomes increasingly important when comparing acquisitions performed with different apparatus and gas challenges. For instance, if this approach is used to compare the vessel size response to hyperoxia and hypercapnia (where an SNR increase is expected due to an increase in $\Delta\chi$), then care must be taken to analyse the same vessel populations to avoid biasing the results.

If the estimated mean vessel size in this study (11μm) is compared with the reported VCI estimates in (Shen et al., 2011) we can see that a reduction of approximately 40% is required to match the estimated vessel size of 6.5 μm. As previously observed, this reduction is similar to the impact of the t-test in their study, and implies a low CNR compared to my modelling results. The low CNR is plausible as the results in my study

are derived from a 32-channel head coil rather than the 8-channel coil used by Shen et al. Comparing my result to (Jochimsen et al., 2010) requires a 22% increase in the mean vessel estimate to match their estimate of 13.4 μm; while my modelling can only account for 10% of this increase, the remainder can be explained by the vasodilatory effect of CO_2 (Ito et al., 2003).

The sensitivity to CNR in this study has been examined through the use of different degrees of spatial smoothing. The approach offers the opportunity to investigate the noise dependence of the analysis methods without the need to acquire multiple datasets. Additionally, it is relevant to practical BOLD-VSI implementations, which will typically employ some degree of Gaussian smoothing. However, there is the possibility that distribution of vessel sizes under examination will vary with the degree of spatial smoothing. For example, a large degree of spatial smoothing could enhance the contribution of surface draining veins to nearby tissue, thus increasing the median VCI. This phenomenon is more likely to present itself in the in-vivo experiments, as the simulations implicitly assume a uniform distribution. However, given the qualitative agreement between the simulations and in-vivo data this effect appears to be small in comparison to the investigated CNR dependence.

The results presented in this chapter highlight the important interaction between CNR and BOLD-VSI analysis methodology. The low CNR inherent in BOLD-VSI studies, particularly at lower field strengths, can lead to both large overestimation (OLS) and underestimation (t-test) of the mean vessel size. I have shown how the use of a more appropriate regression method (TLS) removes much of this bias. While the underestimation observed with the t-test methodology goes some way towards explaining

the differences observed in vessel size estimates made by Jochimsen et al. (Jochimsen et al., 2010; Jochimsen and Moller, 2008) and Shen et al. (Shen et al., 2013; Shen et al., 2011). Further differences between the results are expected due to the vasodilatory effect of CO_2 (Ito et al., 2003). The effect of a hypercapnia challenge on the venous vasculature is explored in more detail in chapter 6, where a bulk dilation model is compared to a functional recruitment model.

To increase the reliability and robustness of BOLD-VSI it is important to consider the influence of the CNR on the analysis method. Ideally data should be acquired and smoothed to achieve a CNR such that the analysis method minimally influences the results. If this is not possible then the effect of all processing steps should be understood and characterised to avoid significant bias. At 7T my modelling shows that all analysis methods result in a group error of 10% or less for large (-0.3ppm) susceptibility changes. At lower field strengths and with smaller susceptibility changes the choice of analysis method becomes increasingly critical and great care is required.

Chapter 6

MRI Measurement of Oxygen Extraction Fraction, Mean Vessel Size and Cerebral Blood Volume Using Serial Hyperoxia and Hypercapnia

Abstract

Functional magnetic resonance imaging measures signal increases arising from a variety of interrelated effects and physiological sources. As presented in the previous chapters there has been some success in disentangling this signal in order to quantify baseline physiological parameters, including the resting oxygen extraction fraction (OEF), cerebral blood volume (CBV) and mean vessel size. However, due to the complicated nature of the signal, each of these methods relies on certain physiological assumptions to derive a solution. In this chapter I present a framework for the simultaneous, voxelwise measurement of these three parameters. The proposed method removes the assumption of a fixed vessel size from the quantification of OEF and CBV, while simultaneously removing the need for an assumed OEF in the calculation of vessel size. The new framework is explored through simulations and validated with a pilot study in healthy volunteers. The MRI protocol uses a combined hyperoxia and hypercapnia paradigm with a modified arterial spin labelling sequence collecting multi-slice gradient-echo and spin-echo data.

6.1 Introduction

The magnitude of the BOLD signal produced via an intravascular susceptibility change is determined by several physiologically important parameters; including the resting venous blood volume (CBV), oxy-haemoglobin saturation (SvO_2) and vessel size. These parameters can each be used as biomarkers related to disease and disease progression. The venous oxy-haemoglobin saturation can be converted to an estimate of oxygen extraction fraction (OEF) and, by combination with a resting blood flow measurement, the cerebral metabolic rate of oxygen consumption ($CMRO_2$). Alterations in $CMRO_2$ have been linked with identification of ischaemic penumbra (Sobesky et al., 2005), and predicting tumour outcome (Miles and Williams, 2008). Additionally, MRI derived measurement of vessel size has shown the potential for non-invasive assessment of tumour grade (Schmainda et al., 2004), and to be a valuable tool for defining the ischaemic penumbra in acute stroke (Xu et al., 2011).

A number of recent studies (Germuska et al., 2013; Jochimsen et al., 2010; Shen et al., 2013; Shen et al., 2011) have explored the measurement of vessel size using either hypercapnic or hyperoxic gas challenges and a dual gradient-echo/spin-echo readout, thus providing a measurement of the BOLD sensitive vasculature. The modelling performed in these studies has demonstrated that the ratio of ΔR_2^* to ΔR_2 produces a monotonic relationship with the vessel size, and is insensitive to CBV and the change in susceptibility ($\Delta\chi$). The assumption has been that because the relationship is insensitive to $\Delta\chi$ it is also insensitive to the resting intravascular susceptibility χ_0. However, I hypothesise that this may not be the case, particularly when it is considered that the

susceptibility varies with χ_0/χ for hypercapnic challenges rather than $\Delta\chi$, as for hyperoxic challenges. Thus to properly quantify the vessel size with a hypercapnic gas challenge the resting intravascular susceptibility must also be known.

In parallel to the development of vessel size techniques, a number of groups (Bulte et al., 2012; Gauthier and Hoge, 2012) have proposed calibrated BOLD methods for measuring SvO_2 and thus OEF. In these measurements the calibrated gradient echo signal changes in response to both hyperoxic and hypercapnic challenges are used to estimate the venous saturation. One of the assumptions made in these methods is a uniform value of β in the BOLD signal model (Davis et al., 1998). The value of β reflects the relative importance of diffusion effects, and thus includes contributions from the diffusion rate and vessel scale under investigation. The modelling performed in this chapter demonstrates that the assumption of a fixed vessel scale can result in considerable uncertainty in OEF estimates.

Here I have investigated the advantages of calibrated BOLD measurements for the estimation of vessel size, and propose a new framework for the simultaneous measurement of vessel size, CBV and OEF. The new technique introduces methods for the estimation of $\Delta\chi$ and χ_0/χ in hyperoxic and hypercapnic challenges, which are then used for calibrated acquisitions of gradient/spin echo data. The method removes the need to assume either a fixed baseline susceptibility or vessel size, removing significant assumptions from each of the techniques being combined. In order to validate the new technique results from a pilot study are presented producing estimates of mean vessel size, CBV and OEF.

6.2 Theory

Recent methods presented by Bulte and Gauthier (Bulte et al., 2012; Gauthier and Hoge, 2012) demonstrate that by combining hypercapnic and hyperoxic calibrated fMRI experiments it is possible to estimate the resting OEF. The calculation of OEF is based upon the Davis BOLD model (Davis et al., 1998), where the calibration parameter M can be defined as shown in equation 6.1. The OEF is calculated by finding the value that brings hyperoxic and hypercapnic measurements of M into agreement.

$$M = \frac{\frac{\Delta BOLD}{BOLD_0}}{1 - \left(\frac{CBV}{CBV_0}\right)\left(\frac{\chi}{\chi_0}\right)^{\beta}} \qquad [6.1]$$

where CBV is the cerebral blood volume, χ is the venous blood susceptibility and the subscript *0* represents the baseline values.

In order to perform these calibration measurements it is common practice to assume a uniform value of the exponent β (Bulte et al., 2012; Chiarelli et al., 2007b; Gauthier and Hoge, 2012; Hoge et al., 1999a). The value of β defines the relative importance of diffusion effects for the sample under investigation and thus includes various factors such as the water diffusion rate, intravascular signal contribution and vessel scale. Here I present a technique that removes the need to assume a vessel scale, which is shown to have significant influence on OEF estimates, particularly for large oxygen extraction fractions.

Vascular modelling of the MRI signal (Jochimsen and Moller, 2008) has demonstrated that the ratio of ΔR_2^* to ΔR_2 (denoted q) produces a monotonic relationship with the

vessel size, as shown previously in figure 3.10. The use of hyperoxic and hypercapnic gas challenges to determine vessel size provides a measurement of the BOLD sensitive vasculature, which is directly integrable into a BOLD signal framework. Additionally, the practical implementation of BOLD-mediated vessel size imaging (BOLD-VSI) is the same as that used in calibrated BOLD experiments. Thus, standard calibration methodologies can be extended to acquire vessel size data with only the addition of a spin-echo to the EPI readout.

In the Davis signal model, β is a compound parameter, representing several interrelated effects; as such it is difficult to directly relate this parameter to vessel scale. Therefore a new formulation of the calibration problem is required to integrate vessel size information. However, rather than create a new analytical model, we propose the use of a look-up table technique to interrogate the results of a Monte-Carlo signal model directly. This approach has the advantage of offering easy access to any modelled parameter and readily lends itself to a consolidated approach, where vessel size and OEF can be calculated simultaneously. As with previous signal modelling methods e.g. (Boxerman et al., 1995; Fisel et al., 1991), the fundamental parameter driving the signal contrast in our simulations is the blood susceptibility. Reframing the problem in this way means an alternative calibration approach is needed for both hyperoxic and hypercapnic challenges. However, as can be seen from equation 6.1, the quantities χ and M are not unrelated and it is relatively straightforward to repose the calibration experiment in terms of the blood susceptibility change induced by hyperoxic (equation 6.2) and hypercapnic (equation 6.3) challenges (for derivations see appendix 6A).

$$\Delta\chi = -2.3 \times 10^{-4} \cdot \Delta P_{ET}O_2 \qquad [6.2]$$

$$\frac{\chi_0}{\chi} = \frac{CBF}{CBF_0} \qquad [6.3]$$

where CBF is the rate of cerebral blood flow and $\Delta P_{ET}O_2$ is change in end-tidal partial pressure of oxygen in mmHg.

It should be noted that while the hypercapnic calibration equation presented here relies on the same physiological assumptions used in the original derivation (Davis et al., 1998), the hyperoxic calibration method is subtly different to that presented by (Chiarelli et al., 2007b). The original hyperoxia calibration method is based on the Davis calibration model and so makes the implicit assumption that arterial blood is fully saturated. However, the method presented here assumes that there is minimal change in arterial saturation from normoxia to hyperoxia. This is a slightly more relaxed constraint and unlikely to be violated unless the normoxic arterial saturation is very low.

Formulating the calibration problem in this way means that four look-up tables, two for hypercapnic (GE and SE) and two for hyperoxic (GE and SE) stimuli, can be created; relating BOLD signal changes to alterations in blood susceptibility. Given that the induced blood susceptibility changes can be measured independently from the BOLD data, this effectively eliminates an unknown parameter from each of the models. By assuming a typical diffusion value for brain tissue, as is common in BOLD-VSI techniques (Jochimsen et al., 2010; Shen et al., 2013), the number of unknown model parameters can be further reduced to just three; the vessel scale, OEF and CBV. The results from our modelling studies show that the four measurements of BOLD signal change (hypercapnic and hyperoxic GE and SE) are sufficient to uniquely determine these parameters. Although not implemented in this pilot study, incorporation of a

diffusion measurement into estimates of these parameters would be a relatively simple matter, requiring only sufficient modelling to cover the parameter space.

In addition to modification of the calibration equations, I have extended previous modelling methods to calculate the resting vessel size using both the hyperoxic and hypercapnic methods. Data presented by (Shen et al., 2013) demonstrated an apparent larger vessel size, due to a greater mean q value, when acquired with a hypercapnic stimulus. However, for integration into this new method it is necessary that both hyperoxic and hypercapnic methods report the same resting vessel size. The modelling presented here suggests that this discrepancy in reported vessel size can be accounted for by a hyperemia induced increase in venous blood volume, as described by the functional recruitment model proposed by Kuschinsky and Paulson (Kuschinsky and Paulson, 1992). Bulk dilation of the venous vasculature, as is commonly assumed in a number of BOLD models e.g. (Buxton et al., 1998), is found to overestimate the vessel scale with a hypercapnic stimulus.

6.3 Methods

6.3.1 Monte-Carlo Signal Modelling

The basis of the signal modelling presented here is as described in (Jochimsen and Moller, 2008) and the method is unchanged for a hyperoxic stimulus. However, in order to calibrate a hypercapnic stimulus against flow change it is necessary to model the susceptibility change as χ_0/χ, rather than $\Delta\chi$ (see equations 6.2 and 6.3). Additionally, the hypercapnic flow change is thought to produce an increase in venous blood volume (Grubb Jr et al., 1974), which has been included in the modelling.

6.3.2 Hyperoxic BOLD Signal Modelling

The change in relaxation rates (ΔR_2* and ΔR_2) were simulated for $\Delta\chi$ from -0.02 to -0.10ppm, covering a range of baseline susceptibility values (χ_0) from 0.1 to 1.3ppm. Diffusion was assumed to be 0.76 μm^2/ms, as is typical in gray matter measurements (Jensen and Chandra, 2000). A post-capillary resting blood volume fraction of 3% was used, being an average of the values used in VSI simulations by Jochimsen (Jochimsen et al., 2010) and Shen ((Jochimsen et al., 2010; Shen et al., 2013). As in previous modelling studies, the blood volume was assumed to remain constant between rest and stimulation. GE and SE echo times were chosen to be 30 and 80ms, with a field strength of 3 T. For each combination of $\Delta\chi$ and χ_0 the vessel size was varied from 1 to 60 μm (with 20 different vessel sizes distributed exponentially). The vasculature was modelled as fully permeable, randomly-oriented, cylinders of infinite length. Each cylinder was modelled independently, while random vessel orientations were accounted for by varying the angle between the main field and the cylinder in the range from 0 to $\pi/2$ (in 64 linear steps). Because the field is invariant along the cylinder, simulations were only performed in a 2D plane perpendicular to the cylinder's axis. The area of the simulated plane (A) was adjusted to match the required intravascular volume fraction, where $A=\pi\cdot(\text{radius})^2/\text{CBV}$. The precession frequency in the extravascular space at rest and during stimulation was calculated according to equation 1.7, while the intravascular signal was assumed to be fully suppressed.

For each radius and vessel orientation 100,000 random walks were simulated from randomly seeded starting points. The step size of each simulation was 1 ms, with the displacement at each step generated by a Gaussian random distribution to represent

isotropic diffusion. The ODIN framework (Jochimsen and von Mengershausen, 2004) was used to produce numerical integrations of the Bloch equations at each step. The transverse magnetisation at each time point was calculated by summation over all the simulated vessel orientations. For a given set of parameters (resting susceptibility, susceptibility change, blood flow change and blood volume change) each vascular simulation took approximately 4-5 hours, running on a virtualised installation of NeuroDebian (hardware: 2.4 GHz Intel Core 2 Duo).

The results of the modelling were entered into a lookup table, with intermediate values created with spline interpolation (MATLAB, The MathWorks Inc, Natick, USA). To limit the size of the lookup table and the required modelling, the resting blood volume was taken to be linearly related to ΔR_2 and ΔR_2*, as demonstrated by Boxerman et al. (Boxerman et al., 1995) for small blood volume fractions.

6.3.3 Hypercapnic BOLD Signal Modelling

The mechanics of the hypercapnic modelling were identical to the hyperoxic modelling. However, certain modifications were made to account for the physiological differences in response to the stimuli. The change in susceptibility was modelled with χ_0/χ ranging from 1.0 to 2.0 and a hypercapnic blood volume increase was included according to the power relationship described by Grubb (Grubb Jr et al., 1974), with α=0.38.

Two physiological models were investigated to account for the venous blood volume change, one a bulk vasodilation, the second a functional recruitment model. In the *bulk vasodilation model* it was assumed that all of the blood volume increase could be explained by a passive vasodilation in the capillaries and venules, thus creating a

quadratic relationship between volume increase and radius during stimulation. In the *functional recruitment model* it is assumed that an improvement of flow in poorly perfused capillaries gives rise to an increase in the effective capillary surface area. This recruitment model does not rely on the switching of capillaries from fully closed to open, but rather the homogenisation of flow through the capillary bed, with poorly perfused capillaries that are intermittently stagnant becoming better perfused. In our modelling, this situation was represented by a stimulus induced CBV change with a constant vessel radius.

Functional recruitment involves a shift in the ratio between local perfusion pressure and capillary vascular resistance. Upstream changes in arteriolar resistance via vasodilation and vasoconstriction alter the local perfusion pressure in downstream capillaries. If the resistance in these capillaries is higher than the perfusion pressure then the red blood cells can cease to flow (stagnation), if the local pressure rises the cells can overcome the local resistance and flow again. This tends to happen intermittently in some cerebral capillaries, causing flow patterns resembling a metropolitan train service where although in general things are moving, there are significant stationary periods. An upstream increase in perfusion pressure causes the flow to change to the express service, increasing both CBF and the capillary CBV that is actively exchanging with the tissue.

6.3.4 Imaging

This study was approved by the National Research Ethics Service, Oxfordshire REC A. Informed consent was obtained from six healthy volunteers (5 male, mean age 34±4 years). Subjects were scanned at 3.0T, Siemens Verio (Siemens Medical Solutions,

Erlangen, Germany) using the body transmit coil and a 32-channel receive-only head coil. Imaging data were acquired with a pseudo-continuous arterial spin labelling (pCASL) sequence with three echo-planar (EPI) readouts; two gradient-echo readouts at 10 and 30ms, and one spin-echo readout at 80ms (see figure 6.1). Spin tagging was achieved with a 1200ms tagging duration and a 960ms post-labelling delay. After the first readout, bi-polar spoiler gradients with a first gradient moment of M1≈200 s/m were used to suppress intravascular signal, as per (Jochimsen and Moller, 2008). Images were acquired with a GRAPPA factor of 3 and a 3x3x6 mm^3 spatial resolution, using a 64x64 matrix over 12 slices with a temporal resolution of 3.5 s.

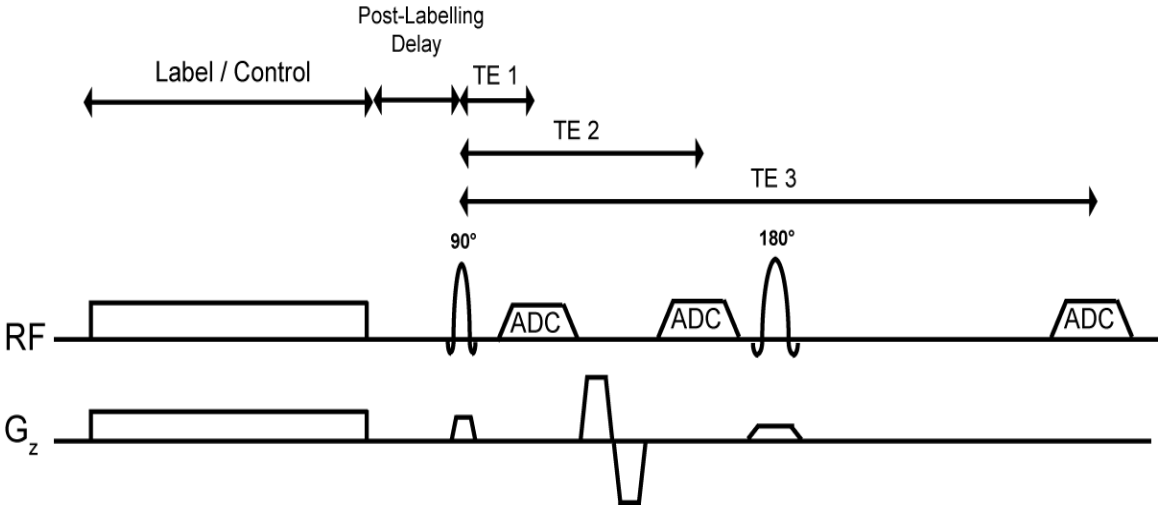

Figure 6.1 Pulse sequence timing diagram for the modified pCASL acquisition scheme with three EPI readouts (two gradient-echo and one spin-echo). A bipolar gradient (M1=200s/m) is used to spoil the intravascular signal before the second EPI readout.

A high resolution structural MPRAGE scan was acquired to enable grey matter masks to be generated (TR/TE = 2040/4.7 ms, flip = 8º, 1 mm isotropic resolution). The location of the labelling plane for the pCASL sequence was by determined by performing a time-of-

flight scan at the base of the brain. The labelling plane was prescribed approximately halfway between the upper and lower contortions of the vertebral arteries, so that the plane was perpendicular to both the vertebral and carotid arteries.

The hyperoxic condition was achieved by presenting 100% oxygen to the subject via a two tube nasal cannula at 8L/min, while the hypercapnic condition was achieved by presenting 10% carbon dioxide in air at the same flow rate. During rest periods air was delivered through the cannula at the same flow rate to avoid any change in sensation for the subject, and to ensure a swift transition between the stimulus and rest conditions. Due to mixing with room air, the inspired oxygen and carbon dioxide fractions were approximately 50% and 3% respectively. Two 2-minute periods of hyperoxia and hypercapnia were interleaved with 2-minute periods of room air, to create a total gas paradigm of 18 minutes. End-tidal PO_2 ($P_{ET}O_2$) and PCO_2 ($P_{ET}CO_2$) were recorded throughout the experiment using a Biopac MP150 (Biopac Systems, Inc. Goleta, CA, USA) with oxygen and carbon dioxide gas analyser modules (O2100C and CO2100C), at a sampling rate of 25 Hz.

6.3.5 Analysis

Images were pre-processed using FSL software tools for motion correction (Jenkinson et al., 2002) and brain extraction (Smith, 2002). High-pass temporal filtering with a cut-off of 260 s and spatial smoothing with a Gaussian kernel with a full width half maximum of 8 mm was applied to the data. The change in CBF was estimated from the first gradient-echo readout by fitting a general linear model of the expected time course using FEAT (Woolrich et al., 2001). The BOLD time courses were modeled by convolving the

hypercapnia and hyperoxia blocks with a gamma-variate function with a mean lag of 30 seconds and a standard deviation of 30 seconds. The ASL signal was explicitly modelled with alternating 1s and 0s to account for the tag/control signal change, as per (Bulte et al., 2012). The ratio of the parameter estimate (PE) of the baseline pCASL tag/control time course and the PE of the interaction between the pCASL tag/control and the BOLD time courses corresponds to the fractional change in CBF.

BOLD-weighted images were produced for the second (GE) and third (SE) EPI readouts by averaging adjacent pCASL tag and control images. The resultant timecourses were then converted to change in transverse relaxation rates (ΔR_2^* and ΔR_2) via equations 6.4a and 6.4b.

$$\Delta R_2^* = -\frac{\ln\left(S(t)_{GE} / S_{0,GE}\right)}{TE_{GE}} \qquad [6.4a]$$

$$\Delta R_2 = -\frac{\ln\left(S(t)_{SE} / S_{0,SE}\right)}{TE_{SE}} \qquad [6.4b]$$

where S(t) is the time course of the signal magnitude, S_0 is its average value during baseline and TE is the corresponding gradient echo or spin echo time.

Parametric maps were calculated in MATLAB with a Delayed Rejection and Adaptive Metropolis (DRAM) Markov chain Monte Carlo (MCMC) algorithm (Haario et al., 2006). A forward model was used to calculate ΔR_2^* and ΔR_2 timecourses for each set of parameters. A lookup table was used to find the expected decay rates, which were then multiplied by derived hypercapnic and hyperoxic BOLD time courses. The BOLD time courses were extracted from the global average of the second GE readout. The signal changes during hypercapnic and hyperoxic stimulation periods were extracted and

normalised to their maximum value. The sum of squared difference between the modelled time courses and the acquired data was returned to the MCMC algorithm for fitting.

The MCMC algorithm was run 5000 times with an adaption interval of 500 simulations for each voxel. To impose normality on the modelled parameters, CBV and VCI were fitted to their natural logarithms. The means of their prior distributions were ln(0.03) and ln(10) for CBV and VCI respectively; with their standard deviations defined by ln(2.3) and ln(1.5). The fractional change in CBF was taken to be a fitting parameter with a tight constraint on the prior distribution (standard deviations = 0.03), with the mean value for each voxel derived from the FEAT analysis. The prior distribution for χ_0 was assigned a mean value of 0.43 with a standard deviation of 0.15. Estimates of χ_0 were converted to OEF via equation 6.5.

$$\chi = 4\pi \cdot Hct \cdot \Delta\chi_{do}\left(1 - SvO_2\right) \qquad [6.5]$$

where $\Delta\chi_{do}$ is the difference in susceptibility between entirely oxygenated and entirely deoxygenated red blood cells (0.264 ppm (Spees et al., 2001)), the haematocrit was assumed to be 0.4, and OEF = 1-SvO_2.

Functional data were registered to the subject's own structural image (Jenkinson et al., 2002), with the parameter maps being simultaneously co-registered. Automated segmentation of the structural image was performed using FAST to produce grey matter, white matter and CSF regions of interest (ROI) (Zhang et al., 2001). Grey matter ROIs were then applied to the transformed parameter maps to calculate means and standard deviations.

6.4 Results

6.4.1 Modelling Results

The results of the hyperoxic modelling were found to be similar to those presented by Jochimsen (Jochimsen and Moller, 2008) and Shen (Shen et al., 2013), with $\Delta\chi$ having a minimal influence on the relationship between q and vessel size. However, the effect of the resting blood susceptibility, χ_0, was found to be quite pronounced, as can be seen in figure 6.2A. In the hypercapnic modelling significant differences were found between the bulk vasodilation model and the functional recruitment model. In all simulations the bulk dilation model predicts a lower q value than the hyperoxic model (figure 6.2B). In the functional recruitment model the value of q was found to be larger for small to medium vessel scales (2 – 20 µm), but smaller for larger vessel scales (> 20 µm), see figure 6.2C.

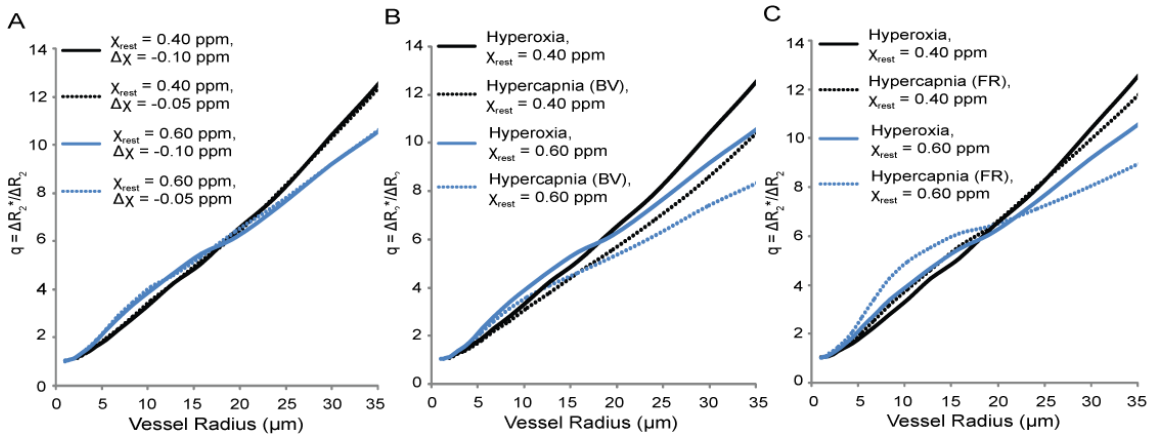

Figure 6.2 Dependence of q ($\Delta R_2^*/\Delta R_2$) on the mean vessel radius for hyperoxic and hypercapnic gas challenges. A: relationship between vessel radius and q for a hyperoxic challenge with different resting blood susceptibility values (0.40 ppm and 0.60 ppm) and different susceptibility changes (-0.05 and -0.10 ppm). B and C: Comparison between hyperoxic ($\Delta\chi$ = -

0.10 ppm) and hypercapnic stimuli (χ_{rest}/χ_{stim} = 1.3). B: Bulk vasodilation model. C: Functional recruitment model.

The majority of hyperoxic BOLD-VSI measurements have reported a mean vessel size less than 20 µm (Germuska et al., 2013; Shen et al., 2011). Thus, assuming the functional recruitment model; hypercapnic measurement of q should generally produces larger q values compared to a hyperoxic measurement. This prediction of larger q values is significant as it is consistent with in-vivo measurements (Shen et al., 2013). This difference in q values between hypercapnic and hyperoxic measurements has previously been explained by the vasodilatory effect of carbon dioxide on the venous vasculature. However, as shown by the bulk vasodilation model, such an explanation would in fact lead to a reduction in q. This counter intuitive result, with larger vessels reporting a lower q value, can be explained if we examine the modelled GE and SE signals (figure 6.3).

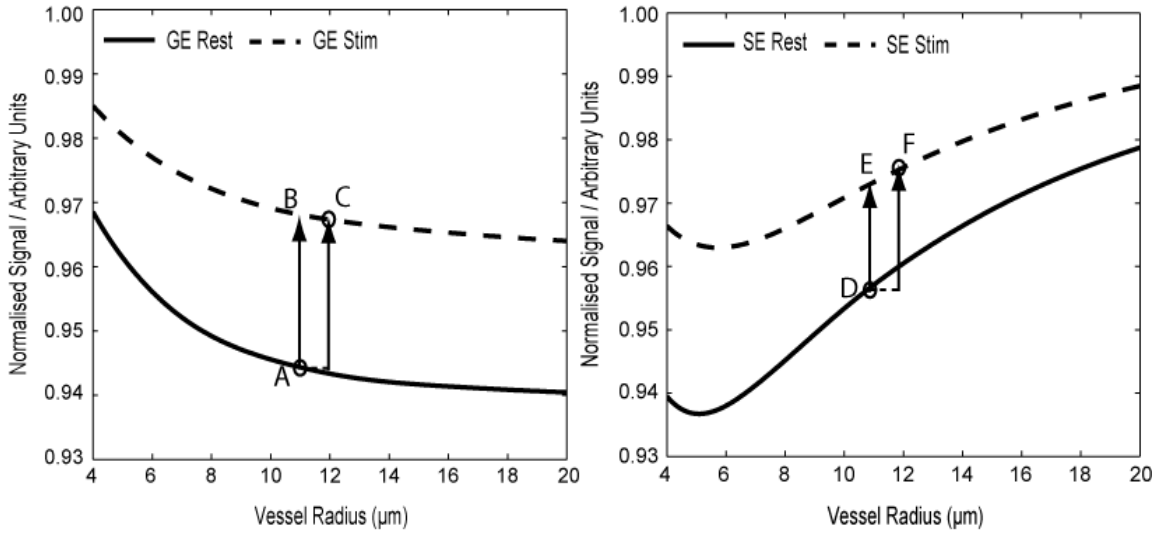

Figure 6.3. Modelled GE and SE signals for a hypercapnic challenge using the bulk vasodilation model. χ_0 = 0.45 ppm, χ_0/χ = 1.6, CBV_0 = 3%, CBV_{stim} = 3.6%. Points A and D represent the baseline signal amplitudes, points B and E are the stimulated signal amplitudes with no change in

vessel radius, points C and F are the stimulated signal amplitudes with a 10% increase in vessel radius.

For illustrative purposes the data in figure 6.3 contains a significant flow change, resulting in a 20% increase in CBV between rest and stimulation. In the bulk dilation model this is equivalent to an approximate 10% increase in vessel radius. Therefore, choosing 11 μm to represent a typical vessel size measurement (Germuska et al., 2013), we should expect a mean vessel radius of approximately 12 μm at stimulation. First, ignoring any increase in vessel size, we can see that the signal increase for the GE signal (A to B) is substantially greater than that for the SE signal (D to E). However, if the 10% vessel size increase is included, the change in the SE signal is increased (D to F), while the change in GE signal (A to C) is slightly reduced. Because q is calculated as the ratio of ΔR_2^* to ΔR_2, this increase in the SE signal will lead to a reduction in q. It can be seen from figure 6.2b that this is true for all resting vessel radii above approximately 5 μm. These modelling results suggest that the functional recruitment model, rather than the bulk dilation model, is a more suitable description of the vascular response to a hypercapnic stimulus, as it provides an explanation for the larger q values observed with a hypercapnic challenge.

The data in figure 6.2 suggests that the relationship between the vessel size and q is strongly dependent on the resting OEF, but only weakly dependent on the change in susceptibility. To investigate this relationship further, vessel size calculations were made with the MCMC fitting algorithm. Fits to noiseless modelled data were made minimising the error either in q (as in a standard VSI technique), or against the relaxation rates ΔR_2^* and ΔR_2. A range of vessel sizes was modelled (2-40 μm in 0.1 μm steps) with each

simulation using random values of OEF (0.1 to 0.95), χ_0/χ (1.15 to 1.45) and $\Delta\chi$ (-0.02 to -0.1 ppm). The range of values was chosen to cover the entire parameter space of OEF simulations and typical hypercapnic and hyperoxic stimuli. When estimating the vessel radius from the change in relaxation rates, the hyperoxic and hypercapnic susceptibility changes were assumed to be known, simulating a calibrated experiment. The results of the analysis are shown with scatter diagrams in figure 6.4, with the modelled vessel size plotted against the estimated vessel size. The top row (A1 to A3) is calculated using the ratio q, while the bottom row (B1 to B3) represents the calibrated methodology. The first column displays results from a hyperoxic stimulus, the middle column from a hypercapnic stimulus and the final column from a combined experiment with serial hyperoxic and hypercapnic stimuli.

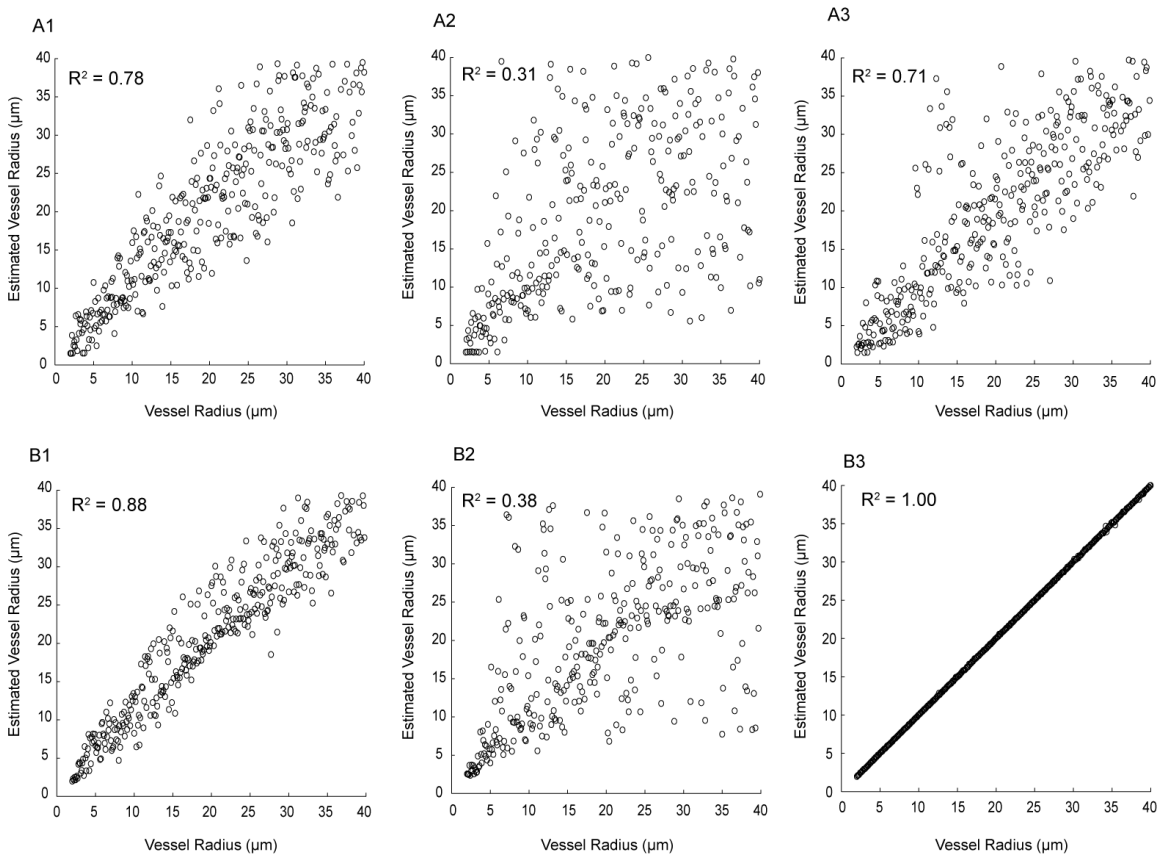

Figure 6.4. Accuracy of vessel size estimates with variability in OEF, $\Delta\chi$ and χ_0/χ. Modelled vessel radius vs. estimated vessel radius (μm) for randomly selected model parameters OEF (0.1 to 0.95), $\Delta\chi$ (-0.02 to -0.1 ppm) and χ_0/χ (1.15 to 1.45). Panels A1 to A3 were calculated using the ratio q, while panels B1 to B3 were calculated using a calibrated measurement of the relaxation rates. The left column represents a hyperoxic challenge, the centre a hypercapnic and the right column and serial hyperoxic/hypercapnic experiment.

The accuracy of vessel size estimates for the hyperoxic stimulus is significantly better than with the hypercapnic stimulus. Calibrating the simulations introduces moderate improvement for the individual hyperoxic and hypercapnic challenges, increasing the R^2 value in both instances. This moderate increase corresponds to removal of uncertainty in the stimulus produced susceptibility change, which is known to have a small effect on

vessel size estimates (Jochimsen and Moller, 2008). However, by combining the calibrated hyperoxic and hypercapnic data an apparently perfect correspondence, R^2 = 1.00, is achieved between the modelled data and the vessel size estimates (Figure 6.4 B3).

The significant improvement in vessel size estimates demonstrated by the combined calibrated approach is a result of its ability to simultaneously estimate the OEF, CBV and vessel size; thus reducing the problem to one unique solution. This is demonstrated by example in figure 6.5

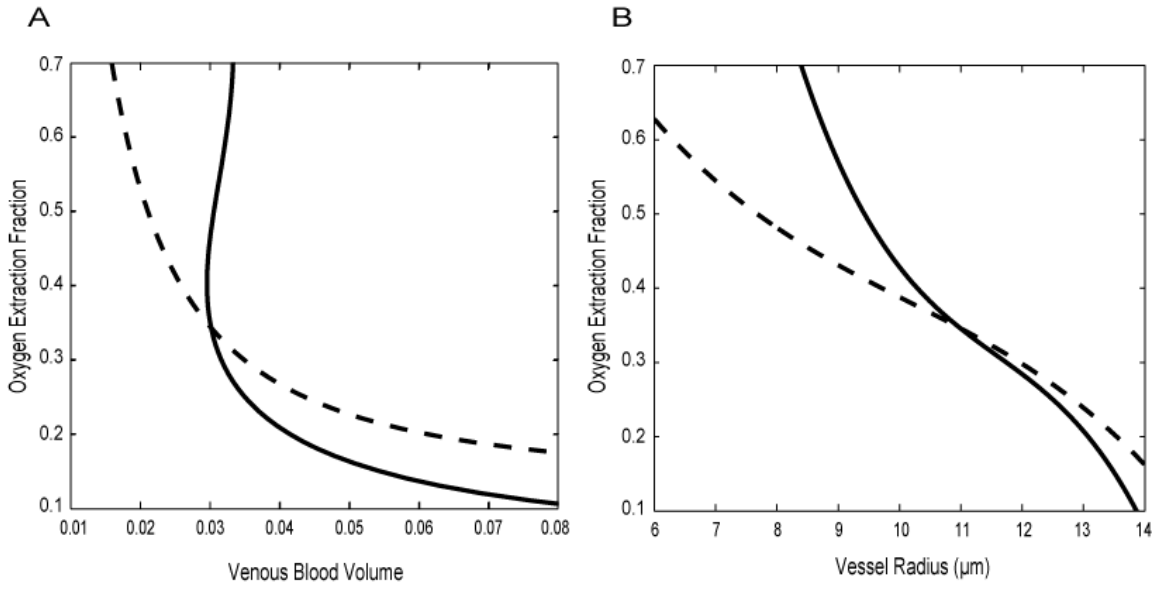

Figure 6.5. Modelled hyperoxic (solid) and hypercapnic (dashed) calibrated data for typical physiological parameters (vessel radius 11 μm, CBV 3% and OEF 0.35). Panel A: CBV vs. OEF. Panel B: Vessel Radius (μm) vs. OEF. The displayed curves represent the possible set of solutions defined by each experiment. In each case the two intersection points coincide with the modelled values.

The curves in figure 6.5 represent the possible solutions for calibrated hyperoxic and hypercapnic stimuli for a typical set of physiological parameters (vessel size of 11 μm, a

CBV of 0.03 and an OEF of 0.35). For each stimulus a range of solutions exists that matches the modelled changes in relaxation rates. However, the intersection of the curves uniquely identifies the modelled vessel size, OEF and CBV. Thus, the accuracy of estimates in figure 6.4 B3 also applies to OEF and CBV estimates, which are simultaneously solved for in the fitting procedure.

The assumption of a uniform β value in techniques that use the Davis model is equivalent to the assumption of uniform diffusion effects. In the modelling presented here the intravascular signal is assumed to be fully suppressed and the extravascular diffusion is assigned a typical grey matter value. Therefore, assuming a fixed β value is equivalent to assuming a typical vessel size. By making this assumption, and considering only the gradient-echo signal, a comparison can be made with previous calibrated OEF measurements.

Figure 6.6 demonstrates the accuracy in estimating OEF from the gradient echo signal when the true vessel size differs from the estimate (11 μm). The data is modelled for a resting CBV of 0.03 and typical gas stimuli of χ_0/χ = 1.3 and $\Delta\chi$ = -0.05 ppm. The sensitivity to error in the true vessel size is dependent on the resting OEF. For smaller OEF values (less than approximately 0.35), typical of those found in healthy brain tissue, there is very little influence of vessel size on the accuracy of the results. However, as the resting OEF is increased there is a dramatic fall in accuracy. For small vessel sizes the OEF estimates quickly reach a plateau as they hit the limits of the model, while for large vessel sizes the effect is less dramatic; resulting in both under and over estimates of OEF. The small error in GE estimates for low OEF (healthy) values is in agreement with the sensitivity analysis in (Bulte et al., 2012). However, the increase in error with resting

OEF is indicative of non-linearities in the BOLD response, present in the Monte-Carlo modelling.

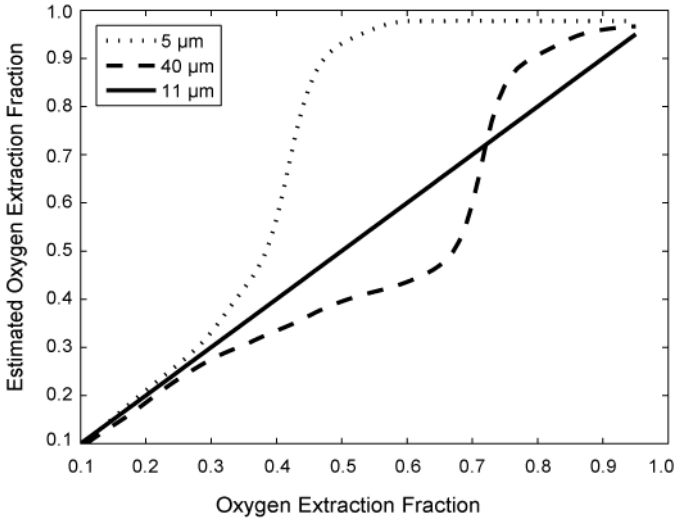

Figure 6.6. Resting OEF vs. estimated OEF using gradient echo only data and an assumed vessel size of 11 μm. Data plotted for a true vessel size of 11 μm (solid), 5 μm (dotted) and 40 μm (dashed).

6.4.2 Imaging Study

One subject was excluded from the analysis due to a $\Delta P_{ET}O_2$ less than 150 mmHg. The cause of this is likely to be an obstruction of the nasal cannula during the gas paradigm, providing an insufficient gas challenge to the volunteer. For the remaining 5 volunteers the mean $\Delta P_{ET}O_2$ was 270 ± 39 mmHg. This is significantly less than the 424 mmHg change observed in (Gauthier and Hoge, 2012) due to a 100% oxygen stimulus. However, this is to be expected due to mixing of the delivered oxygen with room air when delivered via a nasal cannula. The mean increase in CBF caused by hypercapnia was 16 ± 4.4%, while hyperoxia did not produce a significant flow decrease. The average reduction in flow during hyperoxia was 0.4 ± 7.4% (after correcting for T1 changes (Hare et al.,

2013)), assuming a T_1 of blood during hyperoxia of 1.55 s (Bulte et al., 2007b). Because the hyperoxic flow decrease could not be measured on a voxelwise basis it was not included in the analysis.

Figure 6.7 shows the results (CBV, OEF and mean vessel radius) from a single slice for the 5 subjects. The fractional CBV maps are displayed on a log scale to enhance the grey/white matter contrast. Mean grey matter values for all subjects are shown in table 6.1. The average grey matter estimates agree well with previous PET and MR literature (Ito et al., 2004; Jain et al., 2010; Jochimsen et al., 2010; Van Zijl et al., 1998): with a mean OEF value of 0.36 (±0.05), post-capillary CBV estimate of 0.035 (±0.01), and a mean vessel radius estimate of 13.5 μm (±1.7). The CBV maps show the expected grey/white matter contrast and maps of vessel size are a generally uniform as previously observed in healthy tissue (Kiselev et al., 2005).

Subject	$\Delta P_{ET}O_2$ /mmHg	CBV	OEF	VCI / μm
1	273	0.030	0.43	13.7
2	243	0.035	0.35	14.6
3	334	0.024	0.34	14.2
4	266	0.045	0.40	14.3
5	236	0.039	0.29	10.6
Mean ± s.d.	270± 39	0.035± 0.01	0.36± 0.05	13.5± 1.7

Table 6.1. Grey matter values for all subjects and group means ± standard deviations.

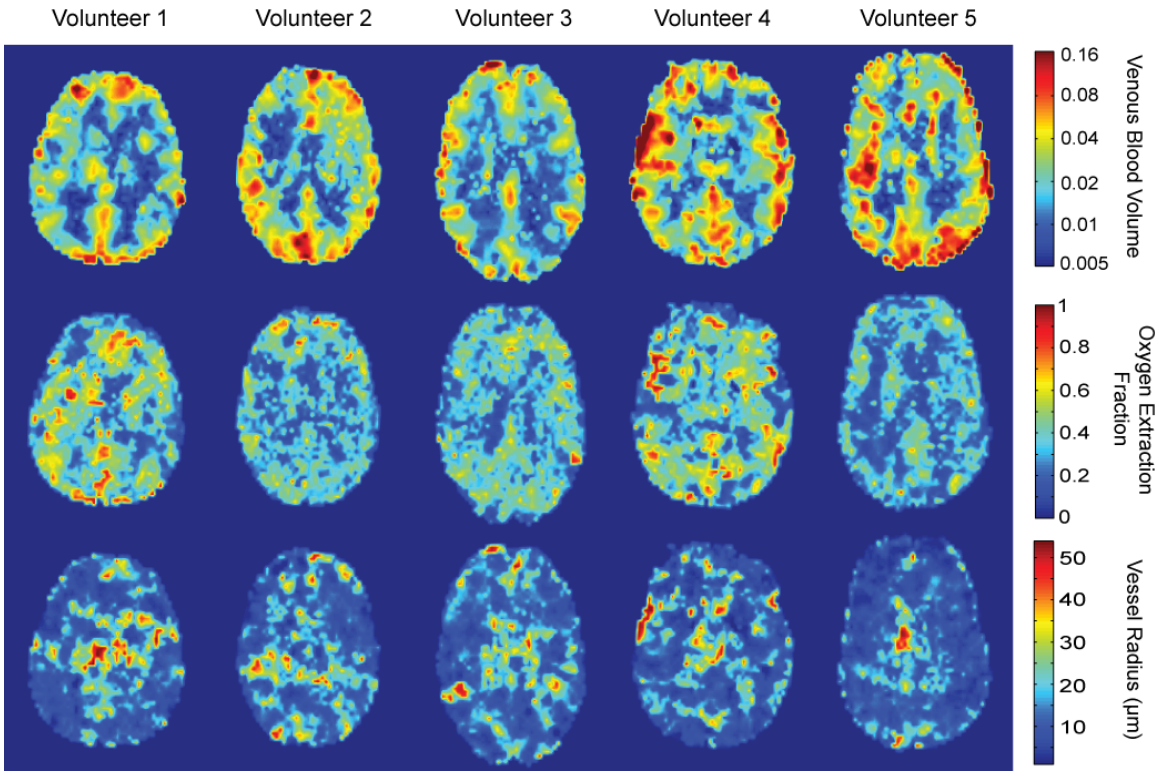

Figure 6.7. Example parameter maps from each of the volunteer in the pilot study. The top row shows CBV estimates from a single slice, with corresponding OEF and VCI estimates displayed in the middle and bottom rows respectively.

While the average OEF values are within the expected range, the maps show a number of large estimates (particularly in volunteers 1 and 4). These hotspots can be explained by considering the sensitivity analysis shown in figure 6.8. The sensitivity plots are derived by assessing the percentage error in estimating the mean parameter values found in this study (CBV = 0.035, OEF =0.36 Vessel Radius = 13.5 μm) for a deviation ± 20% in CBF/CBF_0 and $\Delta P_{ET}O_2$. The analysis demonstrates that large overestimates in OEF can be caused by an underestimation of hypercapnic CBF/CBF_0. Given the relatively small hypercapnic flow change measured in this pilot study, it is likely that the data presented here is particularly prone to these errors. Thus it is likely that the high estimates of OEF

are erroneous, with the underlying values closer to a flat distribution as reported in the PET literature.

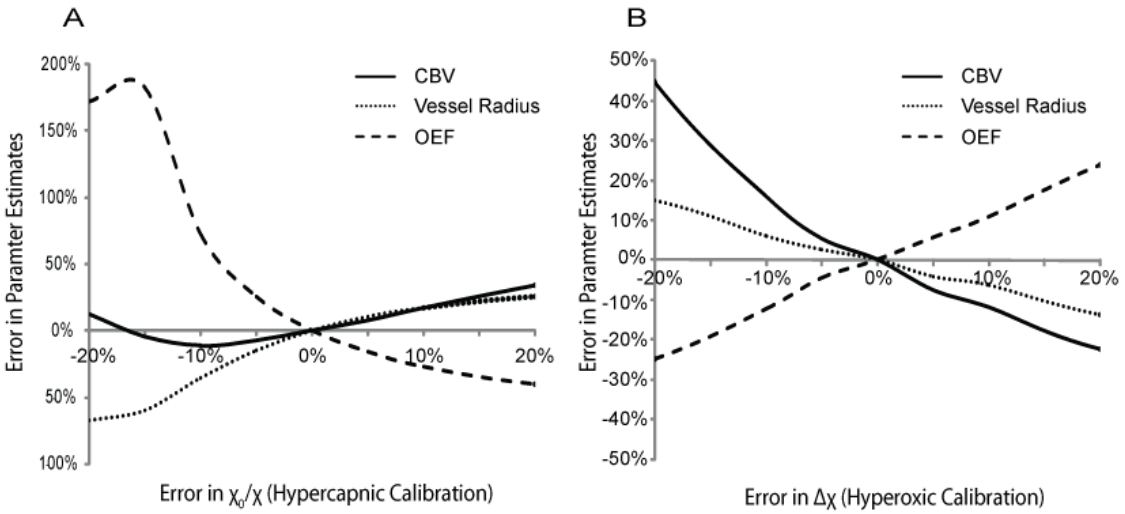

Figure 6.8. Sensitivity of parameter estimates to errors in hypercapnic calibration (A) and hyperoxic calibration (B). The percentage error for each parameter is calculated for typical physiological values (CBV = 0.035, OEF = 0.36 Vessel Radius = 13.5 μm) for a deviation ± 20% in the true CBF/CBF_0 and $\Delta P_{ET}O_2$ from the measured value.

The sensitivity analysis is also informative with regards to the assumption that the arterial blood is fully saturated in the derivation of the hypercapnia calibration method. From consideration of equations A11 to A13 we can see that when this assumption is not true the measured flow change will be an overestimate of the fractional susceptibility change (χ_0/χ). Additionally, the conversion of χ_0 to OEF via the equation of $1\text{-}SvO_2$ to OEF will no longer be valid. Fortunately the combination of these errors appears to act in opposition to each other, producing only a small error in the calculated OEF. If we assume a typical resting SvO_2 of 0.65 and a measured CBF/CBF_0 of 1.3 then the

overestimation of χ_0/χ and its impact on the calculations can be assessed for different arterial saturations. A typical saturation value of 0.97 would lead to an approximate 3% overestimation in χ_0/χ and thus, from figure 6.8A, a 7% reduction in the estimate of χ_0. At the extreme end of the range, an arterial saturation of 0.85 would result in a 13% overestimation of χ_0/χ and thus cause χ_0 to be underestimated by approximately 30%. However, because the conversion from χ_0 to OEF also assumes full arterial saturation the resulting OEF estimates will only be in error by -1.3% and 4.1% respectively. It should be noted however, that estimates of CBV and vessel size will be of a similar magnitude to the errors in χ_0.

The sensitivity of the proposed methodology to errors in $\Delta P_{ET}O_2$ is less pronounced for OEF and vessel size. However, it is the driving factor for errors in CBV. This result is consistent with the idea that the hyperoxic signal change is predominantly a CBV weighted signal (Blockley et al., 2013), where calibration against $\Delta P_{ET}O_2$ can be used to estimate CBV. Consideration of figure 6.5 demonstrates that, for OEF greater than approximately 0.25, the calibrated hyperoxic signal does indeed correspond closely to the CBV. However, the advantage of the proposed method for estimating CBV (from a combined hyperoxic and hypercapnic experiment) is that it does not restrict the range of applicable OEF values or require an implicit assumption of vessel size (via fixing of the parameter β).

6.5 Discussion

In this chapter I have demonstrated a combined approach for the estimation of vessel size, resting OEF and CBV in five healthy subjects. The parameter maps show values within

expected normal ranges, and are comparable to values determined by both PET and other MRI methods. The CBV maps depict the grey/white matter distributions expected, while maps of OEF and vessel size are more uniform. Compared to individual parameter estimation methods (Blockley et al., 2013; Bulte et al., 2012; Jochimsen et al., 2010), the combined estimation approach has the advantage of requiring fewer physiological assumptions. For example, in the estimation of vessel size it has previously been necessary to assume a resting OEF. The modelling results presented in figure 6.4 demonstrate that such an assumption can lead to large uncertainty in vessel size estimates, particularly when using a hypercapnic stimulus. By combining the calculation of vessel size with an estimate of OEF this uncertainty in the modelled data is removed. The advantage of the combined analysis approach also extends to the estimation of the resting OEF. The data presented in figure 6.6 demonstrates that such estimates can be highly dependent on vessel size, particularly for large OEF values. Thus, the inclusion of a simultaneous estimate of vessel size expands the range of OEF values that can be probed.

The calculation of resting OEF is shown to be predominantly susceptible to errors in the measurement hypercapnic flow change (figure 6.8). This sensitivity to flow change for calibrated measurement of OEF is in agreement with (Gauthier and Hoge, 2012), who found this to be the limiting factor in the stability of the approach. The agreement between our results and those presented by Gauthier and Hoge is to be expected as both methods rely on the same fundamental calibration methods. Other factors that affect the accuracy of the presented method are the assumption of fully saturated arterial blood and minimal influence of any flow reduction during hyperoxia. These assumptions are taken from the hypercapnic and hyperoxic calibration methodologies incorporated into our

method and as such have not been directly addressed here. However, the influence of any hyperoxic flow change has been minimised by the gas delivery method. Delivering 100% oxygen via a nasal cannula produces an FiO_2 of approximately 50%, thus minimising any flow changes associated with the stimulus. While previous studies have made a uniform correction for flow during hyperoxia, this approach was not taken here due to the minimal flow change detected in the study (-0.4%). The assumption of fully saturated arterial blood is demonstrated to cause potential errors in the calculation of CBV, vessel size and χ_0. However, the sensitivity analysis reveals that the presented OEF estimates are unlikely to be in error by more than 1-2% due to this assumption. While for greater saturation changes the propagation of errors also appears to be favourable, producing an error of less than 5% for an arterial saturation of 0.85. Despite the low sensitivity of OEF to errors in arterial saturation it is anticipated that the accuracy of results, in particular CBV and vessel radius, could be improved by the inclusion of an externally measured arterial saturation in the fitting process. Adding this information would allow the CBF/CBF_0 ratio to be appropriately scaled to χ_0/χ, while simultaneous fitting for the baseline parameters. However, because the current modelling does not include any arterial contribution, any change in arterial saturation during a hyperoxic stimulus cannot be fully accounted for by the model.

An important aspect of the proposed methodology is the ability to calculate the resting vessel size with both hyperoxic and hypercapnic challenges. In order to do this I have modified previous hypercapnic modelling to reflect the dependence on baseline susceptibility (i.e. χ_0/χ) and have included a blood volume change via the functional recruitment model. The functional recruitment model suggests that an increase in CBF

leads to rapid redistribution of capillary flows to a more homogenous pattern, which has been shown to increase oxygen extraction efficacy (Jespersen and Østergaard, 2012). This increase in efficacy gives a physiological impression of an "apparent" increase in the capillary surface area (Kuschinsky and Paulson, 1992). While this model rules out any physical increases in venous CBV during hypercapnia, which is in agreement with some more recent hypercapnic PET studies (Ito et al., 2005), it does involve an increase in the functional post-arterial blood volume that is actively exchanging with the tissue. Importantly such an increase in the active blood volume does not require an increase in vessel size, and thus allows us to explain the larger q value observed with hypercapnia (as described in the methods section).

The extensions made to the hypercapnic-VSI modelling also reveals that vessel size measurements made with hypercapnia are highly sensitive to the resting OEF (figure 6.4). While this is advantageous for the proposed technique, helping to identify a unique solution for OEF, it suggests that measurement of vessel size cannot be made with a simple hypercapnic stimulus if there is uncertainty in the resting OEF. Fortunately there is much less uncertainty in vessel size measurements made with a hyperoxic stimulus, and calibration against $\Delta P_{ET}O_2$ is shown to reduce this further. Although not implemented here, by restricting the range of possible OEF values, it is apparent that such a calibrated measurement could also be used to produce a simultaneous estimate of CBV (see figure 6.5). This method of CBV determination is similar to that proposed by (Blockley et al., 2013), where gradient-echo data was shown to produce CBV estimates for OEF values in the range of 0.35 to 0.55 when calibrated against $\Delta P_{ET}O_2$. However,

because only the GE signal is acquired in the Blockley method, an assumed vessel size is implicitly used (via assuming a fixed contribution of diffusion effects with a β value of 1).

The presented work represents an evolution of quantitative fMRI methods, bringing in additional measurements to help constrain the unknown aspects of the physiology and thus potentially provide better estimates of the parameters of interest. However, there are still certain physiological limitations that need to be explored to understand the clinical scope of the method. For example, the method is shown to be sensitive to errors in the measurement of hypercapnic CBF changes, which may prove difficult to measure in certain disease states. Additionally, the vascular modelling assumes that all intravascular blood is suppressed with the bipolar crushers. The crushing scheme employed here has previously been shown to suppress the majority of the intravascular signal (Jochimsen and Moller, 2005), and so it is a reasonable assumption. However, it is expected that there will be a certain level of residual signal, the impact of which will require more comprehensive modelling to explore. The framework of the presented technique is based on the differential susceptibility dependence of hypercapnic and hyperoxic stimuli rather than any particular model of the BOLD signal. Therefore, extending the underlying BOLD model to include intravascular effects should not alter the applicability of the method. In fact, any BOLD signal model that describes the GE and SE responses to a change in susceptibility could be used.

In the pilot study a nasal cannula was used to deliver the gas stimuli to subjects. This decision was primarily made to increase the subject comfort level. However, the concentration of delivered gas is inherently limited by mixing with room air when using this delivery system. This did not pose a problem for oxygen delivery, providing a robust

BOLD response, while limiting any hyperoxic CBF effects. However, the hypercapnic stimulus only produced a mean CBF increase of 16%. This is significantly lower than typically achieved with a mask delivery system, and is the likely cause for the non-physiological OEF values reported in some of the subjects. It is anticipated that a significant improvement in the reported data could be achieved by optimising the hypercapnic delivery and CBF measurement.

In summary, we have presented a framework for combined gradient and spin echo measurement of fundamental cerebral physiological parameters using MRI with a combined hyperoxia and hypercapnia stimulus. This method is an extension of previously developed gradient echo methods, incorporating a spin echo BOLD measurement to reduce the necessary physiological assumptions. Modelling studies demonstrate that the new technique is applicable to a wider range of physiological states, and thus has the potential to become a valuable tool in the assessment of disease. Experimental application of this new method produced results that are consistent with the available literature and with the effects predicted by the simulations.

Appendix 6.A

Hyperoxic Gas Modelling

A direct mechanism for modulating the oxy-haemoglobin saturation is to increase the arterial oxygen content via a hyperoxic gas challenge. The effect of a such a challenge on the blood susceptibility can be examined via the Fick principle, equation A1; relating the rate of cerebral oxygen metabolism ($CMRO_2$), cerebral blood flow (CBF) and oxygen extraction (arterial to venous difference).

$$CMRO_2 = CBF \cdot \left(CaO_2 - CvO_2\right) \qquad [A1]$$

where $CMRO_2$ and CBF are expressed in ml/100g/min, and CaO_2 and CvO_2 are the arterial and venous oxygen content, as described by equations A2 and A3.

$$CaO_2 = \phi[Hb]SaO_2 + \varepsilon PaO_2 \qquad [A2]$$

$$CvO_2 = \phi[Hb]SvO_2 + \varepsilon PvO_2 \qquad [A3]$$

The constants ϕ, ε and $[Hb]$ are the oxygen carrying capacity of haemoglobin (ϕ =1.34 $mlO_2\ g_{Hb}^{-1}$), the solubility coefficient of oxygen in blood (ε = 0.0031 $mlO_2\ dl_{blood}^{-1}\ mmHg^{-1}$) and the blood haemoglobin concentration. SaO_2 and SvO_2 are the fractional arterial and venous oxy-haemoglobin saturations. PaO_2 and PvO_2 are the O_2 tensions in units of mmHg.

If it is assumed, as is common for calibrated BOLD studies (Hoge et al., 1999a), that $CMRO_2$ and CBF are minimally affected by an increase in arterial oxygen content, then it follows that the a-v change in oxygen content during normoxia (rest) is the same as the change in oxygen content during hyperoxia (stim) (equation A4).

$$\left(CaO_2 - CvO_2\right)_{rest} = \left(CaO_2 - CvO_2\right)_{stim} \qquad [A4]$$

The contribution from $\varepsilon \cdot PvO_2$ to the venous oxygen content is very small, thus equations A2 and A3 can be substituted into equation A4 to give the relationship shown below.

$$\Delta SvO_2 = \frac{\phi[Hb]\Delta SaO_2 + \varepsilon \cdot \Delta PaO_2}{\phi[Hb]} \qquad [A5]$$

Because a hyperoxic challenge will minimally influence the arterial saturation, SaO_2, equation A5 can be further simplified to give a direct relationship between ΔSvO_2 and ΔPaO_2.

$$\Delta SvO_2 = \frac{\varepsilon \cdot \Delta PaO_2}{\phi[Hb]} \qquad [A6]$$

Considering that the blood susceptibility is directly linked to the venous saturation via equation A7, it follows that the change in blood susceptibility can be estimated from ΔPaO_2 as shown in equation A8.

$$\chi = 4\pi \cdot Hct \cdot \Delta\chi_{do}\left(1 - SvO_2\right) \qquad [A7]$$

$$\Delta\chi = \frac{-4\pi \cdot Hct \cdot \Delta\chi_{do}}{\phi[Hb]} \varepsilon \cdot \Delta PaO_2 \qquad [A8]$$

where $\Delta\chi_{do}$ is the difference in susceptibility between entirely oxygenated and entirely deoxygenated red blood cells (0.264 ppm). The percentage haematocrit can be approximated as three times the blood haemoglobin concentration (see equation 1.2 of this thesis). Assuming that the alveolar-arterial oxygen gradient is not altered by mild hyperoxia and ΔPaO_2 is equivalent to $\Delta P_{ET}O_2$, equation A8 reduces to a simple scaling of $\Delta P_{ET}O_2$.

$$\Delta\chi = -2.3 \times 10^{-4} \cdot \Delta P_{ET}O_2 \qquad [A9]$$

Therefore the change in blood susceptibility in a hyperoxic challenge is additive and independent of the baseline blood susceptibility. In fact it relies entirely on the size of the change in PaO_2, which can be estimated from the change in end-tidal oxygen content.

Hypercapnic Gas Modelling

For a hypercapnic challenge we again start from the Fick principle and equation A1; however it is now assumed that $CMRO_2$ stays constant while CBF increases. This means that the fractional change in CBF must be equal to the inverse of the fractional change in arterial to venous oxygen content difference:

$$\frac{CBF_{stim}}{CBF_{rest}} = \frac{\left(CaO_2 - CvO_2\right)_{rest}}{\left(CaO_2 - CvO_2\right)_{stim}} \qquad [A10]$$

Given that the dissolved oxygen content at normoxia is small in comparison to the bound oxygen content, and PaO_2 will not change with a hypercapnic stimulus, we can approximate equation A10 with equation A11.

$$\frac{CBF_{stim}}{CBF_{rest}} = \frac{\left(SaO_2 - SvO_2\right)_{rest}}{\left(SaO_2 - SvO_2\right)_{stim}} \qquad [A11]$$

As per (Davis et al., 1998) it is now assumed that SaO_2 is close to saturation, thus equation A11 simplifies to

$$\frac{CBF_{stim}}{CBF_{rest}} \approx \frac{1 - SvO_{2rest}}{1 - SvO_{2stim}} \qquad [A12]$$

As before we can now substitute for the susceptibility inside a blood vessel (equation A7) to realise that the fractional change in blood flow is inversely proportional to the fractional change in blood susceptibility:

$$\frac{\chi_{rest}}{\chi_{stim}} \approx \frac{CBF_{stim}}{CBF_{rest}} \qquad [A13]$$

Therefore, the change in blood susceptibility caused by a hypercapnic stimulus is multiplicative rather than additive. The magnitude of the change depends not only on the local CBF but also on the baseline susceptibility.

Chapter 7

Vessel Size Imaging in the Brainstem

7.1 Introduction

The brainstem is vital for the control of critical body functions such as respiration, regulation of blood-pressure and digestion. Diseases of the brainstem have a very poor prognosis. For example diffuse intrinsic potine glioma (DIPG) constitutes only 10-15% of all paediatric brain tumours; however, they are the main cause of death in this group. While other debilitating diseases that affect the adult population, such as Parkinson's and Alzheimer's diseases, are characterized by early pre-clinical involvement of the brainstem (Hawkes et al., 2010; Simic et al., 2009). Despite the importance of the brainstem in such diseases, there has been limited use of quantitative MRI techniques in their assessment; primarily due to the limitations of imaging, segmentation and analysis in this region (Lambert et al., 2013).

In this work data acquisition schemes are compared for MRI evaluation of vessel size data in the brainstem. Histological measurement of vessel size has shown a strong correlation to treatment response in pre-clinical cancer studies (Farrar et al., 2010; Lemasson et al., 2013; Walker-Samuel et al., 2012). While a change in vessel density has been linked with Parkinson's diesease (Bradaric et al., 2012) and Alzheimer's disease (Biron et al., 2011). The imaging in this study is acquired using a completely non-

invasive methodology using the BOLD response to a hyperoxic stimulus to measure the mean vessel size within a voxel (Germuska et al., 2013).

A number of studies have demonstrated the use of an evoked BOLD response to measure the vessel size in the human brain (Germuska et al., 2013; Jochimsen et al., 2010; Shen et al., 2013). However, as with standard fMRI studies, acquisition of data in the brainstem is hindered by cardiac-induced movement. Strong motion artefacts can occur in the brainstem due to natural elongation and contraction during the cardiac cycle and its close proximity to the basilar artery (Beissner et al., 2011). Methods to counteract these motion induced artefacts include retrospective filtering (Glover et al., 2000), and cardiac gating (Zhang et al., 2006). One of the disadvantages of cardiac gating is the fluctuations in repitition time (TR) required to synchronise the data acquisition with the variable cardiac cycle. The variations in TR results in fluctuations of image intensity that can easily dominate the BOLD signal. One method to counteract these signal fluctuations is to remove the TR dependence by collecting multiple echoes to create a T_2* map at each time point. This method has been shown to significantly improve the detection rate for fMRI in the brainstem (Beissner et al., 2011; Zhang et al., 2006) and is analagous to the collection of MESSER data for BOLD-VSI, where maps of R_2* and R_2 are created at each TR (Jochimsen and Moller, 2008).

In this study we compare the efficacy of gated VSI data acquisition collected with two different MRI sequence implementations; one a multi-echo readout (MESSER), the second a dual-echo readout (one gradient-echo and one spin-echo). In the case of the dual-echo readout correction for the variable TR is implemented via the T_1 estimation method proposed by Guimaraes et al., (Guimaraes et al., 1998).

7.2 Theory

The mean vessel size within a voxel can be estimated from a measurement of ΔR_2^* and ΔR_2 caused by a change in intravascular susceptibility ($\Delta\chi$). This measurement is based on the differential vessel size sensitivity exhibited by gradient echo and spin echo acquisitions, as noted in modelling studies performed by (Boxerman et al., 1995). The change in relaxation rate can be estimated either from a direct measurement of R_2^* and R_2 at baseline and stimulation (Jochimsen and Moller, 2008), or indirectly from the change in signal amplitude (Prinster et al., 1997). In order to make a direct calculation of the relaxation rate Jochimsen et al. introduced a single-shot GESFIDE sequence called multi-gradient-echo single-shot-sampling of spin-echo refocusing (MESSER). The sequence uses multiple samples of both the free-induction decay (FID) and spin-echo rephasing (SER) portions of a spin-echo signal. Therefore allowing the calculation of R_2^* from the FID echoes and R_2^- from the SER echoes (where R_2^- is the rate constant associated with spin-echo rephasing). The value of R_2 is then calculated from a linear combination of the relaxation rates, as described by equation 7.1.

$$R_2 = \left(R_2^* + R_2^-\right)/2 \qquad [7.1]$$

An alternative approach to calculate the vessel size is to acquire only a single gradient-echo and spin-echo acquisition in each TR, and calculate the relaxation rate changes from the difference in signal between rest and stimulation (equations 7.2a and 7.2b).

$$\Delta R_2^* = -\frac{\ln\left(S(t)_{GE}/S_{0,GE}\right)}{TE_{GE}} \qquad [7.2a]$$

$$\Delta R_2 = -\frac{\ln\left(S(t)_{SE} / S_{0,SE}\right)}{TE_{SE}} \qquad [7.2b]$$

where S(t) is the time course of the signal magnitude, S_0 is its average value during baseline and TE is the corresponding gradient-echo or spin-echo time.

Because these calculations compare signal amplitudes across different TRs they are susceptible to fluctuations in TR, which arise when gating an acquisition to the cardiac cycle. For a given echo time the amplitude of any signal is dependent on the T_1 of the tissue and the TR, as described by equations 7.3 and 7.4.

$$S_{(n,i)} = A_{(n,i)}\left[1 - \exp\left(-TR/T_{1,n}\right)\right] \qquad [7.3]$$

which can be inverted to give

$$A_{(n,i)} = S_{(n,i)}\left[1 - \exp\left(-TR/T_{1,n}\right)\right]^{-1} \qquad [7.4]$$

where $S_{(n,i)}$ is the measured signal for the *n*th voxel at the *i*th acquisition and $A_{(n,i)}$ is the maximum signal amplitude for an infinite TR.

If TR is sufficiently short (compared to T_1) the value of the measured signal will depend heavily on the acquisition time. However, by inserting known TR values into equation 7.4 and minimising the fluctuations in A_n Guimaraes et al. (Guimaraes et al., 1998) demonstrated that it was possible to solve for A_n and $T_{1,n}$. Having solved for the voxelwise T_1 values an average TR may be used to recover S_n from A_n, and thus correct for variations in TR. Implementation of this correction method by Zhang et al. (Zhang et al., 2006) demonstrated accurate estimates of T_1 could be achieved, while simultaneously

reducing cardiac related noise. However, the greatest gains in noise reduction were achieved with multi-echo techniques, which are invariant to TR fluctuations.

7.3 Methods

GE and SE signals were modelled using the ODIN NMR C++ framework to create Monte-Carlo simulations of water in a vascular network, as per (Germuska et al., 2013). Two different sets of simulations were run. The first simulation modelled the dual echo sequence with one gradient-echo and one spin-echo, at 30 and 90 ms respectively. The second set of simulations modelled the MESSER acquisition, with echo times of 13, 31, 49, and 125 ms; the first three echoes sampling the FID and the fourth echo acquired at the spin-echo time.

Vessel modelling was undertaken for an intravascular susceptibility change, $\Delta\chi$, of -0.10 ppm and 30 different vessel radii distributed exponentially in the range from 1 to 60 μm. The susceptibility change was chosen to correspond with the expected stimulus associated with a 100% oxygen challenge (being approximately twice the susceptibility change measured with an FiO_2 of 0.5 (Germuska et al., 2013)). In all simulations the difference between fully oxygenated and deoxygenated haemoglobin was taken to be 0.264 ppm (Spees et al., 2001). A post-capillary blood volume fraction of 3% and a haematocrit of 0.40 were assumed, while a diffusion coefficient of 0.77 $\mu m^2/ms$ was taken from the mean of the volunteer measurements. The blood T_2 values were calculated by fitting to Zhao et al. (Zhao et al., 2007) and assuming a venous oxy-haemoglobin saturation of 60% at rest; producing T_2 estimates of 32.2 and 41.4 ms, at rest and stimulation respectively.

For the MESSER simulations R_2* was estimated at rest and stimulation by linear regression of the FID echoes. R_2 values were calculated by $[\log(S_0) - \log(S_{TE})]/TE$ from the signal magnitude directly after excitation, S_0, and the signal magnitude at TE=125 ms, S_{TE}. For the dual-echo simulations relaxation rate changes were calculated directly using equations 7.2a and 7.2b for the gradient-echo and spin-echo data respectively, with S_0 being the signal directly after excitation. For each set of simulations look-up tables of q (ΔR_2*/ ΔR_2) against the simulated vessel radius were created, with intermediate values interpolated with spline curve fitting (Matlab, Mathworks, MA, USA). For a given set of parameters (resting susceptibility, susceptibility change) each vascular simulation took approximately 4-5 hours, running on a virtualised installation of NeuroDebian (hardware: 2.4 GHz Intel Core 2 Duo).

Six healthy volunteers (mean age 31 ± 6 years) were scanned on a 3 Tesla Siemens Verio with a 32-channel head coil. For each subject a diffusion weighted scan and four VSI scans were acquired. The diffusion weighted scan used 3 orthogonal directions with two b values (0 and 1000 s/mm^2). Voxel dimensions were 1.5x1.5x4 mm^3, 1.0 mm interslice gap and 13 slices. The VSI data were acquired using a dual GE-SE EPI readout (TR = 2 s, TE = 30/90 ms) and a MESSER EPI readout (TR = 2 s, TE = 13, 31, 49, 78, 95, 113 ms spin-echo time = 125 ms), see figure 7.1 for sequence timing diagrams. A GRAPPA acceleration factor of 2 was used for both readouts. Thirteen axial slices (3x3x4 mm^3 voxels, 1.0 mm interslice gap) were acquired with and without cardiac gating. Each VSI imaging paradigm consisted of one 18-minute session, comprised of 3x3minute hyperoxic periods interleaved with 3x3minute periods of normal air. During periods of hyperoxia, 100% oxygen was delivered to the volunteers via a non-rebreathing mask

(Flexicare Medical, Mountain Ash, UK) at a flow rate of 15 L/min. During rest periods, air was delivered through the mask at the same flow rate.

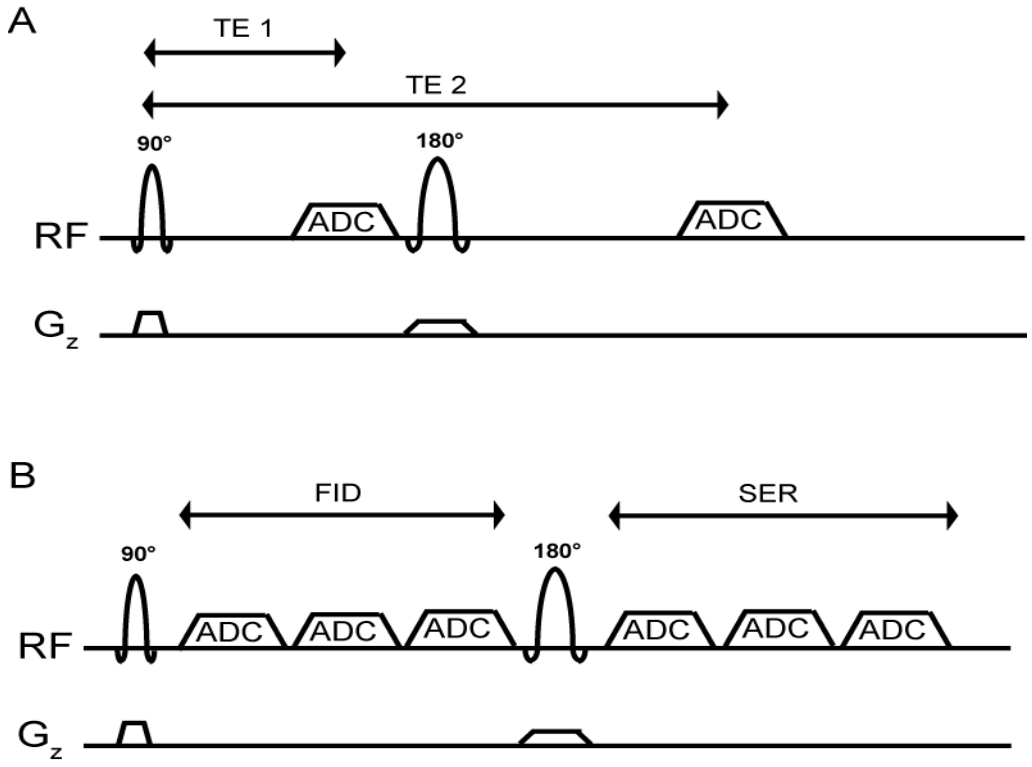

Figure 7.1. Sequence timing diagrams for the dual-echo (A) and MESSER (B) sequences used to collect the VSI data. Echo times of 30 ms (TE1) and 90 ms (TE2) used to acquire gradient-echo and spin-echo data in the dual-echo sequence. MESSER echo times of 13, 31 and 49 ms used during free-induction decay (FID) and echo times of 78, 95 and 113 ms during the spin-echo rephasing (SER).

All individual echoes were pre-processed using FSL software tools for motion correction (Jenkinson et al., 2002) and brain extraction (Smith, 2002). Spatial smoothing with a Gaussian kernel with a full width half maximum of 8 mm was applied to all data. All subsequent data processing and analysis was performed in Matlab. The log of the MESSER data points for each TR were fitted with a linear regression to produce R_2* and

R_2^- time series, with R_2 values being calculated according to equation 7.1. The initial data point in each time series was used to convert the data into estimates of ΔR_2^* and ΔR_2.

Gated gradient-echo data were corrected for fluctuations in TR as proposed by Guimaraes et al. (Guimaraes et al., 1998). However, in the current work the T_1 estimation approach is extended to include simultaneous fitting of the fMRI paradigm and baseline drift. The baseline is modelled by a simple quadratic equation, which has be found to perform equally well as more sophisticated baseline models (Tanabe et al., 2002), while the BOLD paradigm is calculated by convolving a boxcar signal with a gamma-variate function (Bulte et al., 2012). As per Guimaraes et al. the fluctuations in A_n are minimised with known TR values (extracted from the DICOM image headers). Signal fluctuations in the gated spin-echo data were corrected using T_1 values calculated from the gradient-echo data. To maintain consistency between the techniques, the baseline was estimated in the same manner for non-gated data (although T_1 was not estimated in this case).

After correcting for TR related fluctuations and baseline drift, relaxation rate changes for the dual-echo data were calculated using equations 7.2a and 7.2b. For all datasets a total least squares regression of ΔR_2^* against ΔR_2 was used to calculate q (Germuska et al., 2013). For each estimate of q the Chi-square fitting residual was recorded, providing an estimate of the goodness of fit for each technique. Voxelwise estimates of q were converted to mean vessel radii by fitting to appropriate (MESSER or dual-echo) Monte-Carlo modelled data. Non-physiological vessel size estimates less than 1 μm or greater than 60 μm were discarded from the analysis.

7.4 Results

Simulations

The Monte-Carlo modelling reveals a variation in the relationship between q and vessel size in the dual-echo and MESSER simulations (figure 7.2). This variation is most pronounced for large vessel radii and is due to the echo time dependence of the relaxation rate measurements. Although the variation between simulations is small for low q values, the figure demonstrates the need to simulate the vessel size dependence for each implemented MR protocol, avoiding potentially large errors for high q values.

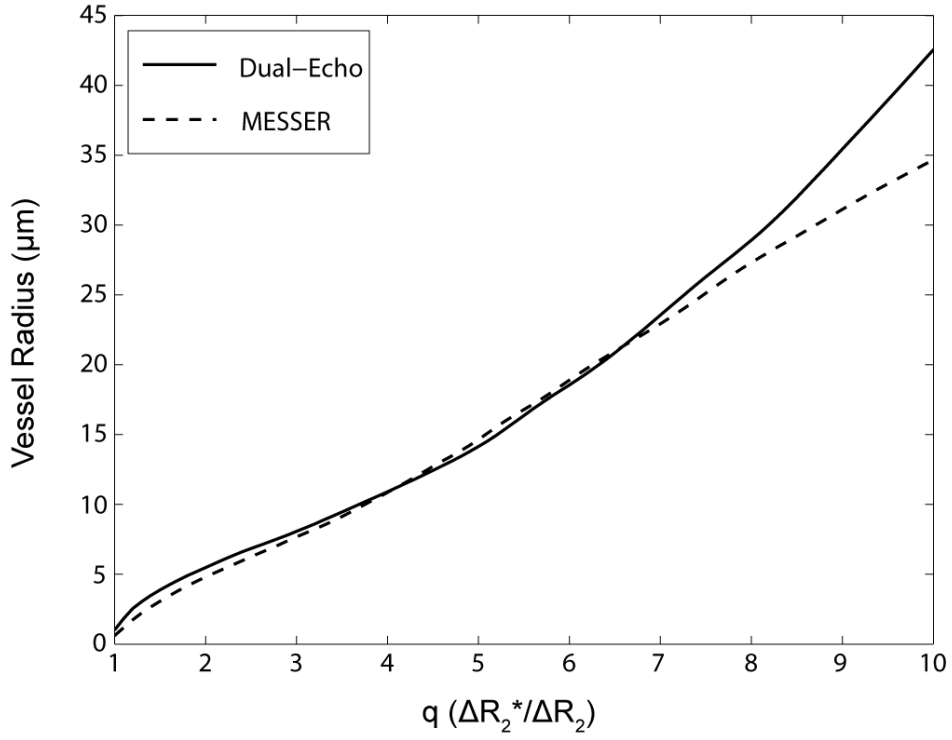

Figure 7.2. Curves to relate the ratio q=ΔR2*/ΔR2 to a vessel radii obtained by Monte Carlo simulation of dual-echo and MESSER acquisitions.

Experimental

In each set of experiments T_1, T_2*, T_2 and ADC values were successfully calculated from the acquired datasets. With T_1 value being calculated from the triggered dual-echo data, and quantitative T_2* and T_2 values being calculated from the MESSER data. A summary of the mean brainstem values acquired in the pilot study is given in table 7.1.

	T_1 (s)	T_2* (ms)	T_2 (ms)	ADC (μm^2/ms)
Mean ± s.d.	1.43 ± 0.1	51 ± 4.6	73 ± 2.9	0.769 ± 0.03

Table 7.1 Group mean (n=6) brainstem values for each derived parameter.

The calculated T_1 value is slightly higher than previous brainstem T_1 measurements in a similar age group (Lambert et al., 2013), who found a mean value of approximately 1.14 s. This discrepancy is likely due to the inclusion of nearby CSF in our analysis via partial voluming of the large voxels and blurring due to the 8mm spatial filter. Figure 7.3 shows example T_1 maps calculated from the gated dual-echo data. The proximity of long T_1 tissues adjacent to the brainstem is apparent; while T_1 values in the cortex have the expected distribution and magnitude. The measured T_2* values are also slightly longer in our study, 51 ms rather than 40 ms. Again this is likely due to partial voluming of the large voxels with neighbouring long T_2 tissues.

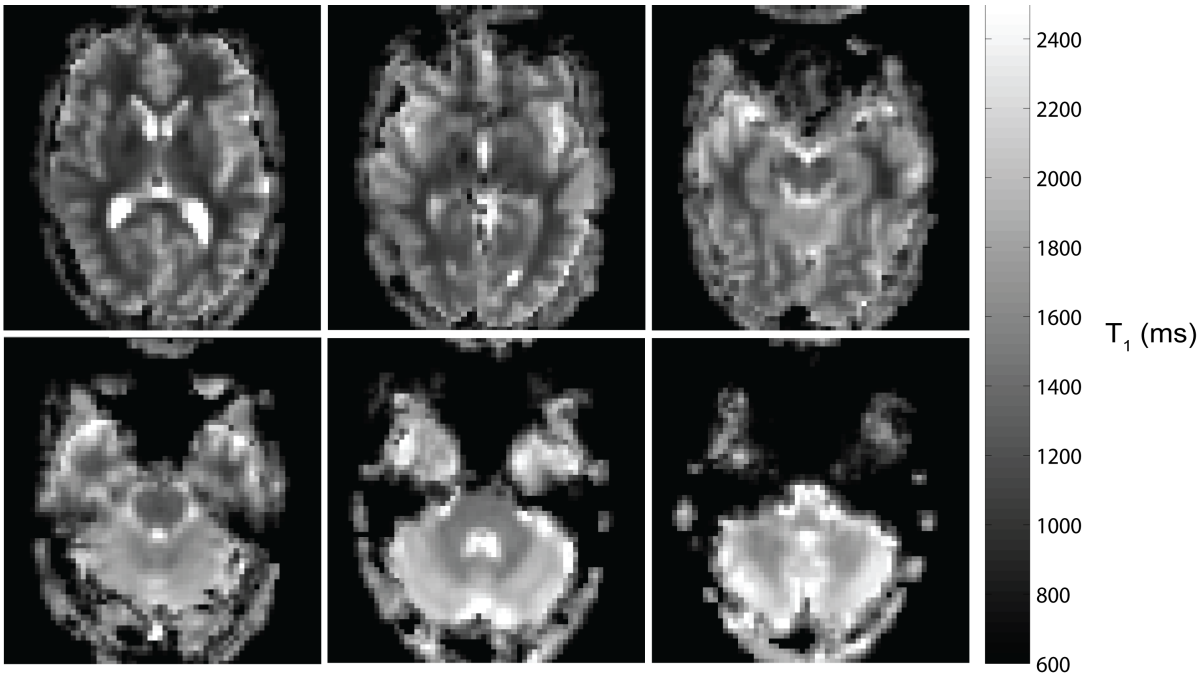

Figure 7.3. Example T_1 maps calculated from gated dual-echo data in a single volunteer

Gated acquisitions acquired an average of 396 time points per examination, while continuous acquisitions acquired 540 time points. This reduction in signal averages represents an approximate 14% reduction in SNR. Despite this, the performance (as measured by the reduced Chi-square fitting residuals) of gated acquisitions appears to be as good (dual-echo), or better (MESSER) than non-gated acquisitions. Figure 7.4 shows example vessel size maps calculated with each acquisition method. The same data is displayed in both an axial view and sagittal view, highlighting the regional variation in vessel size estimates and the efficacy of each method.

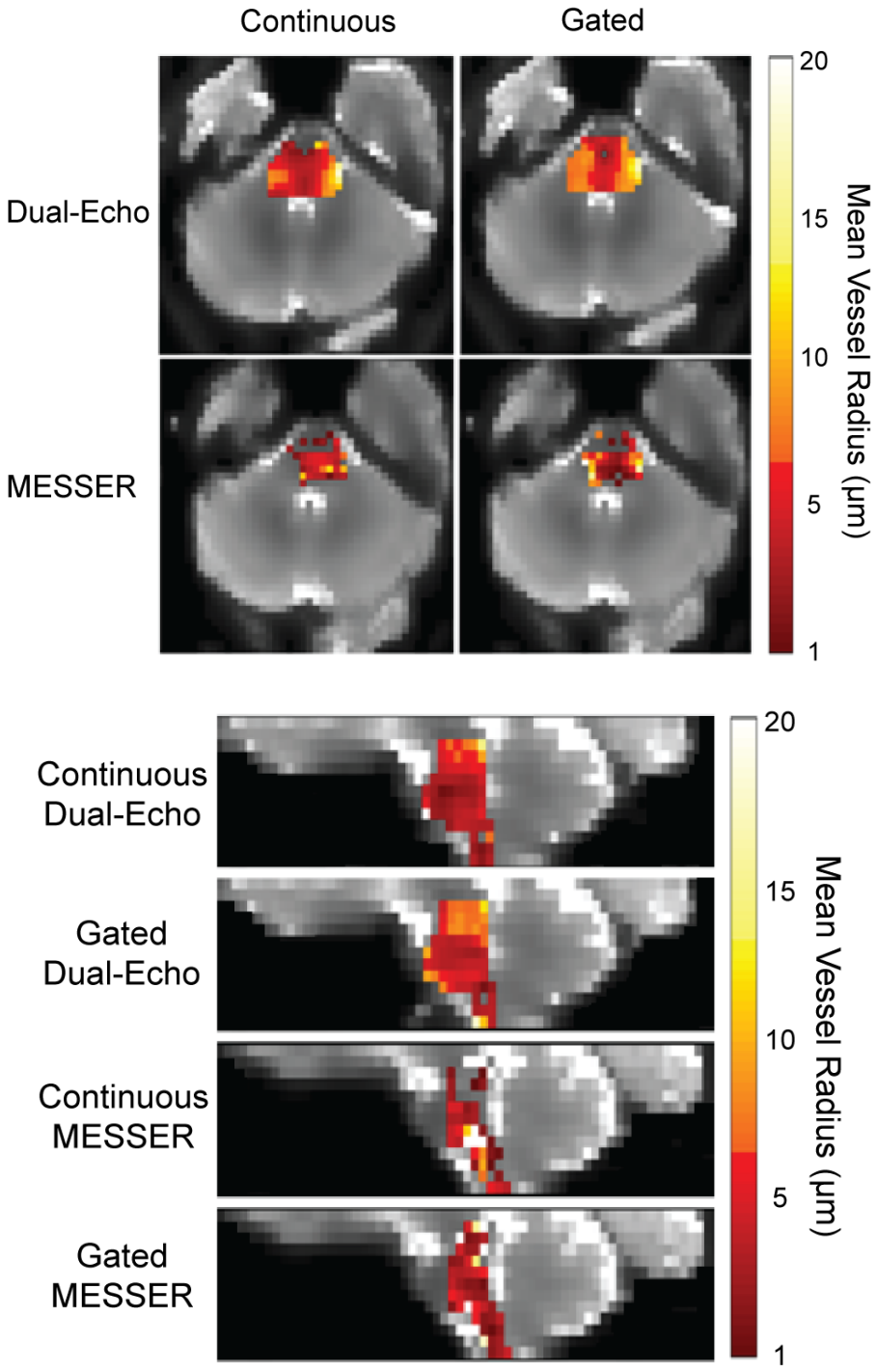

Figure 7.4. Example brainstem vessel size parameter maps from one volunteer; axial slice (top) sagittal slice (bottom). Comparison of the estimated mean vessel radii (μm) for each of the implemented techniques.

Consistent with previous findings, the gated multi-echo data (MESSER) demonstrably provides more robust estimates than the continuous MESSER acquisition. However, figure 7.4 clearly illustrates the superiority of the dual-echo acquisitions over the MESSER data, producing voxelwise measurements throughout the brainstem. The superiority of the dual-echo data is counter to that found in previous fMRI brainstem studies (Zhang et al., 2006), where a clear advantage was found for multi-echo acquisitions. The group averaged brainstem values and fitting residuals are given in table 7.2, where the goodness of fit for each technique can be seen from the reduced chi-square values (chi-square/degrees of freedom).

	q	Vessel Radius (μm)	Reduced Chi-Square
Dual-Echo	2.64 ± 0.5	7.34 ± 1.1	0.89 ± 0.07
Dual-Echo Gated	2.66 ± 0.4	7.33 ± 0.9	0.87 ± 0.15
MESSER	2.60 ± 0.6	5.95 ± 1.3	1.81 ± 0.40
MESSER Gated	2.75 ± 0.6	6.61 ± 1.4	1.39 ± 0.23

Table 7.2. Group mean (n=6) q ratio and vessel radius estimates for each technique.

The dual-echo sequences have smaller Reduced Chi-Square values than the MESSER acquisitions and thus, as observed from figure 7.4, demonstrate a more robust fit to the data. However, there was no significant difference ($p>0.05$) in the vessel size estimates made with the continuous or gated protocols, with mean estimates of 7.34 and 7.33 μm respectively. The mean vessel size estimates made with all techniques are lower than the majority of previous gray matter measurements (Germuska et al., 2013; Jochimsen et al.,

2010; Jochimsen and Moller, 2008; Kiselev et al., 2005; Xu et al., 2011). However, this is consistent with the lack of large (draining) veins in the brainstem, and in agreement with contrast agent measurements made in the thalamus (Xu et al., 2011). In superior sections of the brainstem, lateral estimates of vessel size were consistently greater than medial estimates. It is unclear whether this is related to a difference in vessel size or the diffusion environment. In the Monte-Carlo simulations diffusion was assumed to be uniform throughout the brain. However, the diffusion maps show a certain degree of heterogeneity, particularly in the superior brainstem and the midbrain where a lateral reduction in the apparent diffusion coefficient can be seen (figure 7.5).

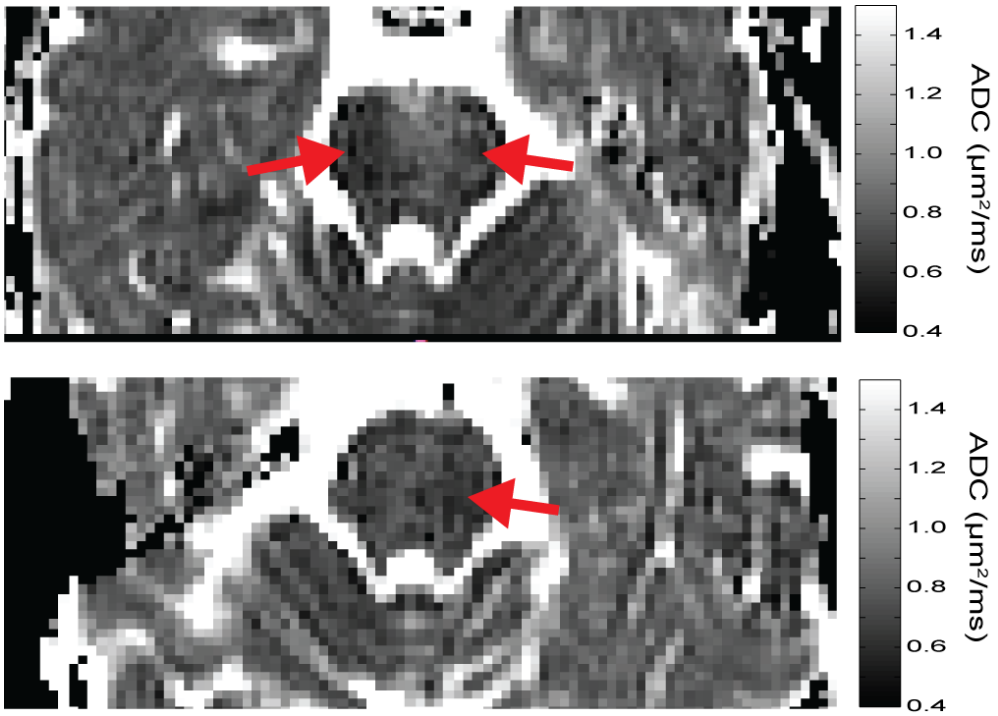

Figure 7.5. Example ADC maps showing lateral reduction in the apparent diffusion coefficient in the superior brainstem (red arrows).

The spatial distribution of the larger vessel size estimates may also explain the lower group values calculated with the MESSER technique, which was unable to make robust estimates in these regions. Indeed, the MESSER acquisitions appear to be particularly prone to error in the anterior and superior/lateral aspect of the brainstem, where few valid estimates were made in this example dataset.

7.5 Discussion

The present study compared two different data acquisitions schemes, with cardiac gating and conventional ungated acquisitions, in their ability to calculate voxelwise estimates of mean vessel size in the brainstem. The MR signal is modulated with a hyperoxic gas challenge, producing an evoked BOLD response that offers a completely non-invasive means of assessing a key biomarker. However, as with all brainstem fMRI methods, the assessment of vessel size in the brainstem via the BOLD contrast mechanism is challenging due to the significant levels of cardiogenic noise. Thus, we have extended vessel size data acquisition schemes to include cardiac gated versions of previously employed methods. Our results demonstrate a clear advantage of a dual-echo acquisition scheme over a multi-echo approach in the brainstem. This is in contrast to the findings reported for gradient-echo acquisitions of fMRI data (Zhang et al., 2006); where a multi-echo approach provided more robust detection of activation. However, our results are in agreement with regard to gated versus non-gated acquisitions, with MESSER data in particular showing a significant improvement when gated.

The poor performance of the multi-echo sequence appears to be largely due to the significant susceptibility gradients around the brainstem; with the short T_2* at the edges

of the brainstem causing considerable attenuation of the later echoes. Vessel size estimates from fMRI data are highly sensitive to errors in the measurement of ΔR_2 (Shen et al., 2011). Therefore, the reduced signal-to-noise during SER echoes can easily result in non-physiological estimates of vessel size (outside of the modelled vessel size range: 1 to 60 μm). The consequence of this is apparent in figure 7.4, where neither the gated nor continuous MESSER acquisitions were able to produce physiological vessel size estimates in the Pons. Because the poor performance of the MESSER sequence appears to be due to fitting errors during SER, it is possible that the sequence could be improved by reducing the SE time. This could most easily be achieved by reducing the number of echo readouts to four (two during the FID and two during the SER). Modifying the sequence in this way would allow for a shorter and thus more optimal SE time, improving the signal-to-noise of the SER readouts. The advantage of a shorter SE time is demonstrated by the superior performance of the dual-echo sequence, where a more optimal spin-echo time of 90 ms could be employed.

While there was a small trend for an increased performance with the gated dual-echo sequence versus the standard acquisition (smaller standard deviation in vessel size estimates and lower Reduced Chi-Square value), the results were not significantly different. The consistency of the results between these two implementations, both in terms of mean values and similarity of parameter maps, indicates that there is a high degree of within session repeatability. Although, repeatability was not systematically investigated in this work and needs further investigation, both in terms of subject numbers and across session validation, these initial results are promising. The sensitivity of the measurement to changes in vessel size also needs further investigation and in

particular the sensitivity to the water diffusion rate. The variability in vessel size estimates in the superior brainstem appears to be correlated with changes in ADC. With the increase in lateral vessel size estimates visually corresponding to a reduction in ADC values (see figures 7.4 and 7.5). This is consistent with vessel size equations based on contrast-agent based techniques (Tropres et al., 2001). However, further Monte-Carlo modelling is required to incorporate such information in to a hyperoxic measurement of vessel size.

In addition to providing vessel size estimates the gated dual-echo technique also provides an estimate of the tissue T_1, which is of itself a valuable biomarker for disease monitoring (Duvvuri et al., 2001; Hoehn-Berlage and Bockhorst, 1994). Thus, although no significant performance increase was observed with the gated acquisition, this method of data acquisition does have the advantage of acquiring an additional quantitative measurement. Calculation of T_1 values from gated acquisitions has previously been found to provide robust estimates that were comparable with inversion recovery measurements (Zhang et al., 2006). However, the estimates reported in our pilot study are somewhat greater than previously reported in the brainstem (Lambert et al., 2013). The most likely explanation for this is partial voluming and spatial smoothing of the signal from nearby CSF voxels. It is expected that such signal contamination could be reduced using smaller voxels and segmentation of the brainstem data prior to spatial smoothing. However, given the agreement of the gated and non-gated acquisitions, this presumed over-estimation of T_1 did not appear to have a significant influence on estimates of vessel size.

In conclusion I have demonstrated the applicability of hyperoxic estimation of vessel size in the brainstem with standard and gated dual-echo acquisitions. Implementation of

multi-echo sequences, that have previously been employed in the brain, demonstrated a vulnerability to short T_2* regions at the anterior of the brainstem. The results suggest that the reproducibility of vessel size estimates with the dual-echo acquisition is high, with no significant differences observed between within session acquisitions. However, extension of the modelling methods to incorporate diffusion measurements appears to be necessary to improve the specificity of the technique.

Chapter 8

Summary and Recommendations

This thesis has addressed some of the key issues in the physiological interpretation of the BOLD signal; creating a framework for the simultaneous estimation of cerebral blood volume, mean vessel size and oxygen extraction fraction. The new framework is based on the investigation of existing methods for individual parameter estimates. Through the course of this investigation a number of points have arisen that would benefit from further research. This chapter summarises the main findings of this thesis and includes a brief outline of possible future work.

8.1 Blood Volume Measurement

Measurement of the venous-weighted blood from a calibrated hyperoxic BOLD signal change was investigated in this thesis based on a previously published methodology (Bulte et al., 2007a). Analysis of the simplified BOLD (Davis et al., 1998) model revealed previously ignored subtleties in the translation of the methodology from contrast-based methods. The new analysis reveals an error in the haematocrit-weighting factor that accounts for the difference in large to small vessel red blood cell content. Additionally, the new derivation of the CBV equation makes explicit the assumptions necessary when calibrating the BOLD signal against the signal change in a blood filled voxel. These assumptions, including a fixed value of the exponent β, result in an

overestimation of CBV, which was confirmed in a pilot study and in an associated research project (Blockley et al., 2013).

To overcome these methodological problems a new method of CBV calculation was proposed in this thesis. In the new method, CBV is calculated by calibrating against the end-tidal oxygen content rather than a blood filled voxel. In the implementation presented here the blood volume is calculated from serial hyperoxic and hypercapnic measurements, rather than a single hyperoxic stimulus. This implementation has the advantage of simultaneously estimating the OEF and vessel size from the same data. However, preliminary analysis of the modelled data suggests that CBV estimates from hyperoxic data are relatively insensitive to the resting OEF and vessel size for a range of healthy values. Future work that thoroughly investigates the sensitivity of hyperoxic CBV measurement to these parameters would be valuable for determining the applicability of this simpler methodology.

8.2 BOLD Vessel Size Imaging

Modelling studies were undertaken to explore the large discrepancy in published BOLD-VSI measurements. The investigation demonstrated that a large part of the variability in the results could be explained by the noise sensitivity of the analysis methods employed. These findings were confirmed with a pilot study, where a significant variation in vessel size estimates was produced depending on the analysis method. It was also demonstrated that the error in vessel size estimates made with regression techniques could be reduced by using the total least square error instead of ordinary least squares. This is in agreement with standard statistical theory, as regression with total least squares allows for

observational errors on both dependent and independent variables and so allows for uncertainties in both ΔR_2^* and ΔR_2. This is untrue of simple linear regression, which assumes the independent variable to be error free, and thus leads to attenuation bias when applied to vessel size estimates from ΔR_2^* and ΔR_2.

However, the noise analysis did not account for all of the variation in the reported BOLD estimates of vessel size. The likely source of the remaining bias is the use of different gas challenges to produce the evoked BOLD response. There is evidence that the estimated vessel size is greater when using a hypercapnic challenge than when using a hyperoxic challenge. The conventional explanation is that the hypercapnic challenge causes an increase in the mean venous vessel diameter and thus results in a greater estimate of vessel size. However, modelling studies presented in this thesis suggest that such an explanation is invalid and would in fact lead to the calculation of a lower vessel size when using a hypercapnic challenge. Instead the modelling results suggest that a hypercapnic challenge causes no net change in the mean venous vessel diameter, but does cause an increase in the effective blood volume exchanging oxygen with the tissue. This finding is in agreement with several vascular studies, which report an increase in the effective venous blood volume via a homogenisation of capillary and venous flow.

The Monte-Carlo modelling employed in this thesis is based on previous vascular models, which represent the mean vessel size by a single cylinder of infinite length. Because of this simplification it was not possible to model any changes in vessel size distribution that could be associated with a hypercapnic challenge. For example there is evidence that hypercapnia could cause an increase in the diameter of very small vessels and reduction in the diameter of larger vessels, while maintaining the same mean diameter (Hutchinson

et al., 2006). Previous investigations have found good agreement between the two-dimensional model of infinite cylinders, as used here, and three-dimensional models of the vasculature (Marques and Bowtell, 2008). However, dynamic changes in the vascular distribution were not investigated and may prove an important factor in determining the BOLD signal response to hypercapnia. Future work that includes a three-dimension model of the venous vasculature could be used to investigate the importance of such dynamic effects and provide a greater insight into the hypercapnic BOLD response.

The applicability of BOLD vessel size imaging in the brainstem was also explored in this thesis. Two existing VSI acquisition schemes, dual-echo and multi-echo, were compared with and without cardiac gating. The results suggest a clear advantage for the dual-echo acquisition scheme and demonstrated an overall improvement with gated acquisitions. The advantage of the dual-echo acquisition is contrary to the finding in brainstem fMRI studies that rely only on the gradient-echo data. This discrepancy appears to be due to the low signal-to-noise ratio during later echoes in the multi-echo sequence. However, vessel size measurements with dual-echo acquisitions appear to be consistent with minimal within-session variability between the gated and standard acquisition. Further work to explore the within-session and between-session repeatability of BOLD-VSI in the brainstem is needed to confirm its applicability to this region.

In addition to providing an attractive clinical target for vessel size imaging, the brainstem also provides a range of diffusion rates. Given that changes in the apparent diffusion coefficient have been linked with numerous diseases it is important that vessel size estimates are invariant to these changes. However, the pilot data collected in the brainstem suggest a high degree of sensitivity to changes in ADC in the current

implementation. This phenomenon is to be expected as the vessel size sensitivity is directly related to extra-vascular diffusion. Fortunately voxelwise estimates of diffusion could easily be incorporated into VSI measurements simply by repeating the Monte-Carlo modelling to cover a range of diffusion rates and expanding the VSI look-up table.

8.3 Estimation of the Oxygen Extraction Fraction

A new framework for estimating oxygen extraction fraction is presented in this thesis. The method relies on the observation that changes in intravascular susceptibility for hypercapnia are multiplicative with respect to the baseline value, while susceptibility changes for hyperoxia are additive. This difference between the two stimuli creates two independent probes of the BOLD signal, setting up a system of simultaneous equations that can be solved to find the venous oxy-haemoglobin saturation. By including measurements of the spin-echo BOLD response, a further two probes of the BOLD signal are introduced, allowing the vessel size and blood volume to be calculated. Monte-Carlo modelling studies of a 2D vascular network were implemented to demonstrate that a unique solution could be found for each of these parameters with the proposed framework. In addition, pilot data was collected from which voxelwise estimates of each parameter were successfully calculated.

The modelling results suggest that the new framework is able to calculate a more accurate estimate of OEF over a wider range of physiology compared to recently proposed techniques that implicitly assume fixed vascular parameters (Bulte et al., 2012; Gauthier and Hoge, 2012). Because there is a strong correlation between vascular re-modelling and

oxygen availability (Dore-Duffy and LaManna, 2007), this ability to simultaneously estimate vessel size and OEF significantly broadens the scope of the technique.

Sensitivity analysis reveals that estimates of OEF are primarily sensitive to errors in measurement of the hypercapnic blood flow response. A number of high OEF estimates visible in the parameter maps are likely due to such errors. The protocol implemented in the pilot study was optimised for subject comfort and hyperoxic gas delivery, producing only a mild hypercapnic stimulus. Thus it is anticipated that voxelwise OEF estimates could be improved by altering the gas delivery method. Indeed significant improvement in the results may be achieved by optimising the acquisition protocol with regard to the model sensitivity. Additional improvements could also be achieved by including intravascular signal in the Monte-Carlo modelling, removing the need to suppress the blood signal and increasing the BOLD contrast-to-noise ratio.

Bibliography

Ances, B.M., Leontiev, O., Perthen, J.E., Liang, C., Lansing, A.E., Buxton, R.B., 2008. Regional differences in the coupling of cerebral blood flow and oxygen metabolism changes in response to activation: Implications for BOLD-fMRI. Neuroimage 39, 1510-1521.

Bandettini, P.A., Wong, E.C., 1995. Effects of biophysical and physiologic parameters on brain activation-induced R2 * and R2 changes: simulations using a deterministic diffusion model. International Journal of Imaging Systems and Technology 6, 133-152.

Baron, J.C., Bousser, M.G., Comar, D., 1981a. Noninvasive tomographic study of cerebral blood flow and oxygen metabolism in vivo. Potentials, limitations, and clinical applications in cerebral ischemic disorders. European Neurology 20, 273-284.

Baron, J.C., Bousser, M.G., Rey, A., Guillard, A., Comar, D., Castaigne, P., 1981b. Reversal of focal "misery-perfusion syndrome" by extra-intracranial arterial bypass in hemodynamic cerebral ischemia. A case study with 15O positron emission tomography. Stroke 12, 454-459.

Barth, M., Moser, E., 1997. Proton NMR relaxation times of human blood samples at 1.5 T and implications for functional MRI. Cellular and Molecular Biology 43, 783-791.

Beaney, R.P., Lammertsma, A.A., Jones, T., McKenzie, C.G., Halnan, K.E., 1984. Positron emission tomography for in-vivo measurement of regional blood flow, oxygen utilisation, and blood volume in patients with breast carcinoma. Lancet 21, 131-134.

Beissner, F., Deichmann, R., Baudrexel, S., 2011. fMRI of the brainstem using dual-echo EPI. Neuroimage 55, 1593-1599.

Bernardi, S., Trimble, M.R., Frackowiak, R.S., Wise, R.J., Jones, T., 1983. An interictal study of partial epilepsy using positron emission tomography and the oxygen - 15 inhalation technique. Journal of Neurology Neurosurgery and Psychiatry 46, 473-477.

Biron, K.E., Dickstein, D.L., Gopaul, R., Jefferies, W.A., 2011. Amyloid Triggers Extensive Cerebral Angiogenesis Causing Blood Brain Barrier Permeability and Hypervascularity in Alzheimer's Disease. PLoS ONE 6, e23789.

Blockley, N.P., Griffeth, V.E.M., Germuska, M., Bulte, D.P., Buxton, R.B., 2013. An analysis of the use of hyperoxia for measuring venous cerebral blood volume: comparison of the existing method with a new analysis approach. Neuroimage 72, 33-40.

Bosomtwi, A., Jiang, Q., Ding, G.L., Zhang, L., Zhang, Z.G., Lu, M., Ewing, J.R., Chopp, M., 2008. Quantitative evaluation of microvascular density after stroke in rats using MRI. Journal of Cerebral Blood Flow and Metabolism 28, 1978-1987.

Boxerman, J.L., Hamberg, L.M., Rosen, B.R., Weisskoff, R.M., 1995. MR Contrast due to Intravascular Magnetic Susceptibility Perturbations. Magnetic Resonance in Medicine 34, 555-566.

Bradaric, B.D., Patel, A., Schneider, J.A., Carvey, P.M., Hendey, B., 2012. Evidence for Angiogenesis in Parkinson's disease, Incidental Lewy Body disease, and Progressive Supranuclear Palsy. Journal of Neural Transmission 119, 59-71.

Brian Jr, J.E., 1998. Carbon dioxide and the cerebral circulation. Anesthesiology 88, 1365-1386.

Bulte, D.P., Chiarelli, P.A., Wise, R., Jezzard, P., 2007a. Measurement of Cerebral Blood Volume in Humans Using Hyperoxic MRI Contrast. Journal of Magnetic Resonance Imaging 26, 894-899

Bulte, D.P., Chiarelli, P.A., Wise, R.G., Jezzard, P., 2007b. Cerebral perfusion response to hyperoxia. Journal of Cerebral Blood Flow and Metabolism 27, 69-75.

Bulte, D.P., Kelly, M., Germuska, M., Xie, J., Chappell, M.A., Okell, T.W., Bright, M.G., Jezzard, P., 2012. Quantitative measurement of cerebral physiology using respiratory-calibrated MRI. Neuroimage 60, 582-591.

Buxton, R.B., Wong, E.C., Frank, L.R., 1998. Dynamics of blood flow and oxygenation changes during brain activation: the balloon model. Magnetic Resonance in Medicine 39, 855-864.

Buxton, R.B., 2002. Introduction to Functional Magnetic Resonance Imaging. Cambridge UP, Cambridge.

Chiarelli, P.A., Bulte, D.P., Gallichan, D., Piechnik, S.K., Wise, R., Jezzard, P., 2007b. Flow-metabolism coupling in human visual, motor, and supplementary motor areas assessed by magnetic resonance imaging. Magnetic Resonance in Medicine 57, 538-547.

Chiarelli, P.A., Bulte, D.P., Wise, R., Gallichan, D., Jezzard, P., 2007a. A calibration method for quantitative BOLD fMRI based on hyperoxia. Neuroimage 37, 808-820.

Davis, T.L., Kwong, K.K., Weisskoff, R.M., Rosen, B.R., 1998. Calibrated functional MRI: Mapping the dynamics of oxidative metabolism. Proceedings of the National Academy of Sciences of the United States of America 95, 1834-1839.

Dennie, J., Mandeville, J.B., Boxerman, J.L., Packard, S.D., Rosen, B.R., Weisskoff, R.M., 1998. NMR imaging of changes in vascular morphology due to tumor angiogenesis. Magnetic Resonance in Medicine 40, 793-799.

Devonshire, I.M., Papadakis, N.G., Port, M., Berwick, J., Kennerley, A.J., Mayhew, J.E., Overton, P.G., 2012. Neurovascular coupling is brain region-dependent. Neuroimage 59, 1997-2006.

Dickson, J.D., Ash, T.W., Williams, G.B., Sukstanskii, A.L., Ansorge, R.E., Yablonskiy, D.A., 2011. Quantitative phenomenological model of the BOLD contrast mechanism. Journal of Magnetic Resonance 212, 17-25.

Diringer, M.N., Aiyagari, V., Zazulia, A.R., Videen, T.O., Powers, W.J., 2007. Effect of hyperoxia on cerebral metabolic rate for oxygen measured using positron emission tomography in patients with acute severe head injury. Journal of Neurosurgery 106, 526-529.

Dore-Duffy, P., LaManna, J.C., 2007. Physiologic angiodynamics in the brain. Antioxid Redox Signal 9, 1363-1371.

Dunn, J.F., Zhang, Q., Wu, Y., Smith, M.R., Shaw, R.A., Srinivasan, S., 2008. Monitoring angiogenesis noninvasively with near-infrared spectroscopy. Journal of Biomedical Optics 13, 064043.

Duvvuri, U., Poptani, H., Feldman, M., Nadal-Desbarats, L., Gee, M.S., Lee, W.M.F., Reddy, R., Leigh, J.S., Glickson, J.D., 2001. Quantitative T1 Magnetic Resonance Imaging of RIF-1 Tumors in Vivo: Detection of Early Response to Cyclophosphamide Therapy. Cancer Research 61, 7747-7753.

Farrar, C.T., Kamoun, W.S., Ley, C.D., Kim, Y.R., Kwon, S.J., Dai, G., Rosen, B.R., di Tomaso, E., Jain, R.K., Sorensen, A.G., 2010. In vivo validation of MRI vessel caliber index measurement methods with intravital optical microscopy in a U87 mouse brain tumor model. Neuro-Oncology 12, 341-350.

Fisel, C.R., Ackerman, J.L., Buxton, R.B., Garrido, L., Belliveau, J.W., Rosen, B.R., Brady, T.J., 1991. MR contrast due to microscopically heterogeneous magnetic susceptibility: numerical simulations and applications to cerebral physiology. Magnetic Resonance in Medicine 17, 336-347.

Freitas, R.A.J., 1999. Nanomedicine, Volume I: Basic Capabilities. Landes Bioscience, Georgetown, TX.

Frost, C., Thompson, S.G., 2000. Correcting for regression dilution bias: comparison of methods for a single predictor variable. Journal of the Royal Statistical Society Series a-Statistics in Society 163, 173-189.

Fujita, N., 2001. Extravascular Contribution of Blood Oxygenation Level-Dependent Signal Changes: A Numerical Analysis Based on a Vascular Network Model. Magnetic Resonance in Medicine 46, 723-734.

Gauthier, C.J., Hoge, R.D., 2012. Magnetic resonance imaging of resting OEF and CMRO2 using a generalized calibration model for hypercapnia and hyperoxia. Neuroimage 60, 1212-1225.

Gauthier, C.J., Hoge, R.D., 2013. A Generalized Procedure for Calibrated MRI Incorporating Hyperoxia and Hypercapnia. Human Brain Mapping 34, 1053-1069.

Gauthier, C.J., Madjar, C., Tancredi, F.B., Stefanovic, B., Hoge, R.D., 2011. Elimination of visually evoked BOLD responses during carbogen inhalation: Implications for calibrated MRI. Neuroimage 54, 1001-1011.

Germuska, M., Meakin, J.A., Bulte, D.P., 2013. The influence of noise on BOLD-mediated vessel size imaging analysis methods. Journal of Cerebral Blood Flow and Metabolism Aug 14.

Glover, G.H., Li, T.Q., Ress, D., 2000. Image-based method for retrospective correction of physiological motion effects in fMRI: RETROICOR. Magnetic Resonance in Medicine 44, 162-167.

Guimaraes, A.R., Melcher, J.R., Talavage, T.M., Baker, J.R., Ledden, P., Rosen, B.R., Kiang, N.Y.S., Fullerton, B.C., Weisskoff, R.M., 1998. Imaging Subcortical Auditory Activity in Humans. Human Brain Mapping 6, 33-41.

Grubb Jr, R.L., Raichle, M.E., Eichling, J.O., Ter Pogossian, M.M., 1974. The effects of changes in PaCO2 on cerebral blood volume, blood flow, and vascular mean transit time. Stroke 5, 630-639.

Haario, H., Laine, M., Mira, A., Saksman, E., 2006. DRAM: Efficient Adaptive MCMC. Statistical Computing 16, 339-354.

Hare, H.V., Germuska, M., Kelly, M.E., Bulte, D.P., 2013. Comparison of CO2 in air versus carbogen for the measurement of cerebrovascular reactivity with magnetic resonance imaging. Journal of Cerebral Blood Flow and Metabolism Aug 7.

Hawkes, C.H., Del Tredici, K., Braak, H., 2010. A time line for Parkinson's disease. Parkinsonism and Related Disorders 16, 79-84.

He, X., Yablonskiy, D.A., 2007. Quantitative BOLD: Mapping of human cerebral deoxygenated blood volume and oxygen extraction fraction: Default state. Magnetic Resonance in Medicine 57, 115-126.

Hoehn-Berlage, M., Bockhorst, K., 1994. Quantitative magnetic resonance imaging of rat brain tumors: in vivo NMR relaxometry for the discrimination of normal and pathological tissues. Technology and Health Care 2, 247-254.

Hoge, R.D., 2012. Calibrated fMRI. Neuroimage 62, 930-937.

Hoge, R.D., Atkinson, J., Gill, B., Crelier, G.R., Marrett, S., Pike, G.B., 1999. Investigation of BOLD signal dependence on cerebral blood flow and oxygen consumption: The deoxyhemoglobin dilution model. Magnetic Resonance in Medicine 42, 849-863.

Hsu, Y.Y., Yang, W.S., Lim, K.E., Liu, H.L., 2009. Vessel Size Imaging Using Dual Contrast Agent Injections. Journal of Magnetic Resonance Imaging 30, 1078-1084.

Hutchinson, E.B., Stefanovic, B., Koretsky, A.P., Silva, A.C., 2006. Spatial flow-volume dissociation of the cerebral microcirculatory response to mild hypercapnia. Neuroimage 32, 520-530.

Ishii, K., Kitagaki, H., Kono, M., Mori, E., 1996. Decreased medial temporal oxygen metabolism in Alzheimer's disease shown by PET. Journal of Nuclear Medicine 37, 1159-1165.

Ito, H., Ibaraki, M., Kanno, I., Fukuda, H., Miura, S., 2005. Changes in the arterial fraction of human cerebral blood volume during hypercapnia and hypocapnia measured by positron emission tomography. Journal of Cerebral Blood Flow and Metabolism 25, 852-857.

Ito, H., Kanno, I., Ibaraki, M., Hatazawa, J., Miura, S., 2003. Changes in human cerebral blood flow and cerebral blood volume during hypercapnia and hypocapnia measured by positron emission tomography. Journal of Cerebral Blood Flow and Metabolism 23, 665-670.

Ito, H., Kanno, I., Kato, C., Sasaki, T., Ishii, K., Ouchi, Y., Iida, A., Okazawa, H., Hayashida, K., Tsuyuguchi, N., Ishii, K., Kuwabara, Y., Senda, M., 2004. Database of normal human cerebral blood flow, cerebral blood volume, cerebral oxygen extraction fraction and cerebral metabolic rate of oxygen measured by positron emission tomography with 15O-labelled carbon dioxide or water, carbon monoxide and oxygen: A multicentre study in Japan. European Journal of Nuclear Medicine and Molecular Imaging 31, 635-643.

Jain, V., Langham, M.C., Wehrli, F.W., 2010. MRI estimation of global brain oxygen consumption rate. Journal of Cerebral Blood Flow and Metabolism 30, 1598-1607.

Jenkinson, M., Bannister, P., Brady, M., Smith, S., 2002. Improved optimization for the robust and accurate linear registration and motion correction of brain images. Neuroimage 17, 825-841.

Jensen, J.H., Chandra, R., 2000. MR imaging of microvasculature. Magnetic Resonance in Medicine 44, 224-230.

Jochimsen, T.H., Ivanov, D., Ott, D.V.M., Heinke, W., Turner, R., Moller, H.E., Reichenbach, J.R., 2010. Whole-brain mapping of venous vessel size in humans using the hypercapnia-induced BOLD effect. Neuroimage 51, 765-774.

Jochimsen, T.H., Moller, H.E., 2008. Increasing specificity in functional magnetic resonance imaging by estimation of vessel size based on changes in blood oxygenation. Neuroimage 40, 228-236.

Jochimsen, T.H., von Mengershausen, M., 2004. ODIN - Object-oriented development interface for NMR. Journal of Magnetic Resonance 170, 67-78.

Kerbel, R.S., 2000. Tumor angiogenesis: past, present and the near future. Carcinogenesis 21, 505-515.

Kim, S.G., Ogawa, S., 2012. Biophysical and physiological origins of blood oxygenation level-dependent fMRI signals. Journal of Cerebral Blood Flow and Metabolism 32, 1188-1206.

Kiselev, V., Posse, S., 1999. Analytical model of susceptibility-induced MR signal dephasing: effect of diffusion in a microvascular network. Magnetic Resonance in Medicine 41, 499-509.

Kiselev, V.G., Strecker, R., Ziyeh, S., Speck, O., Hennig, J., 2005. Vessel size imaging in humans. Magnetic Resonance in Medicine 53, 553-563.

Kuschinsky, W., Paulson, O.B., 1992. Capillary circulation in the brain. Cerebrovascular and Brain Metabolism Reviews 4, 261-286.

Lambert, C., Chowdhury, R., FitzGerald, T.H.B., Fleming, S.M., Lutti, A., Hutton, C., Draganski, B., Frackowiak, R., Ashburner, J., 2013. Characterizing aging in the human

brainstem using quantitative multimodal MRI analysis. Frontiers in Human Neuroscience 7, Article 462.

Lee, S.P., Duong, T.Q., Yang, G., Iadecola, C., Kim, S.G., 2001. Relative changes of cerebral arterial and venous blood volumes during increased cerebral blood flow: Implications for bold fMRI. Magnetic Resonance in Medicine 45, 791-800.

Lee, V.S., 2005. Cardiovascular MR Imaging: Physical Principles to Practical Protocols. Lippincott Williams and Wilkins, Philadelphia, USA.

Lemasson, B., Valable, S., Farion, R., Krainik, A., Remy, C., Barbier, E.L., 2013. In Vivo Imaging of Vessel Diameter, Size, and Density: A Comparative Study Between MRI and Histology. Magnetic Resonance in Medicine 69, 18-26.

Liu, T.T., Brown, G.G., 2007. Measurement of cerebral perfusion with arterial spin labeling: Part 1. Methods. Journal of the International Neuropsychological Society 13, 517-525.

Lu, H., 2007. Quantitative evaluation of cerebral venous oxygenation using T2-Relaxation-Under-Spin-Tagging (TRUST) MRI. International Society of Magnetic Resonance in Medicine, Berlin, p. 256.

Lu, H., Ge, Y., 2008. Quantitative evaluation of oxygenation in venous vessels using T2-relaxation-under-spin-tagging MRI. Magnetic Resonance in Medicine 60, 357-363.

Lu, H.Z., Xu, F., Grgac, K., Liu, P.Y., Qin, Q., van Zijl, P., 2012. Calibration and validation of TRUST MRI for the estimation of cerebral blood oxygenation. Magnetic Resonance in Medicine 67, 42-49.

MacIntosh, B.J., Filippini, N., Chappell, M.A., Woolrich, M.W., Mackay, C.E., Jezzard, P., 2010. Assessment of arterial arrival times derived from multiple inversion time pulsed arterial spin labeling MRI. Magnetic Resonance in Medicine 63, 641-647.

Marques, J.P., Bowtell, R.W., 2008. Using forward calculations of the magnetic field perturbation due to a realistic vascular model to explore the BOLD effect. NMR in Biomedicine 21, 553-565.

Miles, K.A., Williams, R.E., 2008. Warburg revisited: imaging tumour blood flow and metabolism. Cancer Imaging : the official publication of the International Cancer Imaging Society.

Newman, G.C., Hospod, F.E., Patlak, C.S., Fain, S.E., Pulfer, K.A., Cook, T.D., O'Sullivan, F., 2006. Experimental estimates of the constants relating signal change to contrast concentration for cerebral blood volume by T2* MRI. Journal of Cerebral Blood Flow and Metabolism 26, 760-770.

Nield, L., Qi, X., Yoo, S.J., Valsangiacomo, E.R., Hornberger, L.K., Wright, G.A., 2002. MRI-based blood oxygen saturation measurements in infants and children with congenital heart disease. Pediatric Radiology 32, 518-522.

Ogawa, S., Menon, R.S., Tank, D.W., Kim, S.-G., Merkle, H., Ellermann, J.M., Ugurbil, K., 1993. Functional brain mapping by blood oxygenation level-dependent contrast

magnetic resonance imaging. A comparison of signal characteristics with a biophysical model. Biophysical Journal 64, 803-812.

Oja, J.M., Gillen, J., Kauppinen, R.A., Kraut, M., van Zijl, P.C., 1999. Venous blood effects in spin-echo fMRI of human brain. Magnetic Resonance in Medicine 42, 617-626.

Pauling, L., Coryell, C.D., 1936. The Magnetic Properties and Structure of Hemoglobin, Oxyhemoglobin and Carbonmonoxyhemoglobin. Proc Natl Acad Sci U S A. 22, 210-216.

Pennings, F.A., Bouma, G.J., Ince, C., 2004. Direct observation of the human cerebral microcirculation during aneurysm surgery reveals increased arteriolar contractility. Stroke 35, 1284-1288.

Perez-Barcena, J., Ibanez, J., Brell, M., Llinas, P., Abadal, J.M., Llompart-Pou, J.A., 2009. Study of a Brain Microcirculation in Cranioencephalic Trauma Using the Side Stream Field (Sdf) System. Medicina Intensiva 33, 256-259.

Perlmutter, J.S., Herscovitch, P., Powers, W.J., 1985. Standardized mean regional method for calculating global positron emission tomographic measurements. Journal of Cerebral Blood Flow and Metabolism 5, 476-480.

Phelps, M.E., Huang, S.C., Hoffman, E.J., Kuhl, D.E., 1979. Validation of tomographic measurement of cerebral blood volume using C-11-labeled carboxyhemoglobin. Journal of Nuclear Medicine 42, 1032-1039.

Prinster, A., Pierpaoli, C., Turner, R., Jezzard, P., 1997. Simultaneous measurement of Delta R2 and Delta R2* in cat brain during hypoxia and hypercapnia. Neuroimage 6, 191-200.

Qin, Q., Grgac, K., Van Zijl, P.C.M., 2011. Determination of whole-brain oxygen extraction fractions by fast measurement of blood T2 in the jugular vein. Magnetic Resonance in Medicine 65, 471-479.

Reich, D.L., 2011. Monitoring in Anesthesia and Perioperative Care. Cambridge University Press.

Richards, E.M., Fiskum, G., Rosenthal, R.E., Hopkins, I., McKenna, M.C., 2007. Hyperoxic reperfusion after global ischemia decreases hippocampal energy metabolism. Stroke 38, 1578-1584.

Rigau, V., Morin, M., Rousset, M., de Bock, F., Lebrun, A., Coubes, P., Picot, M., Baldy-Moulinier, M., Bockaert, J., Crespel, A., Lerner-Natoli, M., 2007. Angiogenesis is associated with blood-brain barrier permeability in temporal lobe epilepsy. Brain 130, 1942-1956.

Rockswold, S.B., Rockswold, G.L., Zaun, D.A., Zhang, X., Cerra, C.E., Bergman, T.A., Liu, J., 2010. A prospective, randomized clinical trial to compare the effect of hyperbaric to normobaric hyperoxia on cerebral metabolism, intracranial pressure, and oxygen toxicity in severe traumatic brain injury. Journal of Neurosurgery 112, 1080-1094.

Rostrup, E., Larsson, H.B., Toft, P.B., Garde, K., Henriksen, O., 1995. Signal changes in gradient echo images of human brain induced by hypo- and hyperoxia. NMR in Biomedicine 8, 41-47.

Schmainda, K.M., Rand, S.D., Joseph, A.M., Lund, R., Ward, B.D., Pathak, A.P., Ulmer, J.L., Baddrudoja, M.A., Krouwer, H.G.J., 2004. Characterization of a first-pass gradient-echo spin-echo method to predict brain tumor grade and angiogenesis. American Journal of Neuroradiology 25, 1524-1532.

Severinghaus, J.W., 1979. Simple, accurate equations for human blood O2 dissociation computations. Journal of Applied Physiology 46, 599-602.

Shen, Y., Pu, I.M., Ahearn, T., Clemence, M., Schwarzbauer, C., 2013. Quantification of Venous Vessel Size in Human Brain in Response to Hypercapnia and Hyperoxia Using Magnetic Resonance Imaging. Magnetic Resonance in Medicine 69, 1541-1552.

Shen, Y.J., Ahearn, T., Clemence, M., Schwarzbauer, C., 2011. Magnetic resonance imaging of the mean venous vessel size in the human brain using transient hyperoxia. Neuroimage 55, 1063-1067.

Silvennoinen, M.J., Clingman, C.S., Golay, X., Kauppinen, R.A., van Zijl, P.C., 2003. Comparison of the dependence of blood R2 and R2* on oxygen saturation at 1.5 and 4.7 Tesla. Magnetic Resonance in Medicine 49, 47-60.

Simic, G., Stanic, G., Mladinov, M., Jovanov-Milosevic, N., Kostovic, I., Hof, P.R., 2009. Does Alzheimer's disease begin in the brainstem? Neuropathology and Applied Neurobiology 35, 532-554.

Smith, S.M., 2002. Fast robust automated brain extraction. Human Brain Mapping 17, 143-155.

Smith, S.M., Jenkinson, M., Woolrich, M.W., Beckmann, C.F., Behrens, T.E.J., Johansen-Berg, H., Bannister, P.R., De Luca, M., Drobnjak, I., Flitney, D.E., Niazy, R.K., Saunders, J., Vickers, J., Zhang, Y., De Stefano, N., Brady, J.M., Matthews, P.M., 2004. Advances in functional and structural MR image analysis and implementation as FSL. Neuroimage 23, S208-S219.

Sobesky, J., Zaro, W.O., Lehnhardt, F.G., Hesselmann, V., Neveling, M., Jacobs, A., Heiss, W.D., 2005. Does the mismatch match the penumbra? Magnetic resonance imaging and positron emission tomography in early ischemic stroke. Stroke 36, 980-985.

Spearman, C., 1904. The proof and measurement of association between two things. The American Journal of Psychology 15, 72-101.

Spees, W.M., Yablonskiy, D.A., Oswood, M.C., Ackerman, J.J.H., 2001. Water proton MR properties of human blood at 1.5 Tesla: Magnetic susceptibility, T-1, T-2, T-2* and non-Lorentzian signal behavior. Magnetic Resonance in Medicine 45, 533-542.

Sukstanskii, A.L., Yablonskiy, D.A., 2004. Gaussian approximation in the theory of MR signal formation in the presence of structure-specific magnetic field inhomogeneities. Effects of impermeable susceptibility inclusions. Journal of Magnetic Resonance 167, 56-67.

Tahergorabi, Z., Khazaei, M., 2012. A Review on Angiogenesis and Its Assays. Iranian Journal of Basic Medical Sciences 15, 1110-1126.

Tanabe, J., Miller, D., Tregellas, J., Freedman, R., Meyer, F.G., 2002. Comparison of detrending methods for optimal fMRI preprocessing. Neuroimage 15, 902-907.

Triantafyllou, C., Wald, L., Hoge, R.D., 2011. Echo-Time and Field Strength Dependence of BOLD Reactivity in Veins and Parenchyma Using Flow-Normalized Hypercapnic Manipulation. PLoS ONE 6, e24519.

Tropres, I., Grimault, S., Vaeth, A., Grillon, E., Julien, C., Payen, J.F., Lamalle, L., Decorps, M., 2001. Vessel size imaging. Magnetic Resonance in Medicine 45, 397-408.

Tropres, I., Lamalle, L., Peoc'h, M., Farion, R., Usson, Y., Decorps, M., Remy, C., 2004a. In vivo assessment of tumoral angiogenesis. Magnetic Resonance in Medicine 51, 533-541.

Tropres, I., Lamalle, L., Farion, R., Segebarth, C., Remy, C., 2004b. Vessel size imaging using low intravascular contrast agent concentrations. Magnetic Resonance Materials in Physics Biology and Medicine 17, 313-316.

Tudorica, A., Li, H.F., Hospod, F., Delucia-Deranja, E., Huang, W., Patlak, C.S., Newman, G.C., 2002. Cerebral blood volume measurements by rapid contrast infusion and T2*-weighted echo planar MRI. Magnetic Resonance in Medicine 47, 1145.

Van Zijl, P.C.M., Eleff, S.M., Ulatowski, J.A., Oja, J.M.E., Ulug, A.M., Traystman, R.J., Kauppinen, R.A., 1998. Quantitative assessment of blood flow, blood volume and blood oxygenation effects in functional magnetic resonance imaging. Nature Medicine 4, 159-167.

Walker-Samuel, S., Boult, J.K.R., McPhail, L.D., Box, G., Eccles, S.A., Robinson, S.P., 2012. Non-invasive in vivo imaging of vessel calibre in orthotopic prostate tumour xenografts. International Journal of Cancer 130, 1284–1293.

Weisskoff, R.M., Kiihne, S., 1992. MRI Susceptometry: image-based measurement of absolute susceptibility of MR constrast agents and human blood. Magnetic Resonance in Medicine 24, 375-383.

Wise, R.G., Harris, A.D., Stone, A.J., Murphy, K., 2013. Measurement of OEF and absolute CMRO2: MRI-based methods using interleaved and combined hypercapnia and hyperoxia. Neuroimage Epub ahead of print, doi: 10.1016.

Wolfson, L.I., Leenders, K.L., Brown, L.L., Jones, T., 1985. Alterations of regional cerebral blood flow and oxygen metabolism in Parkinson's disease. Neurology 35, 1399-1405.

Wong, E.C., Buxton, R.B., Frank, L.R., 1997. Implementation of quantitative perfusion imaging techniques for functional brain mapping using pulsed arterial spin labeling. NMR in Biomedicine 10, 237-249.

Wong, E.C., Buxton, R.B., Frank, L.R., 1998. Quantitative imaging of perfusion using a single subtraction (QUIPSS and QUIPSS II). Magnetic Resonance in Medicine 39, 702-708.

Woolrich, M.W., Chiarelli, P., Gallichan, D., Perthen, J., Liu, T.T., 2006. Bayesian inference of hemodynamic changes in functional arterial spin labeling data. Magnetic Resonance in Medicine 56, 891-906.

Woolrich, M.W., Ripley, B.D., Brady, M., Smith, S.M., 2001. Temporal autocorrelation in univariate linear modeling of FMRI data. Neuroimage 14, 1370-1386.

Wright, G.A., Hu, B.S., Macovski, A., 1991. Estimating Oxygen Saturation of Blood in Vivo with MR Imaging at 1.5 T. JMRI 1, 275-283.

Xu, C., Kiselev, V.G., Möller, H.E., Fiebach, J.B., 2013. Dynamic Hysteresis Between Gradient Echo and Spin Echo Attenuations in Dynamic Susceptibility Contrast Imaging. Magnetic Resonance in Medicine 69, 981-991.

Xu, C., Schmidt, W.U.H., Villringer, K., Brunecker, P., Kiselev, V., Gall, P., Fiebach, J.B., 2011. Vessel size imaging reveals pathological changes of microvessel density and size in acute ischemia. Journal of Cerebral Blood Flow and Metabolism 31, 1687-1695.

Xu, F., Liu, P., Pascual, J.M., Xiao, G., Lu, H., 2012a. Effect of hypoxia and hyperoxia on cerebral blood flow, blood oxygenation, and oxidative metabolism. Journal of Cerebral Blood Flow and Metabolism 32, 1909-1918.

Xu, F., Uh, J., Liu, P.Y., Lu, H.Z., 2012b. On improving the speed and reliability of T2-relaxation-under-spin-tagging (TRUST) MRI. Magnetic Resonance in Medicine 68, 198-204.

Yablonskiy, D.A., Haacke, E.M., 1994. Theory of NMR signal behavior in magnetically inhomogeneous tissues: the static dephasing regime. Magnetic Resonance in Medicine 32, 749-763.

Yang, R., Zhang, Q., Wu, Y., Dunn, J.F., 2013. Monitoring angiogenesis using a human compatible calibration for broadband near-infrared spectroscopy. Journal of Biomedical Optics 18, 016011.

Zhang, W., Mainero, C., Kumar, A., Wiggins, C.J., Benner, T., Purdon, P.L., Bolar, D.S., Kwong, K.K., Sorensen, A.G., 2006. Strategies for improving the detection of fMRI activation in trigeminal pathways with cardiac gating. Neuroimage 31, 1506-1512.

Zhang, Y.Y., Brady, M., Smith, S., 2001. Segmentation of brain MR images through a hidden Markov random field model and the expectation-maximization algorithm. IEEE Transactions on Medical Imaging 20, 45-57.

Zhao, J.M., Clingman, C.S., Narvainen, M.J., Kauppinen, R.A., van Zijl, P.C.M., 2007. Oxygenation and Hematocrit dependence of transverse relaxation rates of blood at 3T. Magnetic Resonance in Medicine 58, 592-597.

Ziener, C.H., Kampf, T., Melkus, G., Herold, V., Weber, T., Reents, G., M., J.P., R., B.W., 2007. Local frequency density of states around field inhomogeneities in magnetic resonance imaging: effects of diffusion. Phys Rev E Stat Nonlin Soft Matter Phys 76.